T.R.
BOLU ABANT İZZET BAYSAL UNIVERSITY
INSTITUTE OF GRADUATE STUDIES
Department of Chemistry

INVESTIGATION OF THE RELATION BETWEEN SURFACTANT HEAD GROUP SIZE AND FORMATION OF DIFFERENT TYPES OF LYOTROPIC NEMATIC PHASES IN BINARY SURFACTANT/DYE SYSTEMS

MASTER OF SCIENCE

BARIŞ OKUYAN

ACADEMIC SUPERVISOR
PROF. DR. EROL AKPINAR

BOLU, JULY -2024

APPROVAL OF THE THESIS

INVESTIGATION OF THE RELATION BETWEEN SURFACTANT HEAD GROUP SIZE AND FORMATION OF DIFFERENT TYPES OF LYOTROPIC NEMATIC PHASES IN BINARY SURFACTANT/DYE SYSTEMS submitted by **BARIŞ OKUYAN** and defended before the Examining Committe Members listed below in partial fulfillment of the requirements for the degree of **Master of Science** in **Department of Chemistry, Institute of Graduate Studies of Bolu Abant Izzet Baysal University in 22.07.2024** by

Examining Committee Members	**Signature**
Supervisor Prof. Dr. Erol AKPINAR Bolu Abant İzzet Baysal University	.....
Member Prof. Dr. Öznur DEMİR ORDU Bolu Abant İzzet Baysal University	.....
Member Assoc. Prof. Dr. Özgür MASALCI Ege University	.....

Prof. Dr. İbrahim KÜRTÜL

Director of Instıtute of Graduate Studies

To my wife and daughter

İzel &Bade

ETHICAL DECLARATION

In this thesis dissertation that was properly prepared according to the Thesis Writing Rules of Bolu Abant İzzet Baysal University of the Institute of Graduates Studies, I hereby declare that;

- All data, information, and documents presented in the thesis were obtained in accordance with the academic and ethical rules,
- All data, documents, assessments, and results were presented in accordance with the scientific ethical and moral rules,
- All works that were benefitted in the thesis were appropriately cited,
- No alteration was made in the data used,
- Study presented in this thesis is original,

Otherwise, I declare that I accept the loss of all my rights in case any contradiction that may arise against me.

The similarity rate obtained by using the Turnitin program, a plagiarism detection software, is within the limits approved by the University Senate.

_____

BARIŞ OKUYAN

ABSTRACT

INVESTIGATION OF THE RELATION BETWEEN SURFACTANT HEAD GROUP SIZE AND FORMATION OF DIFFERENT TYPES OF LYOTROPIC NEMATIC PHASES IN BINARY SURFACTANT/DYE SYSTEMS
MSC THESIS
BARIŞ OKUYAN
BOLU ABANT IZZET BAYSAL UNIVERSITY
INSTITUTE OF GRADUATE STUDIES
DEPARTMENT OF CHEMISTRY
(SUPERVISOR: PROF. DR. EROL AKPINAR)

BOLU, JULY 2024
(xviii + 103)

In the frame of this thesis, properties of some lyotropic binary surfactant mixtures, composed of surfactant, Sunset Yellow, dodecanol, and water, were studied at constant total surfactant concentrations. Dodecyldimethylammonium bromide (DDMABr), dodecyldimethylethylammonium bromide (DDMEABr), and dodecyltriethylammonium bromide (DTEABr) were chosen as surfactant molecules. The binary surfactant mixtures consisted of DDEMABr/DDMABr and DDMEABr/DTEABr. By changing the relative concentrations of each surfactant in the mixtures, lyotropic mixtures presenting lamellar, nematic, and hexagonal phases were obtained. The textures of the lyotropic phases were analyzed using a polarized optical microscope. The uniaxial to biaxial nematic phase transitions were obtained from the temperature dependences of the birefringences of the nematic phases via laser conoscopy technique. Small-angle X-ray Scattering was used to determine some micellar parameters. The results indicated that the formation of different lyotropic structures, especially biaxial nematic phases, is related to the average area surfactant head group. Those results were interpreted from the interactions between ionic species, considering their kosmotropic and chaotropic properties.

KEYWORDS: Lyotropic Liquid Crystals, Uniaxial Nematic Phase, Biaxial Nematic Phase, Lamellar Phase, Hexagonal Phase, Birefringence, Surfactant-Dye Molecule Interactions

ÖZET

SÜRFAKTAN BAŞ GRUP BÜYÜKLÜĞÜ İLE FARKLI TÜRDE LİYOTROPİK NEMATİK FAZ OLUŞUMLARI ARASINDAKİ İLİŞKİNİN İKİLİ SÜRFAKTAN/BOYAR MADDE SİSTEMLERİNDE ARAŞTIRILMASI
YÜKSEK LİSANS TEZİ
BARIŞ OKUYAN
BOLU ABANT İZZET BAYSAL ÜNİVERSİTESİ
LİSANSÜSTÜ EĞİTİM ENSTİTÜSÜ
KİMYA ANABİLİM DALI
(TEZ DANIŞMANI: PROF. DR. EROL AKPINAR)

BOLU, TEMMUZ - 2024
(xviii + 103)

Bu tez kapsamında; sürfaktan, Sunset Yellow, dodekanol ve sudan oluşan bazı liyotropik ikili sürfaktan karışımlarının özellikleri sabit toplam sürfaktan konsantrasyonlarında incelenmiştir. Sürfaktan molekülleri olarak dodesildimetilamonyum bromür (DDMABr), dodesildimetiletilamonyum bromür (DDMEABr) ve dodesiltrietilamonyum bromür (DTEABr) seçilmiştir. İkili sürfaktan karışımları DDEMABr/DDMABr ve DDMEABr/DTEABr'den oluşturulmuştur. Karışımlardaki her sürfaktanın göreceli konsantrasyonları değiştirilerek lamel, nematik ve hekzagonal fazlar veren liyotropik karışımlar elde edilmiştir. Liyotropik fazların dokuları polarize optik mikroskop kullanılarak analiz edilmiştir. Tek eksenliden çift eksenliye nematik faz geçişleri, lazer konoskopi tekniği ile nematik fazların çift kırılmalarının sıcaklığa bağımlılığından elde edilmiştir. Bazı misel parametrelerini belirlemek için Küçük Açılı X-ışını Saçılımı kullanılmıştır. Sonuçlar, farklı liyotropik yapıların, özellikle çift eksenli nematik fazların oluşumunun sürfaktan baş grubu başına düşen ortalama alanla ilişkili olduğunu göstermiştir. Bu sonuçlar, iyonik türlerin kozmotropik ve kaotropik özellikleri dikkate alınarak kendi aralarındak etkileşimleriyle yorumlanmıştır.

ANAHTAR KELİMELER: Liyotropik Sıvı Kristaller, Tek-Eksenli Nematik Faz, Çift Eksenli Nematik Faz, Lamel Faz, Hekzagonal Faz, Çift Kırınım, Sürfaktant-Boyar Molekül Etkileşimleri

TABLE OF CONTENTS

LIST OF FIGURES

Page

LIST OF TABLES

Page

LIST OF ABBREVIATIONS AND SYMBOLS

N	**:** Nematic phase
N_B	**:** Biaxial nematic phase
N_C	**:** Calamitic nematic phase
N_D	**:** Discotic nematic phase
H	**:** Hexagonal phase
L_α	**:** Lamellar phase
DDMEABr	**:** Dodecyldimethyethlylammonium bromide
DDMABr	**:** Dodecyldimethylammonium bromide
DTEABr	**:** Dodecyltriethylammonium bromide
SSY	**:** Sunset Yellow
DDeOH	**:** 1-Dodecanol
X	**:** Percent mole fraction
Δn/δn	**:** Birefringences
POM	: Polarize Optical Microscope
SAXS	**:** Small-angle X-ray Scattering
B	**:** Magnetic field
n	**:** Phase director or optical axis
CMC	**:** Critical micelle concentration
S	**:** Order Parameter
T_c	**:** Critical temperature
n_e	**:** Refractive index of extraordinary ray
n_o	**:** Refractive index of ordinary ray

ACKNOWLEDGEMENTS

The author wishes to express his deepest gratitude to his supervisor Prof. Dr. Erol AKPINAR for his guidance, advice, criticism, encouragements and insight throughout the research.

The technical assistance of Mrs. Nazlı UYGUR is gratefully acknowledged.

This study was supported by the The Scientific and Technological Research Council of TURKEY (TÜBİTAK), Grant No: 121Z084.

1. INTRODUCTION

Surfactants have hydrophilic and hydrophobic parts in their molecular structures (Figure 1.1), and they have been used in many industrial and biotechnological application areas due to the formation of the supramolecular structure, so-called ‘micelle’, in their solution environment (Figure 1.2) (1–6). These application areas include detergents, pharmacy, engine oils, emulsions, adhesives, inks, paints, etc. (7–11). They also have applications in textiles, food, cosmetics, and wetting/dispersing processes (8,12–15). In all these applications, low surfactant concentrations are generally necessary, and their aqueous solution properties have been widely investigated among researchers. Surfactants may form liquid crystal structures, which have potential biotechnological/biotechnological applications, at relatively high surfactant concentrations.

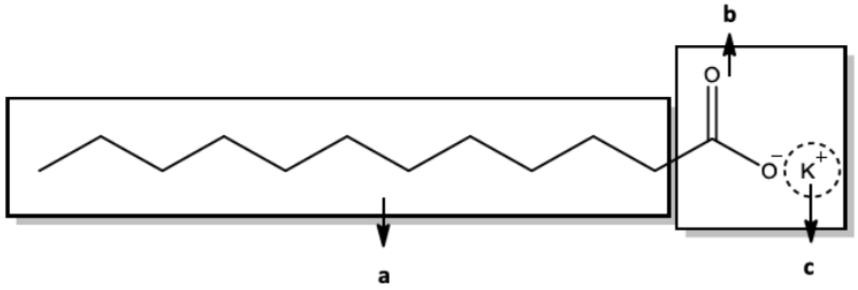

Figure 1.1. Surfactant molecule, potassium laurate. Part **a** is a water-insoluble hydrophobic part; **b** is an ionic head group, which is a water-soluble hydrophilic part; **c** is a counterion of the surfactant.

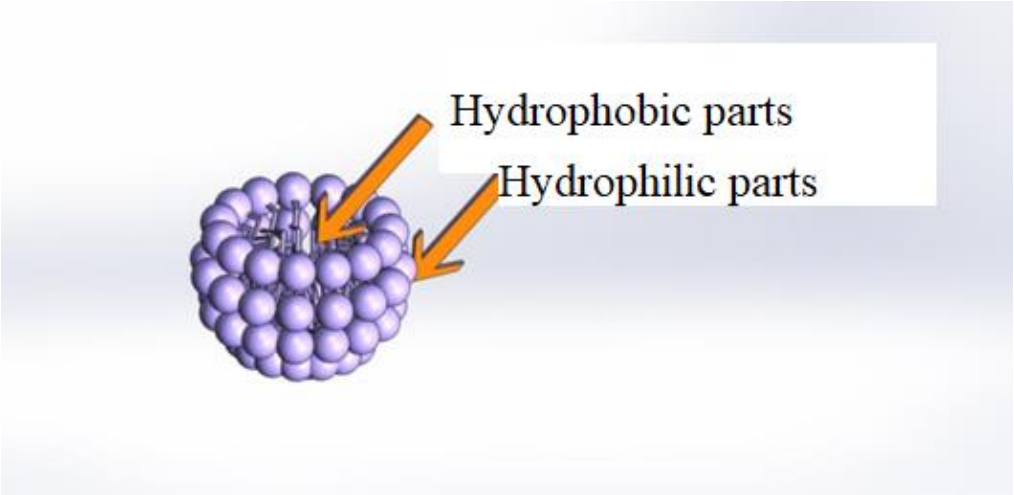

Figure 1.2. Schematic representation of a spherical micelle around the critical micelle concentration.

Surfactant molecules are surrounded by solvents (e.g. water) at their low concentrations in solutions. When surfactants are dissolved in water, first they are adsorbed at the air/water interface by reducing the surface tension of the solution with their hydrophobic parts oriented towards the air, and their hydrophilic parts are in contact with water molecules at the interface. Then, after the surface of the solution is saturated by surfactant molecules, further addition of the surfactant causes the transfer of the excess surfactant molecules in the bulk solution and they self-assemble to form micelles at a certain concentration (critical micelle concentration, cmc), Figure 1.3.

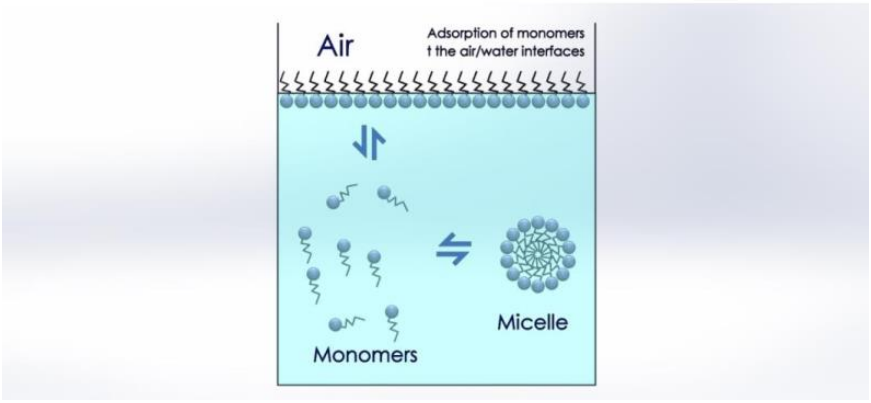

Figure 1.3 Schematic representation of micelle formation via dynamic equilibrium among air/water interface adsorbed surfactant monomers, surfactant monomers in water and micelles.

Surfactants may form different micelles in shape, depending on the aggregation type of surfactant molecules in the micelles. The most common micelle structures and their geometries are given in Figure 1.4. Some factors affect the micellization of surfactants. The important ones are pH, temperature, additives (e.g. electrolytes), solvent, and surfactant types, etc (16–18). For instance, when an electrolyte is added to the solution, its oppositely charged ions with respect to the charge of the surfactant head group bind to the micelle surfaces and reduce the repulsions between the head groups, which favors the micellization, i.e. cmc decreases.

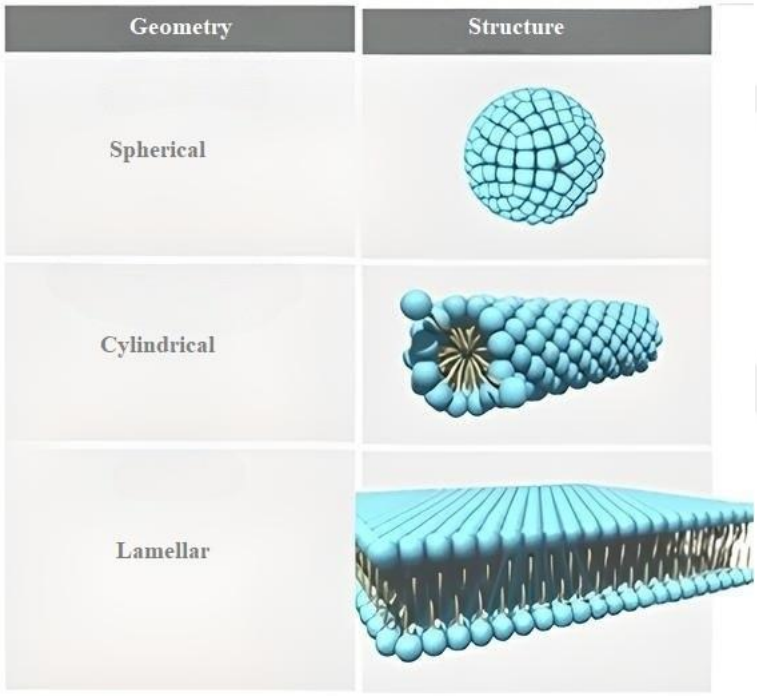

Figure 1.4 The most common micelle structures in micellar solutions.

At around cmc of the surfactants, the micelles are spherical and optically isotropic. At high surfactant concentrations, the micelles turn into more anisometric (cylindrical, lamellar, orthorhombic, etc.) to form optically anisotropic liquid crystal structures.

1.1 Liquid Crystals

The main difference between the solid and liquid states of matter is that the atoms or molecules in a solid are in an ordered state, whereas, in a liquid, they are not as shown in Figure 1.5. Solids have both orientational and positional orders, i.e., the molecules occupy specific positions, and their molecular axes are in certain directions. Contrarily, the molecules in liquids tend to take the shape of the container, and their molecular axes constantly change (rotating, tumbling, oscillating). There exists a phase in nature between these two states of matter, which has more order than the liquid but less than the solid. This phase is called 'Liquid Crystal' and has properties associated with both solid and liquid. The substances in all liquid crystal phases diffuse like the molecules of a liquid, but while doing this, the degree of fluctuating orientational order and local positional order is maintained. However, the degree of order in liquid crystal is lower than that in solid. This relatively small amount of order in liquid crystals has caused them to acquire some properties specific to solids, such as mechanical, electrical, magnetic, and optical properties. Due to these properties of liquid crystals, they have attracted the attention of scientists. Liquid crystal phases are thermodynamically stable thus putting them on equal footing with the solid, liquid, and gas phases.

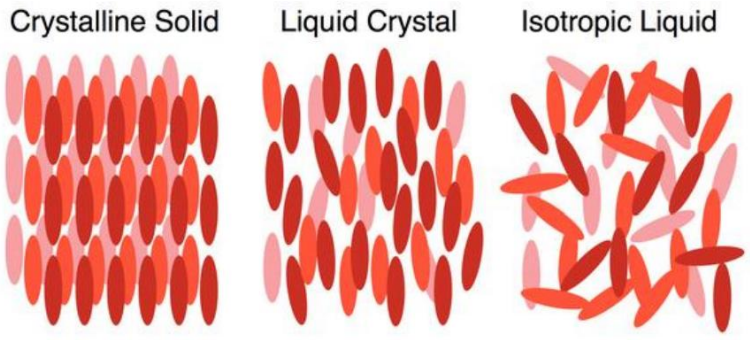

Figure 1.5 Schematic representation of molecular arrangment of crystalline solid, liquid crystal and isotropic liquid.

The simplest liquid crystal phase is nematic. As the molecules undergo diffusion, the molecular axes tend to point along a preferred direction. This preferred direction is called the phase director or optical axis and is denoted by the

unit vector $\vec{n}$, where $\vec{n} = -\vec{n}$, because the preferred direction can be defined to be in either of two opposite directions. The degree of order in such a liquid crystal phase is described by order parameter (S) (Equation 1.1). The most useful formulation is to find the average of a specific function of θ called the second Legendre polynomial, $P_2(\cos\theta)$, where the brackets denote an average over many molecules at the same time or an average over time for a single molecule. Figure 1.6

$$S = \langle P_2(\cos\theta)\rangle = \left\langle \frac{3}{2}\cos^2\theta - \frac{1}{2} \right\rangle \tag{1.1}$$

Figure 1.6 Molecular order in a nematic liquid crystal. The vertical arrow represents the director and the arrow at an angle θ to the director represents the long axis of one of the molecules.

The value of S is equal to zero when the mesomorphic system is disorder completely, i.e., isotropic liquid state and the value of S is equal to in a completely ordered system, i.e., solid crystal state. The order parameters of liquid crystal, in general, take a value between 0.3 to 0.9. Liquid crystal systems become completely disordered at temperature which is called critical temperature, T_c. Figure 1.7 shows the variation of order parameters depending on the temperature.

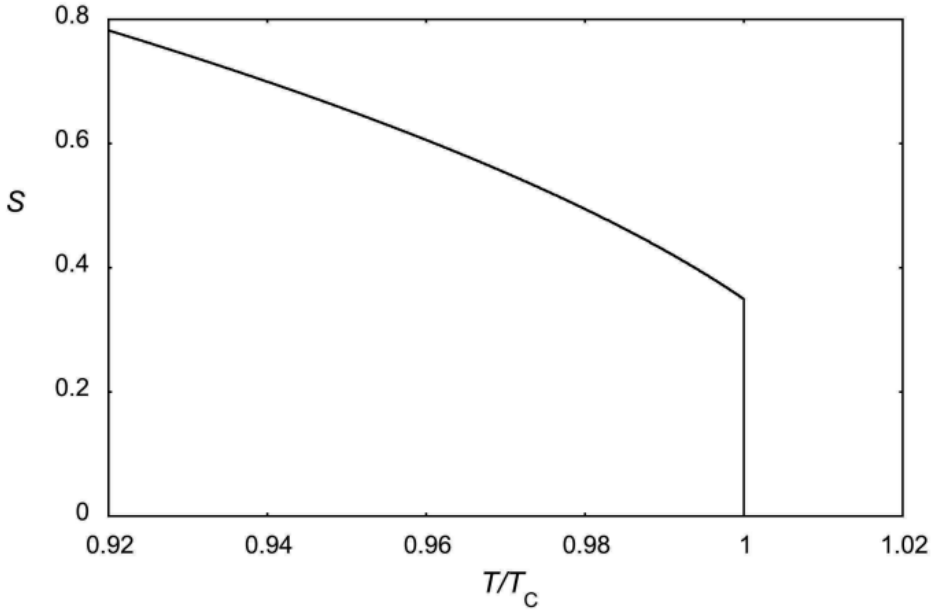

Figure 1.7 Representation of the change in the order parameter of a liquid crystal substance with temperature.

In general, liquid crystals are classified into two sub-classes: thermotropic liquid crystals and lyotropic liquid crystals. Thermotropic liquid crystals are only observed with the effect of temperature, as the name suggested. However, lyotropic liquid crystals depend on both the concentration of surfactant molecules and temperature in the proper solvent (in general, water) (19).This is the main difference between the two types of liquid crystals.

1.1.1 Lyotropic Liquid Crystals

Lyotropic liquid crystal structures are obtained depending on the structure and organization of the micelles. The most important structures are lamellar, hexagonal, and nematic phases. In addition, temperature, pH, magnetic field, type of surfactant, and additives affect the structure of the lyotropic liquid crystals (16–18). The micelle structures formed by surfactant molecules in these phases are schematically shown in Figure 1.8, and the characteristic phase textures obtained under the polarized optical microscope are given in Figure 1.9.

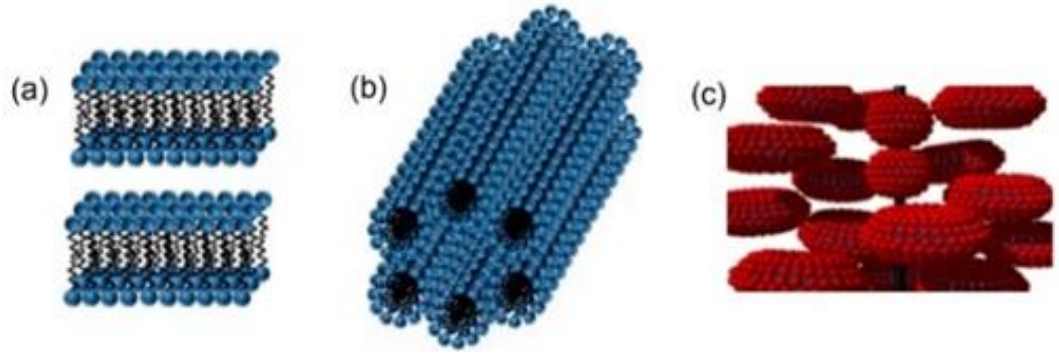

Figure 1.8. (a) In the lamellar phase, surfactants cluster as an infinitely wide double layer. Surfactant alkyl chains (shown in black) are located inside the bilayer and polar or ionic surfactant head groups (shown in blue sphere) are located on the surface. There is a water region between the double layer. (b) In the hexagonal phase, there are infinitely long cylindrical micelles. (c) Nematic phase with disk-shaped micelles. Red spheres symbolize the surfactant head groups on the micelle surface.

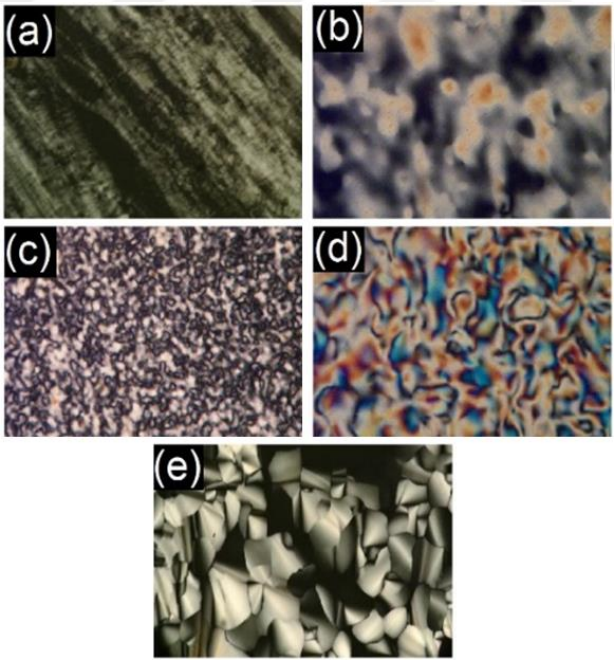

Figure 1.9. Lyotropic (a) lamellar, (b) discotic nematic, N_D, (c) biaxial nematic, N_B, (d) calamitic nematic, N_C, and (e) hexagonal phase textures observed under the polarized optical microscope (20).

Among the surfactant-based lyotropic liquid crystals, nematic phases have a special place due to the existence of the preferred orientational properties. The nematic phases were first introduced to the literature in 1967 (21), then their phase diagrams and physicochemical properties depending on temperature and/or concentration have been examined in many studies (22–28). In general, lyotropic mixtures giving a nematic phase are obtained by dissolving surfactant molecules in water. In many cases, electrolyte or a co-surfactant or both are added to such mixtures (27,29). In terms of the optical axes of the micelles, lyotropic nematic phases are known as uniaxial (discotic nematic, N_D, and calamitic nematic, N_C) and biaxial nematic (N_B) phases. Since the first experimental introduction of biaxial lyotropic nematic phases into the literature in 1980 (30), until today, there is still no full consensus on the existence of these phases. One of the most important reasons for this is that researchers have not been able to find a sufficient amount of lyotropic mixtures that give a biaxial nematic phase. Furthermore, a limited number of models have been proposed in the literature to explain the formation of both biaxial and uniaxial nematic phases. The most useful model was proposed by Antonio and Galerne, which is called 'Instrinsically Biaxial Micelles, IBM' model (31). In the IBM model, it is suggested that micelles are flattened in shape with orthorhombic symmetry and the orientational fluctuations are responsible for the formation of different nematic phases. Another important problem is that it has not been fully determined which parameters or factors play a role in the formation of these phases and in obtaining a wide range of biaxial nematic phases in phase diagrams.

Uniaxial and biaxial lyotropic nematic phases are described with different symmetry: while uniaxial N_D and N_C phases have $D_{\infty}h$ symmetry, and N_B phase has D_{2h} symmetry (32–35). In the case of uniaxial nematic phases, the local symmetry axes of micelles show an average orientation along the direction of the phase director or optical axis ($\vec{\boldsymbol{n}}$). Biaxial nematic phases have two optical axes and three perpendicular two-fold symmetry axes ($\vec{\boldsymbol{l}}$, $\vec{\boldsymbol{m}}$ and $\vec{\boldsymbol{n}}$, where $\vec{\boldsymbol{n}} = \vec{\boldsymbol{l}} \times \vec{\boldsymbol{m}}$) (34,36), and it has been suggested by strong experimental results that all three lyotropic nematic phases consist of micelles with the same orthorhombic symmetry. Furthermore it has been observed that the N_B phase regions are

generally located between the other two uniaxial nematic phase regions in the phase diagrams of mixtures giving all three nematic phases (30,35,37). As suggested theoretically according to the Landau type mean field theory and experimentally proven by many studies, the transitions from uniaxial nematic phases to biaxial nematic phases are of second-order (30,35,37,38).

It is known from the literature that lyotropic nematic phases like lamellar and hexagonal ones have some technological/biotechnological applications (39). For example, nematic phases are used for obtaining thin film E-type polarizers (Extraordinary mode polarizers) in vertically aligned liquid crystal devices (40). Additionally, lyotropic nematic phases have a high potential to contribute to drug delivery systems (41) and future applications in biotechnology and medicine (42). Another application of lyotropic nematic phases in biotechnology is the commercial biomedical product "magnetic latex" used for cell labeling and cell sorting due to the magnetic particles added to the medium (43,44). In addition, one of the commercialized applications of magnetic nanoparticles is magnetic resonance imaging, where hybrid systems obtained by adding these particles to a medium act as contrast agents (45–48).

Other important application areas of lyotropic nematic phases are nanoscale electronics (49,50), field-emission sources (50,51), local drug release at the molecular level through technological and biological molecule detection (52,53) such as actuators (54,55). Lyotropic nematic phases serve as a carrier or guiding solvent/medium (56) for carbon nanotubes, which are used as nanosensors.

Surfactants are also used in systems containing dye molecules. Since surfactant/dye molecule interactions have an important place in industrial and biotechnological applications, such interactions have been extensively studied in dilute surfactant/dye aqueous solutions (57–62). The role of such interactions in the stabilization of lyotropic nematic phases was examined for the first time by Akpinar et al., 2020, 2021 (63,64). The results showed that the Sunset Yellow dye molecule is more effective in the stabilization of nematic phases and obtaining a wide biaxial nematic phase region in partial phase diagrams than the traditional

inorganic electrolyte ions. Furthermore, it was observed that the area per surfactant head group on the micellar surfaces (a_0) is a very important parameter in obtaining nematic phases. Mitchell and his colleagues suggested that there may be a relationship between the formation of different types of lyotropic structures or micelle shapes and a_0 values (65,66). However, in the references, the formation of the biaxial nematic phase was ignored because there were not enough studies to prove the existence of that phase. The data obtained from Akpinar et al., 2020, 2021 has shown, for the first time in the literature, that a biaxial nematic phase can be obtained from mixtures of surfactants with 52 $Å^2 \geq a_0 > 57$ $Å^2$ in the binary surfactant systems of dodecyl trimethylammonium bromide (DTMABr)/ dodecylalkylammonium bromides. Their study only dealt with nematic phases, but not hexagonal and/or lamellar phases (63,64).

1.1.2 Optical and Magnetic Properties of Liquid Crystals

Liquid crystals are anisotropic materials, meaning that their physical properties differ when measured parallel or perpendicular to the alignment of their structural units. When polarized light passes through an anisotropic liquid crystal, it splits into two plane-polarized rays (ordinary and extraordinary rays) that travel at different velocities, resulting in different refractive indices. This phenomenon is called birefringence or double refraction (Δn). The birefringence (Δn) is defined as the difference between the refractive indices of the extraordinary (n_e) and ordinary rays (n_o) as shown in Figure 1.10.

$$\Delta n = n_e - n_o \qquad 1.2$$

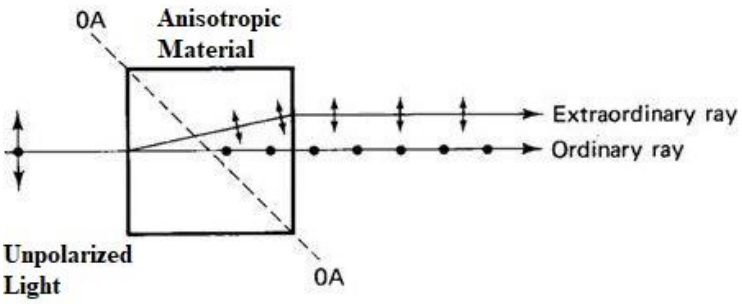

Figure 1.10 The light passing through anisotropic material (e.g. liquid crystal) double refraction scheme; an extraordinary ray (E-ray) is polarized perpendicular to the optic axis and experiences a different index of refraction than the ordinary

Under a polarizing optical microscope, conoscopic investigations help to determine the sign of optical anisotropy (Δn). In nematic phases, alignment of the phase director perpendicular or parallel to a magnetic field yields homeotropic or planar textures, respectively Figure 1.11. The sign of birefringence can be observed using interference colors with a ¼ retardation plate. If the laboratory frame axes are selected along 1, 2, and 3 directions, which are orthogonal to each other, the axis-3 is perpendicular to the 1-2 plane. Uniaxial nematics have one birefringence, while biaxial nematics have two, described by $\Delta n = n_2 - n_1$ and $\delta n = n_3 - n_2$ where $n_1 \neq n_2 \neq n_3$. If $n_3 - n_2 > n_2 - n_1$, the biaxial phase has positive birefringence . In the contrast case, i.e. $n_3 - n_2 < n_2 - n_1$, the biaxial phase is described with negative birefringence (67).

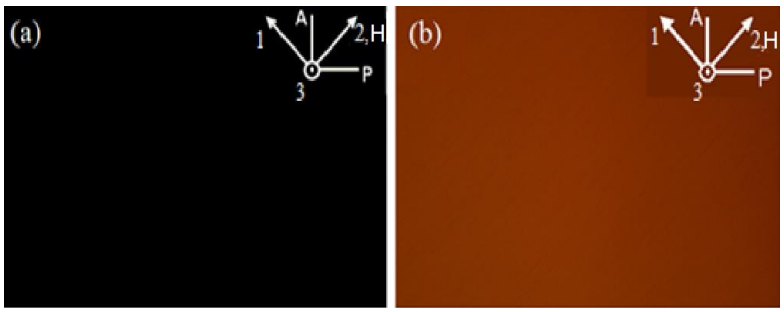

Figure 1.11 Properly aligned homeotropic and planar textures of uniaxial (a) N_D and (b) N_C phases, respectively. A and P are analyzer and polarizer, respectively. H: magnetic field direction; 1, 2, and 3 are the laboratory frame axes.

Conoscopic images reveal optical anisotropy, with uniaxial crystals show a dark-corss (Maltese cross) and the center of the dark cross is named melatope. In this dark cross consist of two L shaped fingers (isogyres) and colored concentric

fringes (isochromes) (67). Biaxial crystals display two melatopes as shown Figure 1.12. Laser light can also be used to investigate optical properties, where the application of an electric field can induce biaxial behavior.

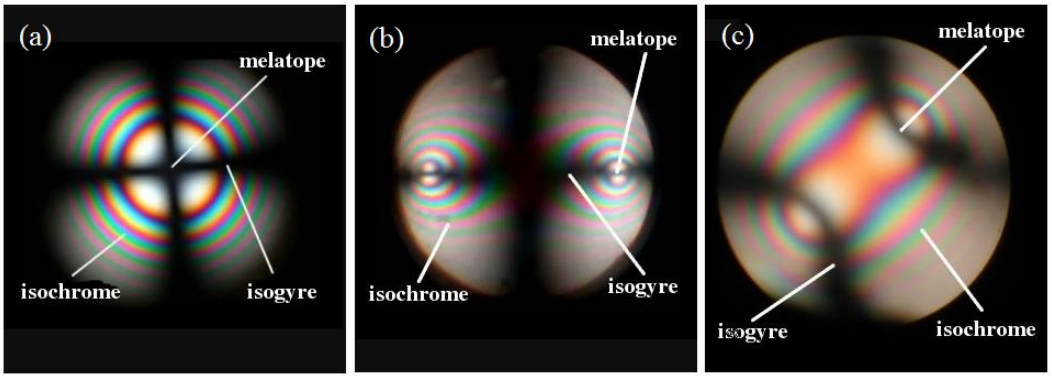

Figure 1.12 Images of dark cross **c**onoscopic interference of a (a) uniaxial crystal, (b) biaxial crystals and (c) biaxial with 45° rotation (68)

Wang demonstrated the study of the optical properties of uniaxal crystals using polarized optical microscopy (69). In this study, they managed to obtain conoscopic interference images by applying the electric field shown in Figure 1.13. When the electric field strength is incresead, the conoscopic interference pattern is changed from uniaxal phase to the biaxial phase. Similar results were reported in the reference (70), Figure 1.14. These laser conoscopic interference images are quite similar to those produced by our laser conoscopy set-up. However, in our thesis, a magnetic field is applied instead of an electric field, and hyperbolic isogyres are observed at 0° rotation (i.e., no rotation) due to the experimental design.

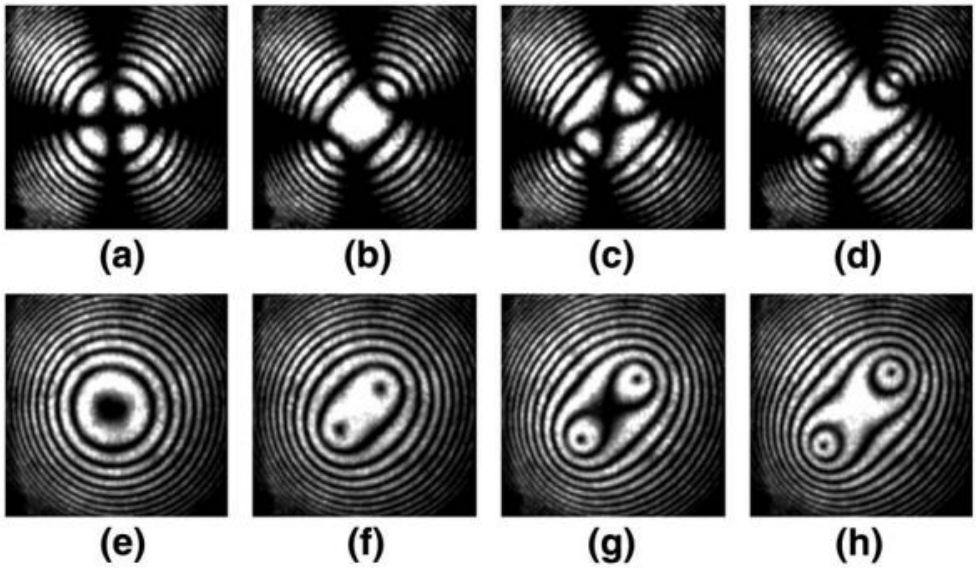

Figure 1.13 Conoscopic interference images of LiNbO3 at different voltages. (a) and (e), V= 0; (b) and (f), V =Vπ; (c) and (g), V = 2Vπ; (d) and (h), V = 3Vπ. In (e)–(h) the spinning polarizer and analyzer method is employed. (69).

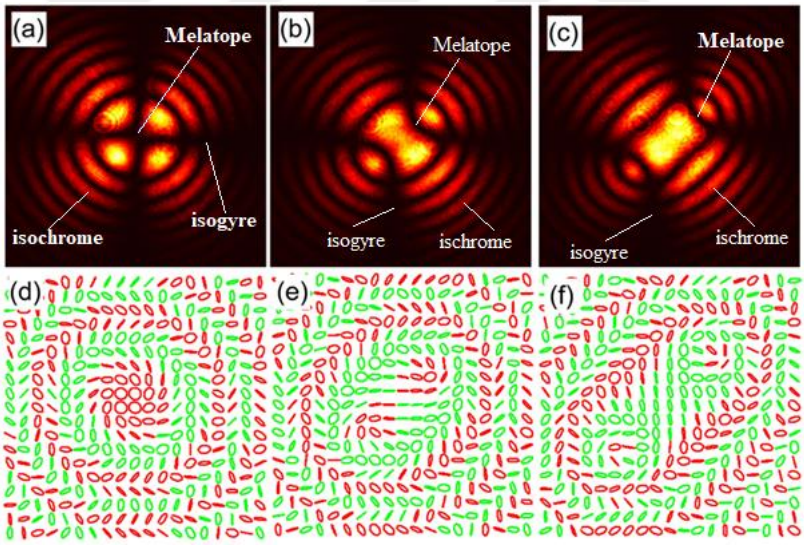

Figure 1.14 Conoscopic interference pattern (first row) and the polarization ellipse map (second row) of the output beam for different applied fields, E_x = 0 V/*m* (a,d), $E_x = 0.7 \times 10^2$ V/ *m* (b,e) and $E_x = 2 \times 10^2$ V/ *m* (c,f) (70).

Liquid crystals are diamagnetic, and their magnetization (M) is proportional to the magnetic field strength (B) with magnetic susceptibility (χ) being negative. The diamagnetic susceptibility anisotropy ($\Delta\chi$) is defined by the difference in magnetic susceptibilities measured parallel ($\chi_{//}$) and perpendicular ($\chi_{\perp}$) to the optical axis. Positive (negative) $\Delta\chi$ means alignment parallel to the

magnetic field, while negative $\Delta\chi$ means perpendicular alignment. Generally, the signs of optical anisotropy (Δn) and diamagnetic susceptibility anisotropy ($\Delta\chi$) are opposite. Biaxial nematic phases have three two-fold magnetic susceptibilities, and their alignment depends on the sign of $\Delta\chi$.

2. AIM AND SCOPE OF THE STUDY

Lyotropic liquid crystal structures are widely studied by many researchers in the literature. In a recent study, Akpinar et. al., 2020 examined the effect of the anionic azo dye Sunset Yellow (SSY) on the lyotropic nematic properties of dodecytrimethylammonium bromide (DTMABr)/dodecanol/water mixtures by comparing its effect with some inorganic electrolytes and showed that Sunset Yellow dye binds to the micelle surfaces by interacting with the surfactant head groups like electrolyte ions. Furthermore, they revealed the chaotropic property of SSY for the first time. The same authors also investigated the presence of SSY in lyotropic mixtures of some binary DTMABr/dodecylalkylammonium bromide surfactants (64). However, in both studies, the author limited their studies to the formation of **only nematic phases** from the investigation of specific interactions at the micelle surface point of view.

In this thesis, we aimed to investigate the effect of the interactions between SSY and surfactant head group on the formation of the lamellar and hexagonal phases in addition to that of the nematic phases. In this way, unlike the studies in the literature (63–65), the effect of the change in the average area per surfactant head groups, which is a result of the specific interactions between the anionic parts of the SSY and the ionic head groups of the surfactants, on the phase sequence of lamellar → discotic nematic → biaxial nematic → calamitic nematic → hexagonal was revealed in a different binary surfactant systems of dodecyldimethylethylammonium bromide(DDMEABr)/ dodecyl-dimethylammonium bromide (DDMABr) and DDMEABr/dodecyltriethylammonium bromide (DTEABr).

3. MATERIALS AND METHODS

3.1 Chemicals

Three surfactant molecules were selected for the experimental parts of this thesis. Among them, dodecyldimethylethylammonium bromide (DDMEABr) was purchased commercially with a minimum purity of 98% (Sigma). Dodecyldimethylammonium bromide (DDMABr) and dodecyltriethylammonium bromide (DTEABr) were synthesized in our research laboratory according to the procedure given below.

Sunset Yellow was provided commercially with a minimum purity of 90%, and purified before its use to increase its purity to >99% (71,72). This purification method includes first dissolution of Sunset Yellow in a minimum amount of pure water, and then precipitation by adding absolute ethanol. Finally, it is obtained in pure form by filtration and vacuum drying. The same purification method was applied 3 times.

Ultrapure water was used in the preparation of lyotropic samples and it was provided from the Millipore Direct-Q3 UV purification system with a resistivity of 18.2 MΩ.cm at 25ºC. Dodecanol (DDeOH) was commercially available from Sigma-Aldrich with 99% purity.

3.2 Synthesis Procedure and Characterization of Surfactants

DDMABr and DTEABr molecules were synthesized (see below for details) and characterized by IR and NMR techniques. ^{1}H-NMR measurements were obtained from solutions of surfactant molecules in $CDCl_3$. IR and NMR spectroscopy results of both molecules are given below. Commercially available DDMEABr was also characterized to compare its IR and NMR spectra with the synthesized molecules (Figures 3.1 and 3.2). As can be seen, the spectra of DDMABr (Figures 3.3-3.4) and DTEABr (Figures 3.5-3.6) are quite compatible with DDMEABr.

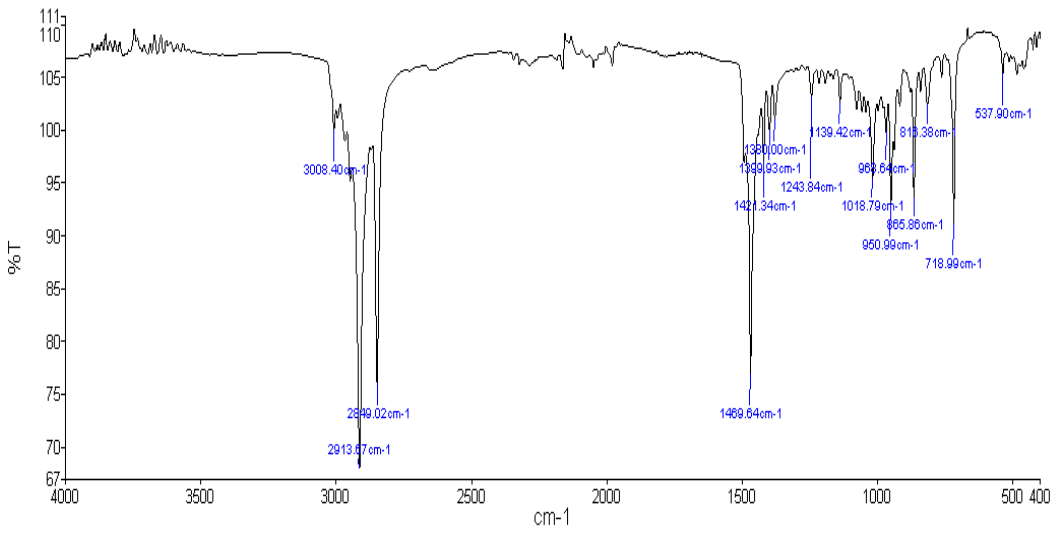

Figure 3.1. FTIR spectrum of DDMEABr.

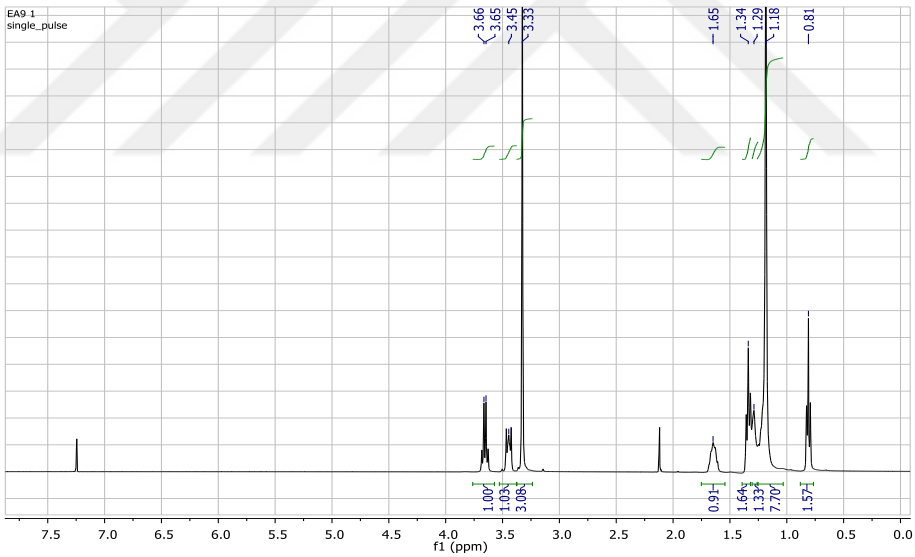

Figure 3.2. 400 MHz ^{1}H NMR spectrum of DDMEABr (solvent: $CDCl_3$) ^{1}H NMR (400 MHz), δ (ppm, $CDCl_3$): 0.81 (CH_3, 3H, t), 1.18 (CH_2, 14H, br m), 1.29 (CH_2, 2H, br m), 1.34 (CH_3, 3H, t), 1.65 (CH_2, 2H, br m), 3.33 (N^+CH_3, 6H, s), 3.45 (N^+CH_2, 2H, t), 3.66 (N^+CH_2, 2H, q).

3.2.1 Synthesis of dodecyldimethylammonium bromide

0.3237 mol dodecyldimethylamine is dissolved in 136 mL of ethanol in a 500 mL beaker by stirring on a magnetic stirrer and 40.00 mL (0.3462 mol) HBr(aq) is added. After the addition of all HBr(aq) is completed, the reaction vessel (beaker) is cooled by placing it in an ice bath and then placed in the deep freezer at –18°C for one day to precipitate dodecyldimethylammonium bromide. The product is separated from the solution by vacuum filtration and purified by recrystallization from chloroform/diethylether at least three times. Then, it is dried thoroughly in a vacuum oven at 40°C.

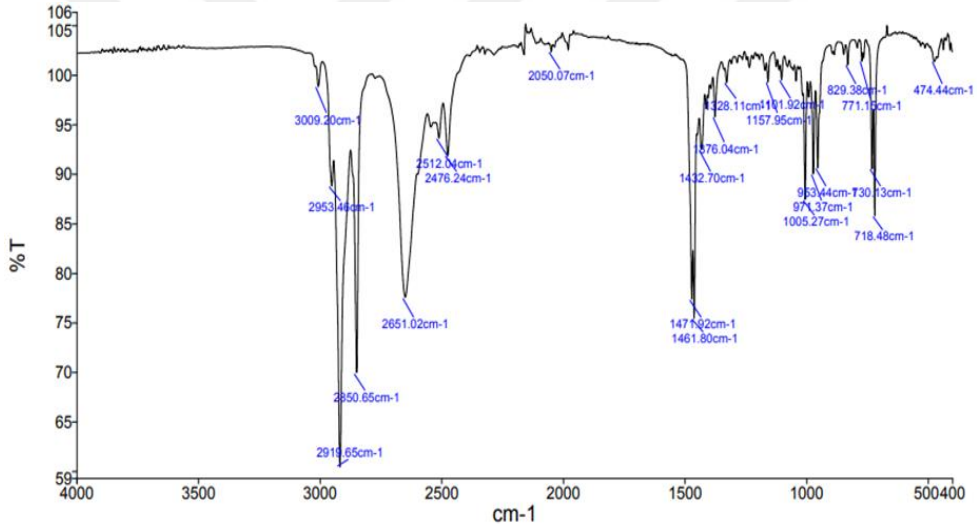

Figure 3.3. FTIR spectrum of DDMABr.

Figure 3.4. 400 MHz ^{1}H NMR spectrum of DDMABr (solvent: $CDCl_3$); ^{1}H NMR (400 MHz), δ (ppm, $CDCl_3$): 0.83 (CH_3, 3H, t), 1.20-1.29 (CH_2, 18H, br m), 1.78-1.86 (CH_2, 2H, m), 2.79 (N^+CH_3, 6H, t), 2.99 (N^+CH_2, 2H, t), 11.17 (N^+H, 1H, br s).

3.2.2 Synthesis of dodecyltriethylammonium bromide

0.33 mol of triethylamine is added to 0.30 mol of 1-bromododecane dissolved in 150 mL of ethanol in a 500 mL round-bottomed two-necked flask, and then the reaction mixture is refluxed. The reflux is carried out (for approximately two days) until all 1-bromododecane is consumed, which is checked by TLC occasionally. After the reaction is completed, the reaction flask is allowed to cool at room temperature followed by the removal of ethanol as much as possible with a rotary evaporator. Diethyl ether is added to the remaining concentrated ethanol-product solution and kept in the deep freezer at –18°C for a day. Dodecyltriethylammonium bromide, which precipitates as a white solid, is obtained by filtration under vacuum. Then, it is recrystallized from chloroform/diethyl ether at least three times and dried thoroughly in a vacuum oven at 40°C.

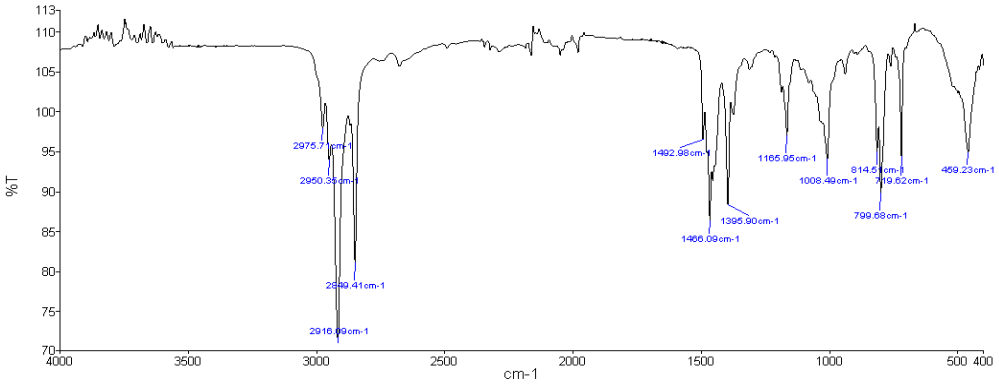

Figure 3.5. FTIR spectrum of DTEABr.

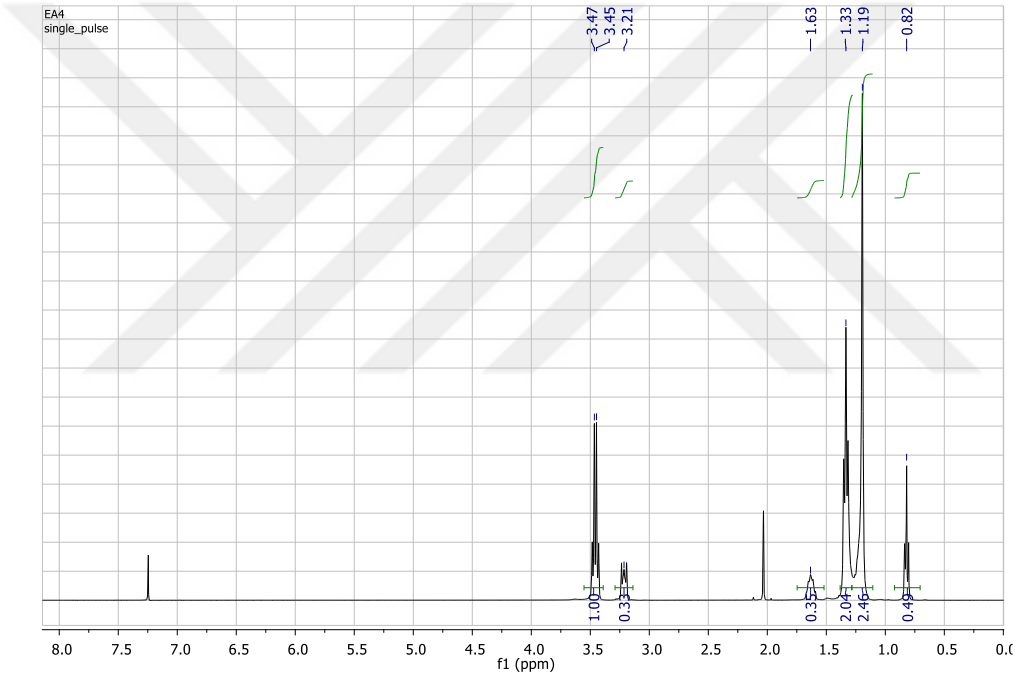

Figure 3.6. 400 MHz ^{1}H NMR spectrum of DTEABr (solvent: $CDCl_3$) 1H NMR (400 MHz), δ (ppm, $CDCl_3$): 0.82 (CH_3, 3H, t), 1.19 (CH_2, 18H, br m), 1.33 (CH_3, 9H, t), 1.59-1.67 (CH_2, 2H, m), 3.21 (N^+CH_2, 2H, t), 3.46 (N^+CH_2, 6H, q).

3.3 Experimental Techniques/Methods

3.3.1 Preparation of Lyotropic Liquid Crystal Mixtures

Lyotropic liquid crystal mixtures were prepared by weighing the required amounts of each component (surfactant, co-surfactant, Sunset Yellow, and water) in capped glass test tubes at appropriate concentrations using a precision balance (Radwag, ±0.00001 g). After the weighing process was completed, mixing with a vortex (Ika) and centrifugation (Hettich) processes were applied several times to homogenize them. Because highly oriented nematic phases are necessary for laser conoscopy, polarized optical microscopy, and small-angle X-ray scattering measurements, a water-based ferrofluid (Ferrotec, EMG-607) was added at 1 μL per 1 g of lyotropic mixtures in the presence of the magnetic field (~2.0, ~1.0 kG and ~1.0 kG, respectively). Previous experiments in the literature showed that the addition of ferrofluid in these amounts does not cause any deformation in the phase structure or any error in measurements (27,73).

The host mixture (s0) consists of DDMEABr/SSY/DDeOH/water. By keeping the total composition of the mixtures and the total surfactant concentration constant, the amount of DDMEABr was replaced by DDMABr and DTEABr, separately, in some portions (in mole fraction). The binary surfactant mixtures were prepared at 15 different DDMEABr/DDMABr (mixtures s1-s15) and DDMEABr/DTEABr (mixtures s17-s31) in percent mole fraction, i.e. total of 30 mixtures. Furthermore, the mixtures with single surfactant (100% DDMABr; s16 and 100% DTEABr; s32) were also prepared.

Compositions of DDMEABr/DDMABr/Sunset Yellow/DDeOH/water and DDMEABr/DTEABr/Sunset Yellow/DDeOH/water single and binary surfactant mixtures are given in Tables 3.1 and 3.2, respectively. These mixtures were used for polarizing optical microscopy, laser conoscopy, and small-angle X-ray Scattering (SAXS) measurements.

Table 3.1 Compositions of DDMEABr/DDMABr/Sunset Yellow/DDeOH/water binary surfactant samples. X corresponds to the percent mole fraction of each component. s0 and s16 mixtures were composed of single surfactants.

Sample	$X_{DDMEABr}$	X_{DDMABr}	X_{SSY}	X_{DDeOH}	X_{water}
s0	5.218	0.000	0.131	2.131	92.519
s1	5.114	0.104	0.131	2.131	92.519
s2	5.010	0.209	0.131	2.131	92.519
s3	4.905	0.313	0.131	2.131	92.519
s4	4.801	0.417	0.131	2.131	92.519
s5	4.697	0.522	0.131	2.131	92.519
s6	4.592	0.626	0.131	2.131	92.519
s7	4.488	0.731	0.131	2.131	92.519
s8	4.175	1.044	0.131	2.131	92.519
s9	3.653	1.566	0.131	2.131	92.519
s10	3.131	2.087	0.131	2.131	92.519
s11	2.609	2.609	0.131	2.131	92.519
s12	2.087	3.131	0.131	2.131	92.519
s13	1.566	3.653	0.131	2.131	92.519
s14	1.044	4.175	0.131	2.131	92.519
s15	0.522	4.697	0.131	2.131	92.519
s16	0.000	5.218	0.131	2.131	92.519

Table 3.2 Compositions of DDMEABr/DTEABr/Sunset Yellow/DDeOH/water binary surfactant samples. X corresponds to the percent mole fraction of each component. s32 mixture was composed of a single surfactant.

Mixture	$X_{DDMEABr}$	X_{DTEABr}	X_{SSY}	X_{DDeOH}	X_{water}
s0	5.218	0.000	0.131	2.131	92.519
s17	5.114	0.104	0.131	2.131	92.519
s18	5.010	0.209	0.131	2.131	92.519
s19	4.905	0.313	0.131	2.131	92.519
s20	4.801	0.417	0.131	2.131	92.519
s21	4.697	0.522	0.131	2.131	92.519
s22	4.592	0.626	0.131	2.131	92.519
s23	4.488	0.731	0.131	2.131	92.519
s24	4.175	1.044	0.131	2.131	92.519
s25	3.653	1.566	0.131	2.131	92.519
s26	3.131	2.087	0.131	2.131	92.519
s27	2.609	2.609	0.131	2.131	92.519
s28	2.087	3.131	0.131	2.131	92.519
s29	1.566	3.653	0.131	2.131	92.519
s30	1.044	4.175	0.131	2.131	92.519
s31	0.522	4.697	0.131	2.131	92.519
s32	0.000	5.218	0.131	2.131	92.519

3.3.2 Polarized Optical Microscopy (POM)

The phase textures of lyotropic liquid crystal samples prepared within the scope of this thesis were characterized by a Nikon Eclipse Ci-POL (Nikon, Japan) polarized optical microscope. For these measurements, well-homogenized liquid crystal samples were transferred into a flat capillary tube or microslide (Vitrocom, Japan) with a thickness of 0.2, 0.3, and/or 0.4 mm. Both ends of the microslides (capillaries) were coated with a special fluidic nanocomposite (DLine, Lithuania) and then UV light was applied to prevent water loss. Microslides containing lyotropic liquid crystal samples were placed in a temperature control unit (Linkam LTS120E, 0.1°C precision) and homogeneous heat distribution was provided by a circulating water bath (Polyscience) connected to this temperature control unit. The phase textures of lyotropic liquid crystal samples were recorded with a digital microscope camera (DFK41AU02, The Imaging Source, Germany) and characterized with special software (NIS-Element-D computer software, Nikon). The samples were placed in the temperature control unit in a position of 45° concerning both the analyzer and polarizer, Figure 3.7.

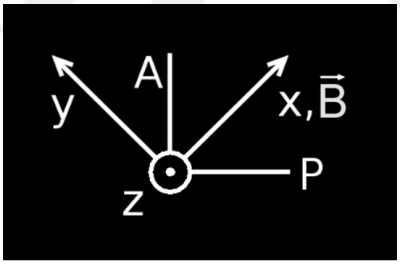

Figure 3.7 Selected measurement configuration for texture analysis of lyotropic samples under polarized optical microscopy: x, y, z selected laboratory coordinate axes; A and P are analyzer and polarizer directions, respectively; **B** indicates the direction of the magnetic field. The long axis of the capillary containing the lyotropic liquid crystal samples was placed parallel to the y-axis (perpendicular to the magnetic field direction).

3.3.3 Laser Conoscopy Measurements

Lyotropic nematic phases are characterized by two different optical birefringences (Δn and δn): $\Delta n = n_2 - n_1$ and $\delta n = n_3 - n_2$. Here, n_1, n_2, and n_3 are the refractive index values of the medium along the three perpendicular laboratory frame axes (1, 2, and 3). While birefringence can only be measured in one

direction (Δn) using a Berek or Senarmont compensator under a polarized optical microscope, birefringence values (Δn/δn) of micelles with orthorhombic symmetry in both directions can be calculated with laser conoscopy. In addition, laser conoscopy is a method that provides very useful and sensitive results in determining the second-order phase transition temperatures between uniaxial and biaxial nematic phases.

Laser conoscopy measurements were applied starting from the well-aligned N_D phase in the presence of the magnetic field (Figure 3.8a). It is a crucial point that the N_D phase must be fully oriented in these measurements. Uniaxial-to-biaxial nematic phase transitions were determined from the temperature dependence of the birefringence values of each nematic phase. Figure 3.7 shows the interference patterns observed for three nematic phases in the screen of the laser conoscopy set-up.

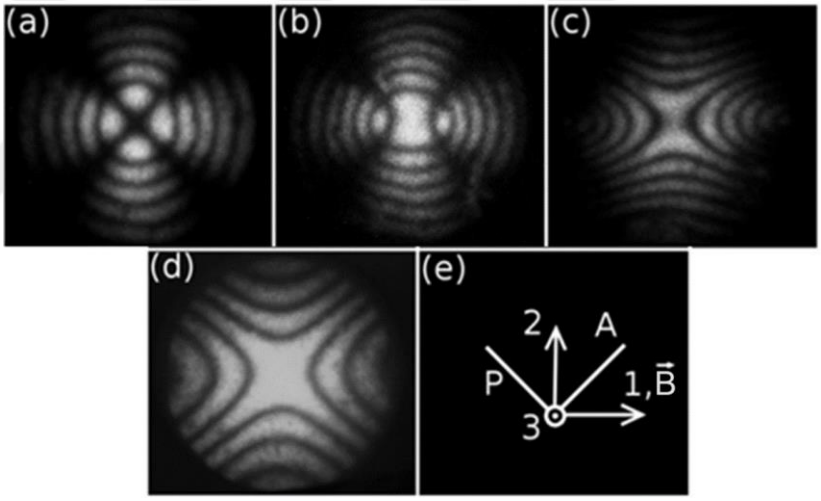

Figure 3.8 Interference patterns of (a) N_D, (b) N_B around N_D-N_B phase transitions, (c) N_B around N_B-N_C phase transitions, and (d) N_C phases obtained from laser conoscopy by changing the temperature. (d) 1, 2, and 3 are laboratory frame axes; A and P are analyzer and polarizer directions, respectively; **B** indicates the direction of the magnetic field. The optical direction of the laser light beam directed on the sample is parallel to the axis-3 direction.

In laser conoscopy measurements, lyotropic liquid crystal samples were placed between two circular optical glasses (Helma) with a diameter of 2.5 cm, using a 2.5 mm thick glass ring. Then, measurements were made by placing the sample in a specially designed sample holder. After the measurements are

completed, birefringence values were calculated depending on the temperature with a specially developed computer software (Figure 3.9).

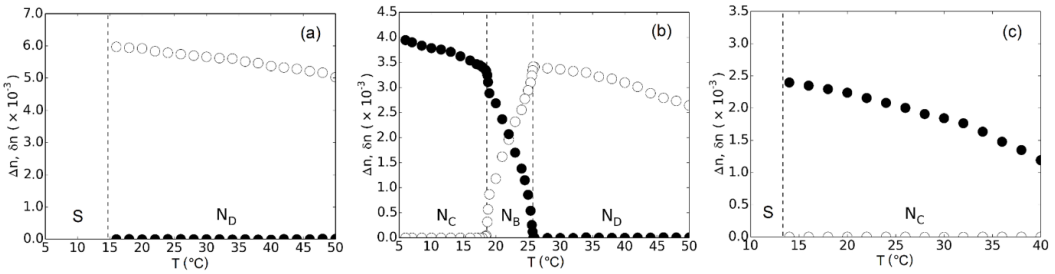

Figure 3.9 Variation of birefringence values of nematic phases with temperature for potassium alkanoate/Rb_2SO_4/DeOH/water mixtures obtained from our previous studies (Akpinar et al., 2018): (a) only a uniaxial N_D phase; (b) N_D, N_B and N_C phases depending on temperature; (c) only uniaxial N_C phase.

Temperature control is very important in the laser conoscopy system. For this purpose, a temperature controller (Lakeshore 335) and Pt102 sensor with 0.001°C sensitivity was used. To distribute the temperature homogeneously, a circulating water bath (Polyscience AD07R) with an accuracy of 0.01°C was used. The strength of the magnetic field in the system was checked with a Gaussmeter (Lakeshore, Model 455) during the measurements.

In general, a crystalline-like phase was observed at temperatures lower than 12°C, and isotropic (I) or two-phase regions (2P: isotropic + nematic) were observed at temperatures above 30°C, similar to dodecyltrimethylammonium bromide (DTMABr) surfactant system (74). Because such phases are not subjected to this thesis, they were not investigated in detail. Thus, the optimum working temperature range for laser conoscopy and polarized optical microscopy investigations of the nematic phases was determined as 12-30°C. The birefringence values (δn and Δn) as a function of temperature for the mixtures, which exhibited nematic phases (Tables 3.1 and 3.2), are given in Tables 3.3-3.20.

Table 3.3 Birefringence values of the s0 mixture (Table 3.1) depending on temperature.

T/°C	$\delta n/10^{-3}$	$\Delta n/10^{-3}$	T/°C	$\delta n/10^{-3}$	$\Delta n/10^{-3}$
29.25	1.82	0	20.30	1.37	0.94
28.25	1.92	0.00	20.10	1.06	1.17
27.50	1.99	0.00	19.90	0.87	1.40
27.00	2.02	0.00	19.70	0.72	1.62
26.50	2.05	0.00	19.50	0.57	1.87
26.00	2.09	0.00	19.30	0.43	2.11
25.50	2.12	0.00	19.10	0.17	2.31
25.00	2.15	0.00	19.00	0.00	2.46
24.50	2.17	0.00	18.90	0.00	2.58
24.00	2.20	0.00	18.70	0.00	2.66
23.50	2.25	0.00	18.40	0.00	2.70
23.00	2.28	0.00	18.00	0.00	2.77
22.50	2.32	0.00	17.50	0.00	2.81
22.00	2.33	0.00	17.00	0.00	2.86
21.50	2.35	0.00	16.50	0.00	2.92
21.30	2.36	0.00	16.00	0.00	2.98
21.10	2.36	0.01	15.50	0.00	3.03
21.00	2.23	0.07	14.75	0.00	3.06
20.90	2.08	0.17	14.00	0.00	3.11
20.70	1.95	0.38	13.00	0.00	3.17
20.50	1.62	0.70			

Table 3.4 Birefringence values of the s1 mixture (Table 3.1) depending on temperature.

T/°C	$\Delta n/10^{-3}$	T/°C	$\Delta n/10^{-3}$	T/°C	$\Delta n/10^{-3}$
22.00	0.00	19.00	0.53	16.90	2.24
21.50	0.00	18.80	0.63	16.80	2.26
21.00	0.00	18.60	0.71	16.60	2.31
20.50	0.00	18.40	0.81	16.30	2.35
20.10	0.00	18.20	0.92	16.00	2.40
19.90	0.00	18.00	1.04	15.50	2.45
19.80	0.00	17.80	1.19	15.00	2.50
19.70	0.08	17.60	1.36	14.50	2.55
19.60	0.18	17.40	1.59	14.00	2.62
19.40	0.32	17.20	1.78		
19.20	0.44	17.00	1.99		

Table 3.5 Birefringence values of the s2 mixture (Table 3.1) depending on temperature.

T/°C	$\Delta n/10^{-3}$	T/°C	$\Delta n/10^{-3}$	T/°C	$\Delta n/10^{-3}$
22.00	0.00	16.80	0.19	13.90	1.37
21.00	0.00	16.60	0.38	13.60	1.60
20.00	0.00	16.30	0.51	13.50	1.79
19.00	0.00	16.00	0.64	13.40	1.98
18.50	0.00	15.70	0.72	13.30	1.98
18.00	0.00	15.40	0.80	13.10	2.01
17.50	0.00	15.10	0.85	12.70	2.06
17.20	0.00	14.80	0.94	12.40	2.10
17.00	0.00	14.50	1.04	12.00	2.16
16.90	0.06	14.20	1.19		

Table 3.6 Birefringence values of the s3 mixture (Table 3.1) depending on temperature.

T/°C	$\delta n/10^{-3}$	$\Delta n/10^{-3}$	T/°C	$\delta n/10^{-3}$	$\Delta n/10^{-3}$
30.00	2.44	0.00	15.50	3.19	0.00
28.25	2.61	0.00	15.20	3.20	0.00
26.50	2.69	0.00	15.00	3.20	0.00
25.00	2.76	0.00	14.90	3.19	0.02
23.50	2.84	0.00	14.80	3.00	0.14
22.25	2.90	0.00	14.60	2.90	0.26
21.00	2.97	0.00	14.40	2.71	0.40
20.00	3.01	0.00	14.10	2.43	0.63
19.00	3.06	0.00	13.80	2.21	0.93
18.25	3.08	0.00	13.40	2.03	1.33
17.50	3.11	0.00	13.00	1.93	1.56
17.00	3.13	0.00	12.70	1.78	1.82
16.50	3.16	0.00	12.40	1.60	2.01
16.00	3.17	0.00	12.10	1.45	2.19
15.70	3.18	0.00			

Table 3.7 Birefringence values of the s4 mixture (Table 3.1) depending on temperature.

T/°C	δn/10^{-3}	Δn/10^{-3}	T/°C	δn/10^{-3}	Δn/10^{-3}
30.00	2.58	0.00	15.50	3.33	0.00
28.00	2.81	0.00	15.00	3.35	0.00
26.50	2.90	0.00	14.50	3.37	0.00
25.00	2.97	0.00	14.00	3.39	0.00
23.75	3.01	0.00	13.70	3.42	0.00
22.50	3.06	0.00	13.50	3.43	0.00
21.50	3.08	0.00	13.40	3.39	0.04
20.50	3.12	0.00	13.30	3.12	0.18
19.50	3.16	0.00	13.20	2.86	0.48
18.50	3.19	0.00	13.00	2.61	0.77
17.75	3.21	0.00	12.80	2.44	1.22
17.00	3.25	0.00	12.60	2.25	1.50
16.50	3.28	0.00	12.40	2.02	1.78
16.00	3.30	0.00			

Table 3.8 Birefringence values of the s5 mixture (Table 3.1) depending on temperature.

T/°C	δn/10^{-3}	Δn/10^{-3}	T/°C	δn/10^{-3}	Δn/10^{-3}
33.00	2.00	0.00	21.00	3.42	0.00
31.50	2.68	0.00	19.50	3.49	0.00
30.00	2.96	0.00	18.00	3.52	0.00
28.50	3.11	0.00	16.50	3.54	0.00
27.00	3.21	0.00	15.00	3.55	0.00
25.50	3.27	0.00	13.50	3.58	0.00
24.00	3.35	0.00	12.00	3.62	0.00
22.50	3.40	0.00			

Table 3.9 Birefringence values of the s6 mixture (Table 3.1) depending on temperature.

T/°C	$\delta n/10^{-3}$	$\Delta n/10^{-3}$	T/°C	$\delta n/10^{-3}$	$\Delta n/10^{-3}$
29.00	3.10	0.00	20.00	3.60	0.00
27.50	3.24	0.00	18.50	3.65	0.00
26.00	3.32	0.00	17.00	3.73	0.00
24.50	3.39	0.00	15.50	3.79	0.00
23.00	3.47	0.00	14.00	3.86	0.00
21.50	3.53	0.00	12.50	3.96	0.00

Table 3.10 Birefringence values of the s7 mixture (Table 3.1) depending on temperature.

T/°C	$\delta n/10^{-3}$	$\Delta n/10^{-3}$	T/°C	$\delta n/10^{-3}$	$\Delta n/10^{-3}$
29.00	3.15	0.00	20.00	3.94	0.00
27.50	3.38	0.00	18.50	4.03	0.00
26.00	3.53	0.00	17.00	4.10	0.00
24.50	3.64	0.00	15.50	4.17	0.00
23.00	3.76	0.00	14.00	4.25	0.00
21.50	3.85	0.00	12.50	4.33	0.00

Table 3.11 Birefringence values of the s8 mixture (Table 3.1) depending on temperature.

T/°C	**$\delta n/10^{-3}$**	**$\Delta n/10^{-3}$**	**T/°C**	**$\delta n/10^{-3}$**	**$\Delta n/10^{-3}$**
30.00	3.03	0.00	19.50	3.50	0.00
28.50	3.13	0.00	18.00	3.55	0.00
27.00	3.17	0.00	16.50	3.60	0.00
25.50	3.24	0.00	15.00	3.67	0.00
24.00	3.33	0.00	13.50	3.75	0.00
22.50	3.39	0.00	12.00	3.81	0.00
21.00	3.43	0.00			

Table 3.12 Birefringence values of the s17 mixture (Table 3.2) depending on temperature.

T/°C	$\delta n/10^{-3}$	$\Delta n/10^{-3}$	T/°C	$\delta n/10^{-3}$	$\Delta n/10^{-3}$
29.75	1.44	0.00	21.20	0.72	1.36
28.50	1.58	0.00	21.10	0.58	1.55
27.50	1.67	0.00	21.00	0.29	1.79
26.50	1.76	0.00	20.90	0.15	2.00
25.50	1.84	0.00	20.80	0.08	2.08
25.00	1.87	0.00	20.60	0.00	2.12
24.50	1.91	0.00	20.30	0.00	2.17
24.00	1.93	0.00	20.00	0.00	2.24
23.50	1.94	0.00	19.50	0.00	2.34
23.00	1.96	0.00	19.00	0.00	2.44
22.50	1.98	0.00	18.50	0.00	2.57
22.20	1.98	0.00	18.00	0.00	2.67
22.00	1.99	0.01	17.50	0.00	2.76
21.90	1.988	0.06	17.00	0.00	2.86
21.80	1.93	0.19	16.00	0.00	3.02
21.70	1.74	0.41	15.00	0.00	3.20
21.60	1.57	0.58	14.00	0.00	3.36
21.50	1.35	0.77	13.00	0.00	3.58
21.40	1.09	1.00	12.00	0.00	3.71
21.30	0.88	1.20			

Table 3.13 Birefringence values of the s18 mixture (Table 3.2) depending on temperature.

T/°C	$\delta n/10^{-3}$	$\Delta n/10^{-3}$	T/°C	$\delta n/10^{-3}$	$\Delta n/10^{-3}$
30.00	1.01	0.00	21.80	0.66	1.13
29.00	1.14	0.00	21.70	0.48	1.34
28.00	1.28	0.00	21.60	0.25	1.51
27.25	1.36	0.00	21.50	0.14	1.70
26.50	1.45	0.00	21.40	0.04	1.85
26.00	1.51	0.00	21.30	0.00	1.97
25.50	1.55	0.00	21.10	0.00	2.17
25.00	1.59	0.00	20.80	0.00	2.48
24.50	1.63	0.00	20.40	0.00	2.66
24.00	1.66	0.00	20.00	0.00	2.86
23.50	1.70	0.00	19.50	0.00	3.00
23.00	1.73	0.00	19.00	0.00	3.16
22.70	1.75	0.00	18.50	0.00	3.29
22.50	1.75	0.00	18.00	0.00	3.41
22.40	1.70	0.04	17.50	0.00	3.54
22.30	1.56	0.12	17.00	0.00	3.67
22.25	1.39	0.30	16.25	0.00	3.84
22.20	1.25	0.48	15.50	0.00	4.01
22.10	1.11	0.64	14.50	0.00	4.12
22.00	0.98	0.82	13.25	0.00	4.32
21.90	0.78	1.00			

Table 3.14 Birefringence values of the s19 mixture (Table 3.2) depending on temperature.

T/°C	$\delta n/10^{-3}$	$\Delta n/10^{-3}$	T/°C	$\delta n/10^{-3}$	$\Delta n/10^{-3}$
29.00	0.81	0.00	22.65	0.50	1.15
28.25	0.97	0.00	22.60	0.37	1.32
27.50	1.12	0.00	22.55	0.25	1.42
27.00	1.20	0.00	22.50	0.22	1.49
26.50	1.27	0.00	22.45	0.00	1.68
26.00	1.32	0.00	22.30	0.00	1.87
25.50	1.37	0.00	22.10	0.00	2.04
25.00	1.41	0.00	21.80	0.00	2.30
24.50	1.44	0.00	21.50	0.00	2.49
24.00	1.47	0.00	21.00	0.00	2.59
23.60	1.49	0.00	20.50	0.00	2.78
23.30	1.50	0.00	20.00	0.00	2.93
23.10	1.50	0.01	19.25	0.00	3.13
23.00	1.34	0.06	18.50	0.00	3.30
22.95	1.21	0.27	17.50	0.00	3.45
22.90	1.09	0.47	16.50	0.00	3.72
22.85	0.93	0.69	15.50	0.00	3.98
22.80	0.82	0.82	14.50	0.00	4.25
22.75	0.65	0.97	13.00	0.00	4.42
22.70	0.56	1.06			

Table 3.15 Birefringence values of the s20 mixture (Table 3.2) depending on temperature.

T/°C	$\delta n/10^{-3}$	$\Delta n/10^{-3}$	T/°C	$\delta n/10^{-3}$	$\Delta n/10^{-3}$
27.00	0.78	0.00	23.20	0.00	1.28
26.50	0.91	0.00	23.10	0.00	1.38
26.00	1.02	0.00	22.90	0.00	1.50
25.50	1.08	0.00	22.50	0.00	1.67
25.00	1.15	0.00	22.00	0.00	1.83
24.50	1.20	0.00	21.50	0.00	2.02
24.10	1.23	0.00	21.00	0.00	2.19
23.80	1.25	0.00	20.50	0.00	2.34
23.70	1.24	0.00	19.75	0.00	2.58
23.60	1.19	0.07	19.00	0.00	2.77
23.55	1.12	0.14	18.00	0.00	2.99
23.50	1.01	0.33	17.00	0.00	3.22
23.45	0.79	0.49	16.00	0.00	3.40
23.40	0.62	0.72	14.75	0.00	3.63
23.35	0.53	0.88	13.50	0.00	3.85
23.30	0.35	0.99	12.00	0.00	4.01
23.25	0.12	1.13			

Table 3.16 Birefringence values of the s21 mixture (Table 3.2) depending on temperature.

T/°C	$\delta n/10^{-3}$	$\Delta n/10^{-3}$	T/°C	$\delta n/10^{-3}$	$\Delta n/10^{-3}$
25.50	0.74	0.00	23.50	0.00	1.44
25.00	0.83	0.00	23.00	0.00	1.53
24.60	0.88	0.00	22.50	0.00	1.68
24.40	0.91	0.00	22.00	0.00	1.80
24.30	0.92	0.00	21.00	0.00	1.97
24.20	0.92	0.01	20.00	0.00	2.15
24.10	0.90	0.06	18.75	0.00	2.42
24.05	0.78	0.54	17.50	0.00	2.72
24.00	0.03	1.15	16.00	0.00	3.09
23.95	0.00	1.19	14.50	0.00	3.35
23.80	0.00	1.28	13.00	0.00	3.61

Table 3.17 Birefringence values of the s22 mixture (Table 3.2) depending on temperature.

T/°C	$\delta n/10^{-3}$	$\Delta n/10^{-3}$	T/°C	$\delta n/10^{-3}$	$\Delta n/10^{-3}$
23.00	0.00	1.39	17.00	0.00	3.19
22.00	0.00	1.86	16.00	0.00	3.44
21.00	0.00	2.17	15.00	0.00	3.63
20.00	0.00	2.51	14.00	0.00	3.76
19.00	0.00	2.77	13.00	0.00	3.90
18.00	0.00	3.00			

Table 3.18 Birefringence values of the s23 mixture (Table 3.2) depending on temperature.

T/°C	$\delta n/10^{-3}$	$\Delta n/10^{-3}$	T/°C	$\delta n/10^{-3}$	$\Delta n/10^{-3}$
23.00	0.00	1.44	17.00	0.00	3.20
22.00	0.00	1.80	16.00	0.00	3.37
21.00	0.00	2.21	15.00	0.00	3.52
20.00	0.00	2.51	14.00	0.00	3.74
19.00	0.00	2.79	13.00	0.00	3.89
18.00	0.00	2.99	12.00	0.00	3.98

Table 3.19 Birefringence values of the s24 mixture (Table 3.2) depending on temperature.

T/°C	$\delta n/10^{-3}$	$\Delta n/10^{-3}$	T/°C	$\delta n/10^{-3}$	$\Delta n/10^{-3}$
21.00	0.00	1.39	16.00	0.00	3.09
20.00	0.00	1.90	15.00	0.00	3.27
19.00	0.00	2.32	14.00	0.00	3.40
18.00	0.00	2.64	13.00	0.00	3.60
17.00	0.00	2.87	12.00	0.00	3.67

Table 3.20 Birefringence values of the s25 mixture (Table 3.2) depending on temperature.

T/°C	$\delta n/10^{-3}$	$\Delta n/10^{-3}$	T/°C	$\delta n/10^{-3}$	$\Delta n/10^{-3}$
22.00	0.00	1.49	16.00	0.00	3.19
21.00	0.00	1.97	15.00	0.00	3.34
20.00	0.00	2.32	14.00	0.00	3.48
19.00	0.00	2.63	13.00	0.00	3.65
18.00	0.00	2.83	12.00	0.00	3.74
17.00	0.00	3.01			

3.3.4 Small-Angle X-Ray Scattering Measurements

The SAXS measurements were performed in a Xeuss 2.0 laboratory-based system (Xenocs, France), composed of mainly a Cu anode microfocus' X-ray source, followed by a FOX^{3D} X-ray mirror for monochromatization and collimation of the X-ray beam, and a pair of Xenocs scatterless slits for futher collimation. The monochromatic and collimated incident X-ray beam has a wavelength of 1.5419 Å and a square cross-section of 0.7 mm side in the sample position. The measurements were performed in transmission geometry. The two-dimensional X-ray scattering patterns were measured in a Pilatus 300K detector (Dectris, Switzerland). The sample-to-detector distance was chosen as 937 mm.

The samples were transferred into cylindrical Mark-tube capillaries of 1.5 mm diameter (Hilgenberg, Germany), and they were closed with UV-sensitive photopolymer to prevent sample evaporation. For the measurements, a capillary was placed in a temperature-controlled sample holder with precision of ± 0.2 °C. A sufficient homogeneous static magnetic field was generated by attaching rectangular bars of permanent NdFeB magnets (~1 kG) to the sidewalls of the sample holder.

From the 2D anisotropic scattering patterns, frame integrations were performed along the directions parallel and perpendicular to the magnetic field direction. The frame integrations of 2D SAXS were madeobtained in circular sectors of 20° around the vertical (VRT) and horizontal (HRZ) directions of the images, Figure 3.10. These operations resulted in curves of X-ray scattering intensity as a function of the momentum transfer modulus, $q=4\pi/\lambda \sin(\theta) q = (4\pi/\lambda) \sin\theta$, where 2θ is the scattering angle.

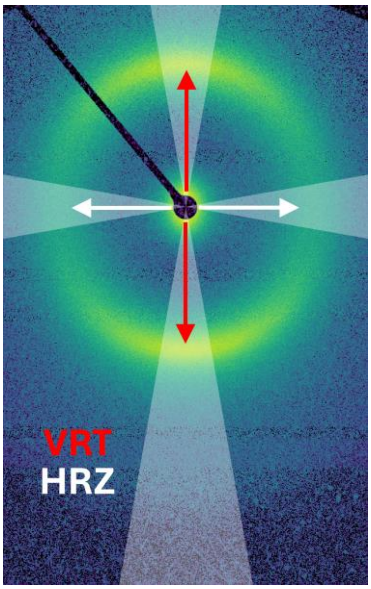

Figure 3.10 Frame integrations of a 2D anisotropic SAXS patterns in circular sectors of 20° around the vertical (VRT) and horizontal (HRZ) directions of the images.

4. RESULTS AND DISCUSSION

The interactions between ionic species (head groups of surfactants, counterions, electrolyte ions, etc.) play a crucial role in micellar solutions. It is well known from the literature that those interactions modify the packing of the surfactant molecules in the micelles, leading to changes in the micelle surface curvature and the micellar shape anisotropy. Experimental results showed that the modifications in terms of the ionic interactions at micelle surfaces may control the stabilization of different lyotropic nematic phases and the temperature range of the N_B phase in the partial phase diagrams. Furthermore, highly ordered lyotropic structures such as lamellar and hexagonal ones are also obtained depending on the strength of those interactions. In a recent study, we showed that the degrees of kosmotropic and chaotropic properties of the surfactant head groups and the counterions or ions of the electrolytes present in the lyotropic mixtures have to be considered to obtain uniaxial and biaxial nematic phases. In addition, the relation between the average area per surfactant head group and the formation of possible types of lyotropic structures was reported in a few studies in the literature. However, when those studies were performed, the existence of the biaxial nematic phases was not found experimentally. Another deficiency in these studies is that the results obtained from different lyotropic systems were compared. In the present study, we aim to investigate the relation between the formation of the different lyotropic structures (lamellar, hexagonal, and nematic) in the same system, which gives a biaxial nematic phase, and the experimental data obtained are presented in the following part of the thesis.

4.1 Determination of Textures of Lyotropic Mixtures: Polarized Optical Microscopy

Depending on the mixture compositions (Table 3.1 and Table 3.2), different lyotropic phases (lamellar, hexagonal, and nematic) were obtained from single and binary surfactant systems. The textures of those phases were analyzed under the polarized optical microscope. Nematic phases are characterized by their characteristic “schlieren” textures. Lamellar and hexagonal phase textures are generally characterized as "oily streak" and "fan-shaped", respectively. Figure 4.1

shows the phase textures characterized under POM for mixtures s0, s16 and s32 which give three types of nematic phases depending on temperature, only lamellar phase, and only hexagonal phase, respectively. Similar phase textures were observed for the phases of other samples. The observed lyotropic phase types for DDMEABr/DDMABr and DDMEABr/DTEABr single and binary surfactant mixtures are given in Tables 4.1 and 4.2. The nematic-nematic phase transitions were obtained from laser conoscopy measurements. The lyotropic phase types were also confirmed by Small-Angle X-ray Scattering results (see part 4.3).

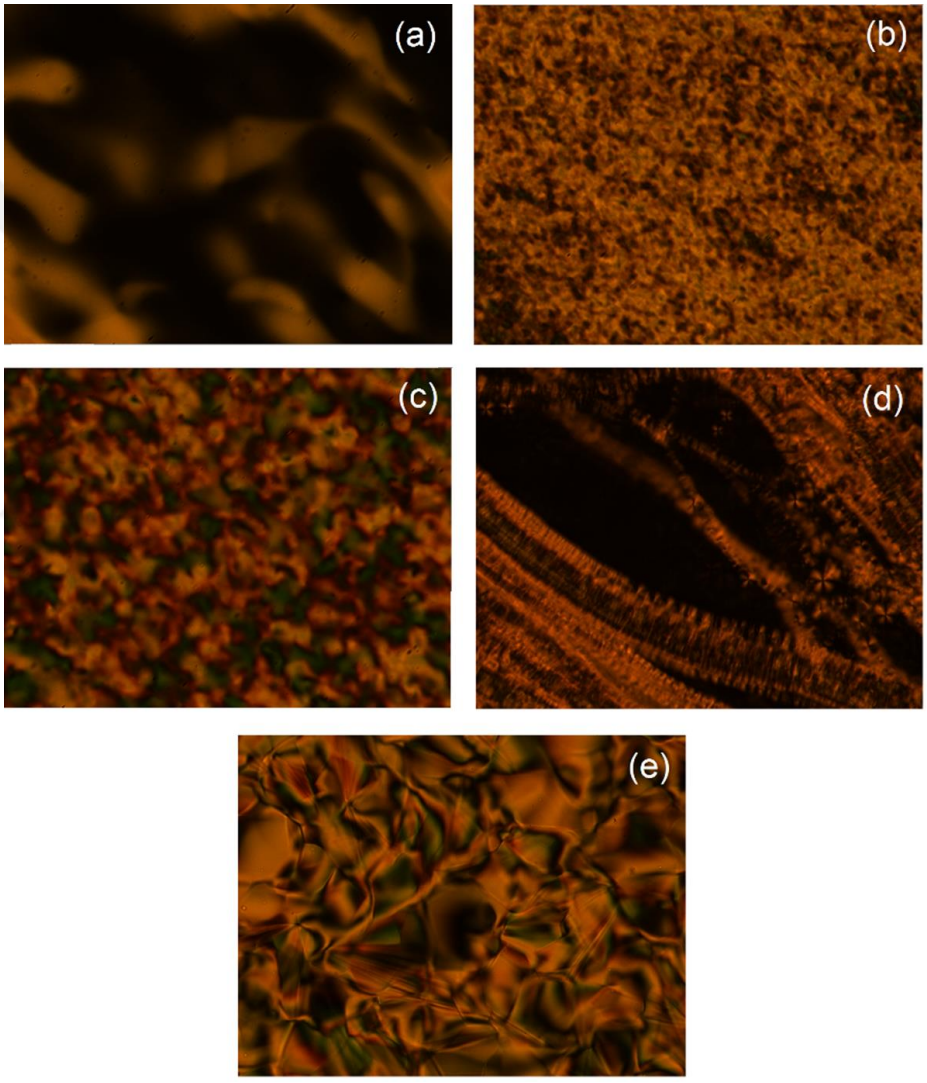

Figure 4.1. Lyotropic liquid crystal phase textures observed under a polarized optical microscope: (a) N_D at 22.0°C, (b) N_B at 20.0°C, and (c) N_C at 18.0°C for s0 mixture containing only DDMEABr; (d) L_α phase at 25.0°C for s16 mixture containing only DDMABr; (e) H phase at 25.0°C for s32 mixture containing only DTEABr. Objective: 10x. Sample thickness: 0.400 mm.

Table 4.1. Lyotropic phase types, nematic-nematic phase transition temperatures and the range of the biaxial nematic phase region - ΔT_{N_B} for DDMEABr/SSY/ DDeOH/water single surfactant mixture and DDMEABr/DDMABr/Sunset Yellow/DDeOH/water binary surfactant mixtures. Nematic-nematic phase transition temperatures and ΔT_{N_B} were determined from laser conoscopy. The lyotropic phase types were characterized by polarized optical microscopy and confirmed by the SAXS investigations. L_α: lamellar phase.

Mixture	**Lyotropic phase types and nematic-nematic phase transition temperatures**	ΔT_{N_B}/°C
s0	$N_D \xrightarrow{21.0℃} N_B \xrightarrow{19.0℃} N_C$	2.0
s1	$N_D \xrightarrow{19.4℃} N_B \xrightarrow{16.8℃} N_C$	2.6
s2	$N_D \xrightarrow{16.7℃} N_B \xrightarrow{13.5℃} N_C$	3.2
s3	$N_D \xrightarrow{14.8℃} N_B$	---
s4	$N_D \xrightarrow{13.1℃} N_B$	---
s5	N_D	---
s6	N_D	---
s7	N_D	---
s8	N_D	---
s9	N_D	---
s10	L_α	---
s11	L_α	---
s12	L_α	---
s13	L_α	---
s14	L_α	---
s15	L_α	---
s16	L_α	---

Table 4.2. Lyotropic phase types, nematic-nematic phase transition temperatures and the range of the biaxial nematic phase region - ΔT_{N_B} for DDMEABr/SSY/ DDeOH/water single surfactant mixture and DDMEABr/DDMABr/Sunset Yellow/DDeOH/water binary surfactant mixtures. H: hexagonal phase.

Sample	**Lyotropic phase types and nematic-nematic phase transition temperatures**	ΔT_{N_B}/℃
s0	$N_D \xrightarrow{21.0℃} N_B \xrightarrow{19.0℃} N_C$	2.0
s17	$N_D \xrightarrow{22.0℃} N_B \xrightarrow{20.6℃} N_C$	1.4
s18	$N_D \xrightarrow{22.3℃} N_B \xrightarrow{21.4℃} N_C$	0.9
s19	$N_D \xrightarrow{23.0℃} N_B \xrightarrow{22.4℃} N_C$	0.6
s20	$N_D \xrightarrow{23.6℃} N_B \xrightarrow{23.2℃} N_C$	0.4
s21	$N_D \xrightarrow{24.1℃} N_B \xrightarrow{24.0℃} N_C$	0.1
s22	N_C	---
s23	N_C	---
s24	N_C	---
s25	N_C	---
s26	*H*	---
s27	*H*	---
s28	*H*	---
s29	*H*	---
s30	*H*	---
s31	*H*	---
s32	*H*	---

4.2 Determination of Nematic-Nematic Phase Transitions and Birefringences with Laser Conoscopy Measurements

As we mentioned before, lyotropic nematic phases are defined by three refractive indices and two birefringences: $\Delta n = n_2 - n_1$ and $\delta n = n_3 - n_2$. In the case of the lyotropic discotic nematic phase (N_D), $n_3 > n_2 = n_1$, which results in $\Delta n = 0$ and $\delta n > 0$. In the case of the lyotropic calamitic nematic phase (N_C), $n_3 = n_2 > n_1$, hence $\Delta n > 0$ and $\delta n = 0$. In lyotropic biaxial nematic phases (N_B), $n_1 \neq n_2 \neq n_3$. If $n_3 - n_2 > n_2 - n_1$ ($n_3 - n_2 < n_2 - n_1$), the N_B phase is defined with positive (negative) birefringence. An important property is observed in the birefringence-temperature phase diagrams obtained from laser conoscopy: the existence of a crossover point at which both birefringences are equal ($\Delta n = \delta n$). After reaching this point, the macroscopic birefringence value of the biaxial nematic phase changes sign (from negative to positive or from positive to negative). We observed this situation in the laser conoscopy results of the DDMABr/DDMEABr and DDMEABr/DTEABr binary surfactant systems, Figure 4.3-4.4. In other words, in all birefringence-temperature phase diagrams, $\Delta n = 0$ and $\delta n > 0$ for N_D phases, and $\Delta n > 0$ and $\delta n = 0$ for N_C phases; it can be seen from the laser conoscopy results that when entering the biaxial nematic phase from the N_D phase by changing the temperature, $\delta n > \Delta n$ up to the crossover point and $\delta n < \Delta n$ from the crossover point to the N_C phase, which is in a good agreement with the literature (73,75).

Considering the birefringence values given in Tables 3.3-3.20, the birefringences-temperature partial phase diagrams for the nematic phases of DDMABr/DDMEABr and DDMEABr/DTEABr binary surfactant systems are graphically shown in Figures 4.3 and 4.4. The birefringences for mixtures of s1 and s2 could not be determined in a part of the biaxial nematic phase region after the crossover point. It was identified as "anomalous behavior" in the literature (74), and it is due to the decrease in micellar shape anisotropy, which results in the loss of the orientation of the nematic phase director in the magnetic field. So, although N_D-N_B transitions could be determined accurately from the laser conoscopy, N_B-N_C transitions could not. For samples s1 and s2, nematic-nematic phase transition temperatures were determined by using the Senarmont compensator under POM (Figure 4.2). With this technique, only Δn values can be

determined due to the configuration of the microscope. However, these values are sufficient to determine the nematic-nematic phase transition temperatures.

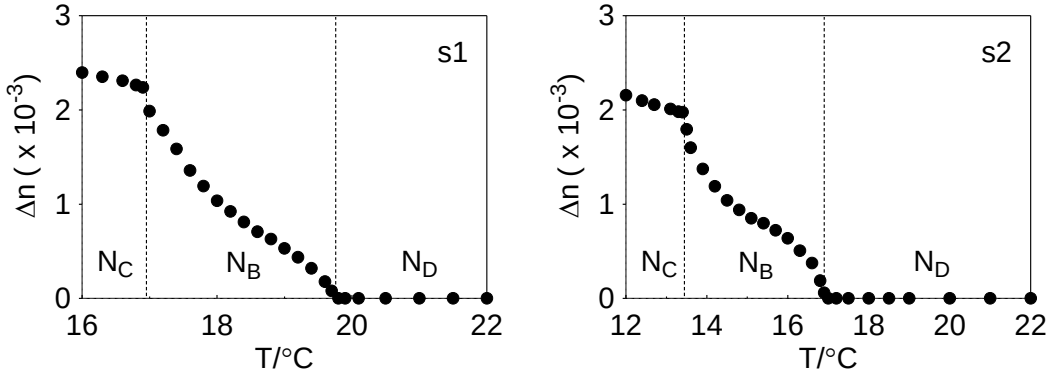

Figure 4.2. Temperature dependence of the birefringence Δn for the nematic phases of s1 and s2 mixtures (Table 3.1) obtained from POM measurements by using the Senarmont compensator.

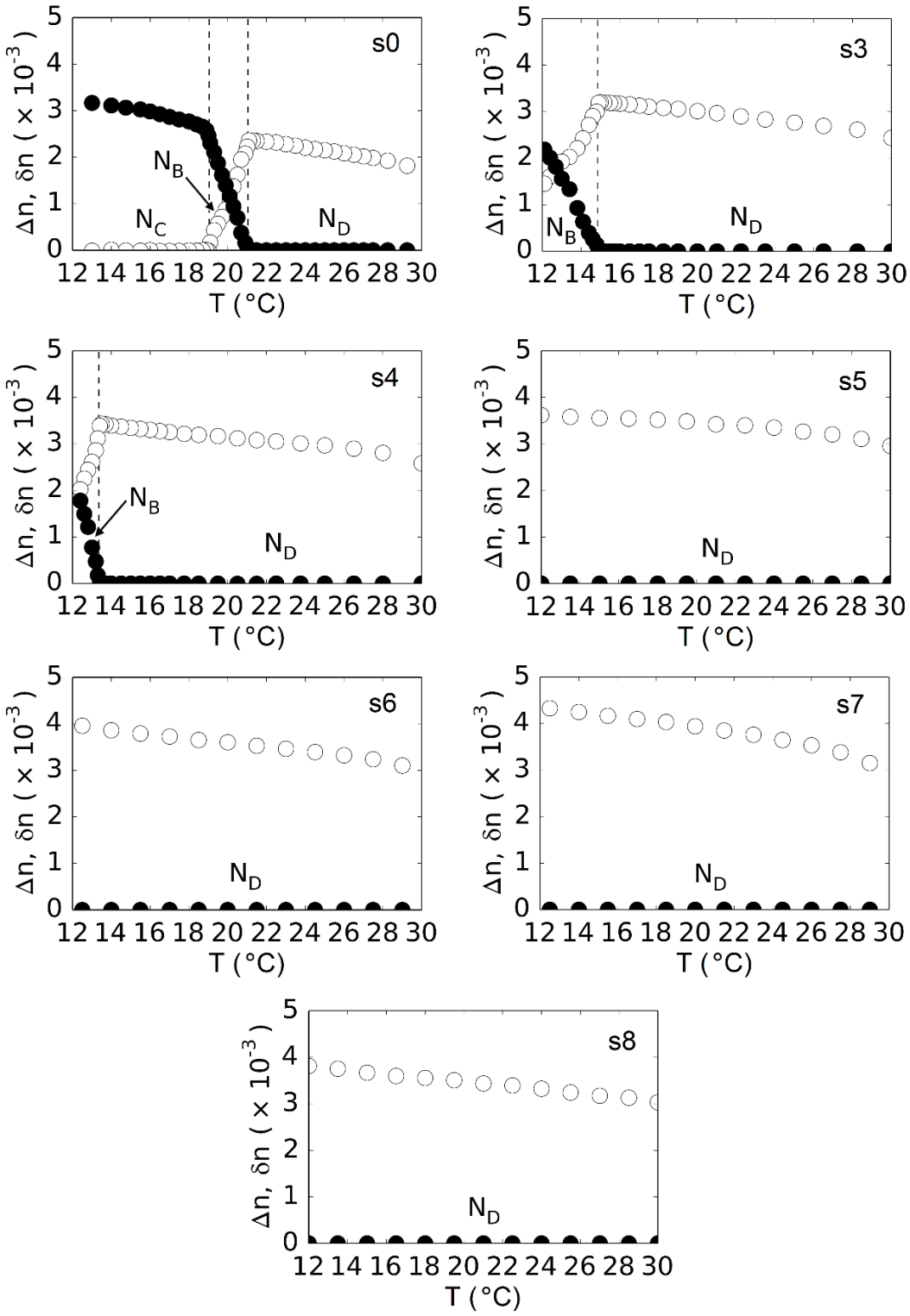

Figure 4.3. The birefringences-temperature partial phase diagrams determined from laser conoscopy for the nematic phases of DDMEABr/DDMABr mixtures (Table 3.1). Δn (●); δn (○).

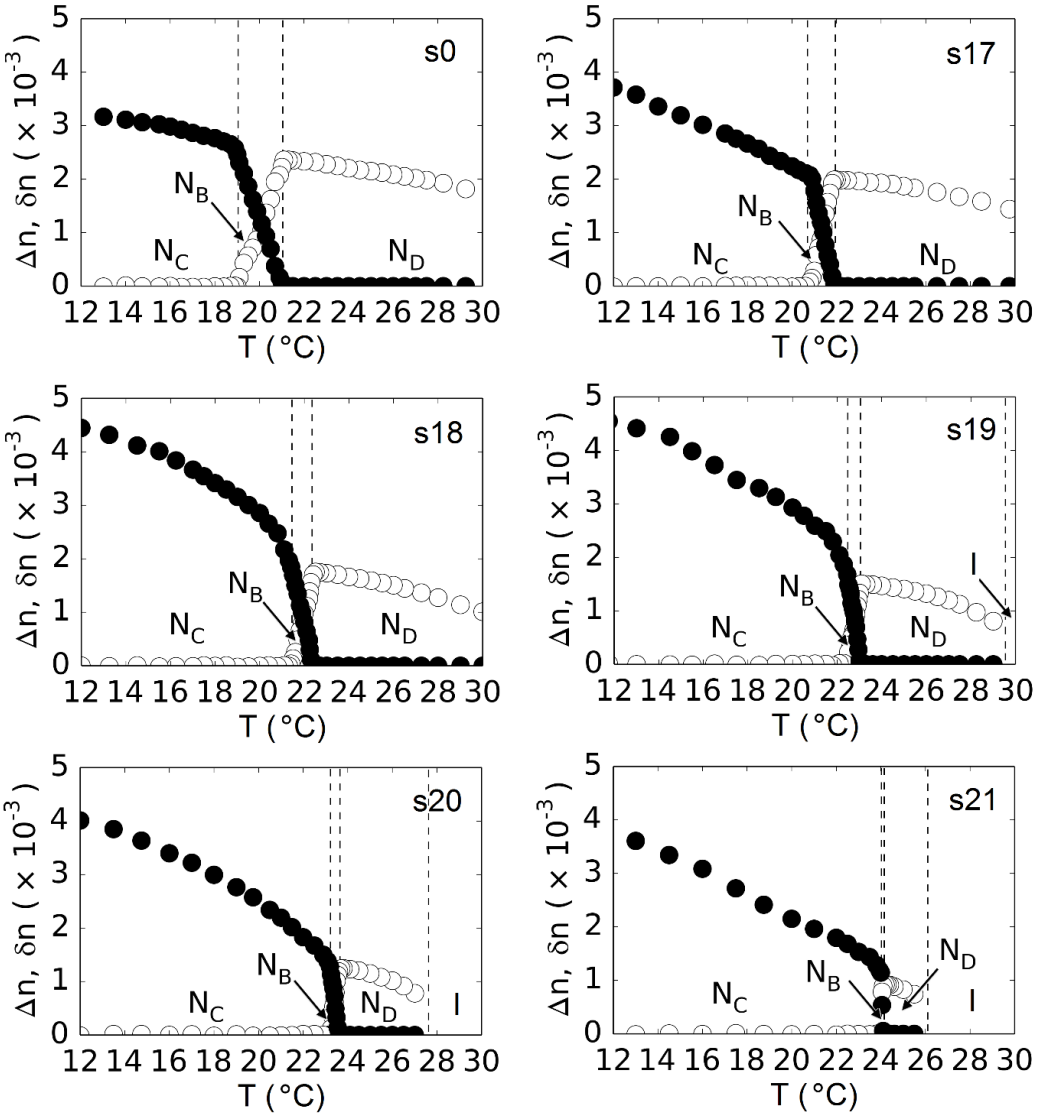

Figure 4.4a. The birefringences-temperature partial phase diagrams determined from laser conoscopy for the nematic phases of DDMEABr/DTEABr mixtures (Table 3.2). Δn (●); δn (○). I: Isotropic phase.

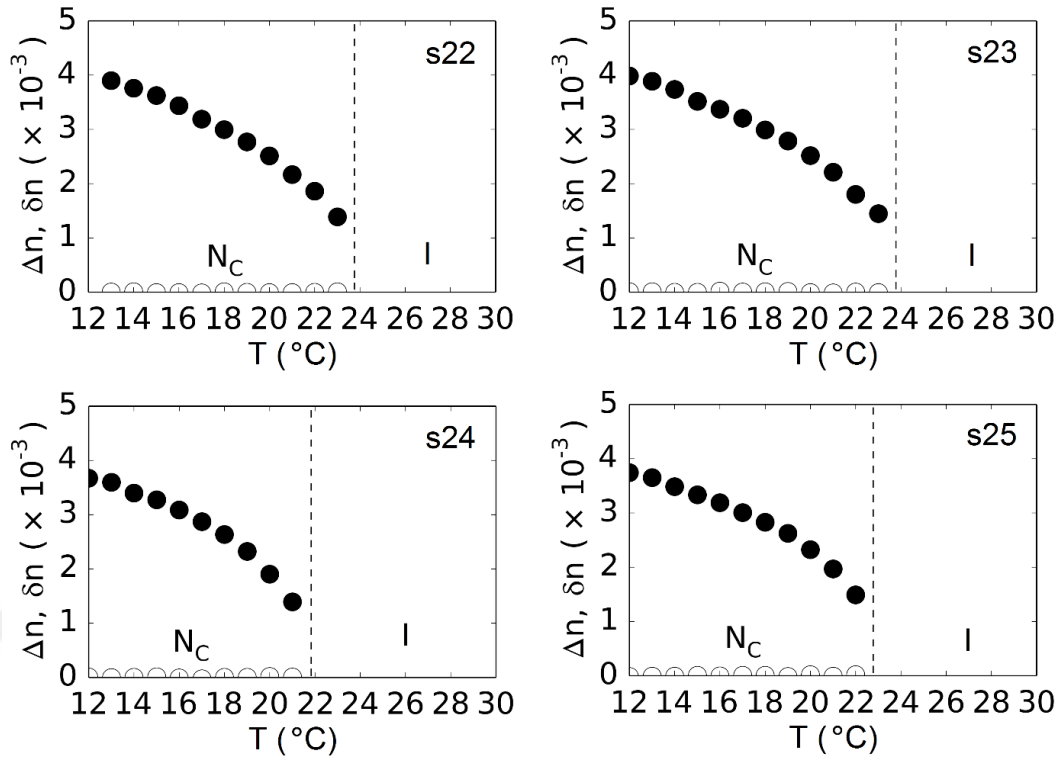

Figure 4.4b. The birefringences-temperature partial phase diagrams determined from laser conoscopy for the nematic phases of DDMEABr/DTEABr mixtures (Table 3.2). Δn (●) and δn (○). I: Isotropic phase.

4.3 Temperature-Concentration Phase Diagrams

Temperature-concentration partial phase diagrams for DDMEABr/ DDMABr and DDMEABr/DTEABr systems were constructed in the temperature range of 12-30°C by combining the POM investigations with the laser conoscopy results. Their phase diagrams are given in Figure 4.5 and Figure 4.6, respectively.

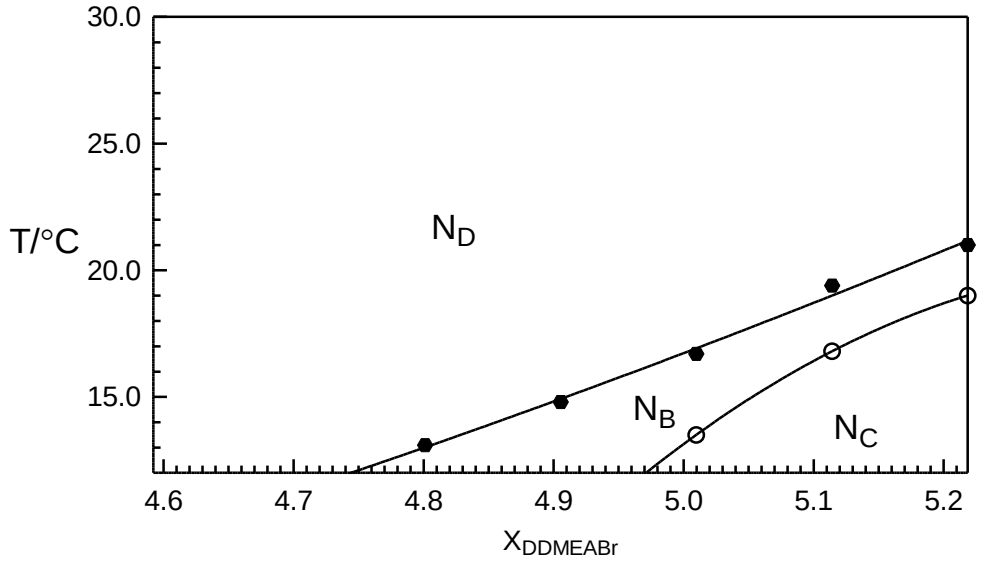

Figure 4.5 Partial phase diagram of the DDMEABr/DDMABr system. $X_{DDMEABr}$ is the percent mole fraction of DDMEABr at constant total surfactant concentration ($X_{DDMEABr}$ + X_{DDMABr}) in the mixtures. ● N_D-N_B phase transition temperatures; ○ N_B-N_C phase transition temperatures.

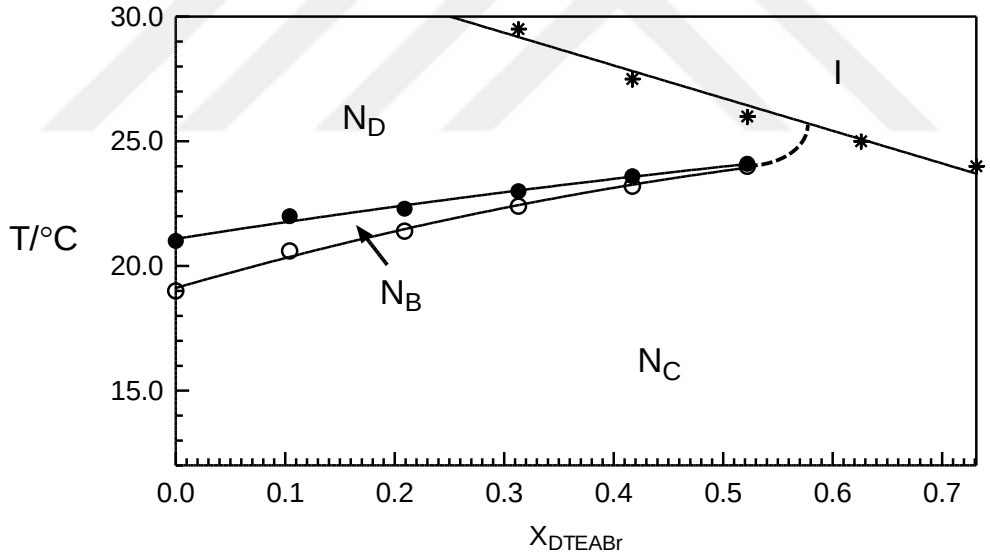

Figure 4.6 Partial phase diagram of the DDMEABr/DTEABr system. X_{DTEABr} is the percent mole fraction of DTEABr at constant total surfactant concentration ($X_{DDMEABr}$ + X_{DTEABr}) in the mixtures. ● N_D-N_B phase transition temperatures; ○ N_B-N_C phase transition temperatures.

For dodecylalkylammonium bromides, as the number of the $–CH_2$ group increases the head group size enlarges (76). The increase in the order of the head

group size or the area per surfactant head group on the micelle surfaces is DTEABr > DDMEABr > DDMABr. So, as it is expected, the average area per surfactant head group (a_0) on the micelle surfaces should increase (decrease) with the replacement of some part of DDMEABr with DTEABr (DDMABr) in the DDMEABr/DTEABr (DDMEABr/DDMABr) binary surfactant systems. Experimental results indicated that there is a relation between the formation of different nematic phases and the a_0. Furthermore, while the largest (lowest) a_0 value is obtained for the N_C (N_D) phase, the surfactant head groups have moderate level a_0 values in the N_B phase. This can be seen from the partial phase diagrams: at a constant total surfactant concentration, the N_C phase region expands with increasing surfactant head group size in the DDMEABr/DTEABr system, while the N_D phase region expands with decreasing surfactant head group size in the DDMEABr/DDMABr system. By combining the partial phase diagrams given in Figure 4.5 and Figure 4.6, the effect of head group size dependence of nematic phase formations in our binary surfactant systems can be more understandable, except that in this case the phase transition temperatures are plotted against the average number of $–CH_2$ groups per surfactant head group (n_{avg}) (Figure 4.7) (20). In this way, the effect of head group size on the biaxial nematic phase region can be seen in more detail. The n_{avg} values are calculated from the following equation (Equation 4.1):

$$n_{avg} = \frac{X_{DDMEABr}}{X_{total}} n_{DDMEABr} + \frac{X_{DDMABr}}{X_{total}} n_{DDMABr} + \frac{X_{DTEABr}}{X_{total}} n_{DTEABr} \qquad (4.1)$$

$X_{DDMEABr}$, X_{DDMABr} and X_{DTEABr} are the mole fractions of all three surfactants in the mixtures; $n_{DDMEABr}$, n_{DDMABr} and n_{DTEABr} are the number of $–CH_2$ groups in the head groups of the surfactants (2, 4 and 6 for DDMABr, DDMEABr and DTEABr, respectively); X_{total} is the total mole fraction of surfactants in the mixtures. The n_{avg} values are given in Table 4.3. Furthermore, the change of ΔT_{N_B} with n_{avg} is shown in Figure 4.8. The partial phase diagram was constructed according to the dependence of the uniaxial-biaxial nematic phase transitions on n_{avg}, obtained from polarized optical microscopy and laser conoscopy measurements of the mixtures (Figure 4.7). A similar partial phase diagram was reported for dodecyldimethylammonium bromide/dodecyltrimethylammonium bromide (DTMABr) and

DDMEABr/DTMABr binary surfactant systems, remaining in the nematic phases but not investigating lamellar and hexagonal phases (64).

Table 4.3 Surfactant percent mole fractions ($X_{DDMEABr}/_{DDMABr}/_{DTEABr}$) for mixtures which give three types of nematic phases depending on temperature from DDMEABr/DDMABr/Sunset Yellow/DDeOH/water and DDMEABr/DTEABr/ Sunset Yellow/DDeOH/water binary surfactant systems. ΔT_{N_B} is temperature range of the biaxial nematic phase region; average number of $–CH_2$ groups per surfactant on micellar surfaces (n_{avg}); discotic nematic-biaxial nematic (N_D-N_B) and biaxial nematic-calamitic nematic (N_B-N_C) phase transition temperatures.

Mixture	$\mathbf{X_{DDMEABr}}$	$\mathbf{X_{DDMABr}}$	$\mathbf{X_{DTEABr}}$	$\mathbf{n_{avg}}$	N_D-N_B/°C	N_B-N_C/°C	ΔT_{N_B}/°C
s4	4.801	0.417	-----	3.84	13.1	-----	-----
s3	4.905	0.313	-----	3.88	14.8	-----	-----
s2	5.010	0.209	-----	3.92	16.7	13.5	3.2
s1	5.114	0.104	-----	3.96	19.4	16.8	2.6
s0	5.218	0.000	-----	4.00	21.0	19.0	2.0
s17	5.114	-----	0.104	4.04	22.0	20.6	1.4
s18	5.010	-----	0.209	4.08	22.3	21.4	0.9
s19	4.905	-----	0.313	4.12	23.0	22.4	0.6
s20	4.801	-----	0.417	4.16	23.6	23.2	0.4
s21	4.697	-----	0.522	4.20	24.1	24.0	0.1

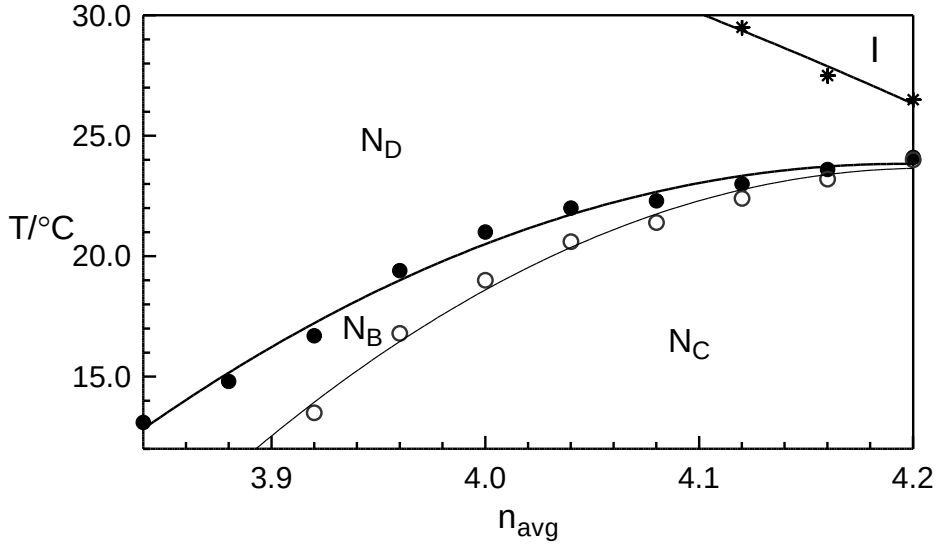

Figure 4.7 Partial phase diagram considering the n_{avg} values for mixtures of DDMEABr/DDMABr/Sunset Yellow/DDeOH/water and DDMEABr/DTEABr/ Sunset Yellow/DDeOH/water binary surfactant systems. This phase diagram was obtained by combining the partial phase diagrams shown in the Figures 4.5 and 4.6.

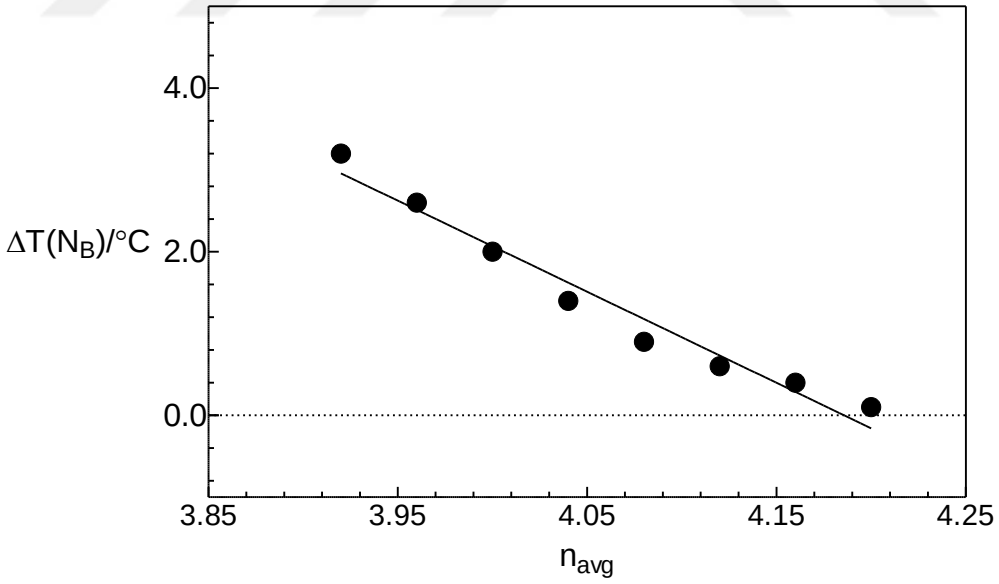

Figure 4.8 Variation of temperature range of the biaxial nematic phase region ΔT_{N_B} with the average number of surfactant head groups n_{avg} in the partial phase diagrams for the mixtures given in Table 4.3.

According to the IBM model of the lyotropic nematic phases (31) the driving force for the formation of different nematic phases is the orientational fluctuations of the orthorhombic or plank-like micelles (see the Introduction part of the thesis). As the amount of DDMABr is increased in the binary surfactant system, (from s1 to s4), the n_{avg} values decrease and the N_D-N_B and N_B-N_C phase transition temperatures shift to lower values. In addition, the temperature ranges of the N_D and N_B phase regions increase in the partial phase diagrams. The opposite situation was observed for DDMEABr/DTEABr system with the increase in the average surfactant head group size (from mixture s17 to s21): by increasing the amount of DTEABr in the mixtures, (a) N_D-N_B and N_B-N_C phase transition temperature shifts to higher values and (b) the N_C phase region increases by expensing the N_D/N_B phase regions in the partial phase diagrams. These results indicate that the decrease (increase) in the average area per surfactant head group on the micelle surfaces favors the orientational fluctuations around the symmetry axis perpendicular (parallel) to the largest micelle surfaces (the longest micelle dimension) to form the N_D (N_C) phase with the small amplitude orientational fluctuations around three symmetry axes in the N_B phase. Further increase in the amount of DDMABr (DTEABr) favors the formation of first only the N_D (N_C) phase and then the lamellar (hexagonal) phase, which was confirmed by the POM (Part 4.1) and SAXS (Part 4.3) results.

In the literature, there are some studies to show the relationship between the formation of the lyotropic structures and surfactant head group size (65,66). However, in those studies, the existence of the N_B phase was ignored. As it is expected, micellar surface curvature should increase in the order $L_\alpha \rightarrow N_D \rightarrow N_B \rightarrow N_C \rightarrow H \rightarrow I$. This is due to the increase in repulsive forces between the surfactant head groups on the micelle surfaces which leads to the increase in the average area per the surfactant head group. There are two main important factors in obtaining different lyotropic structures: (a) the temperature and (b) the relative concentrations of the components in the mixture. In this study, the concentrations (in mole fractions) of the constituents in the mixtures were kept constant. As can be seen from Figure 4.8 and the birefringences-temperature partial phase diagrams, when the temperature was increased, the phase transitions occurred in

the order of $N_C \rightarrow N_B \rightarrow N_D$. This means that as the temperature increases, the micelle surface curvature becomes more planar due to the screening of the electrical charges/repulsions between the surfactant head groups on the micellar surfaces. Such screening can only be explained by the binding of more ionic species (surfactant counterions and/or electrolyte ions present in the mixture) to the micelle surfaces. However, according to the experimental results given in the literature for dodecyltrimethylammonium bromide (DTMABr)/water isotropic micelle solutions, which is similar surfactant to the molecules in this thesis, the degree of binding of Br ions, the counter ion of DTMABr, to the micelle surfaces decreases with increasing temperature (77,78). Since lyotropic systems have the same structural units as isotropic micellar solutions, it is known from studies in the literature that the scientific knowledge obtained from isotropic micellar solutions can be applied to lyotropic systems (29,79–82). Therefore, our results can be explained as follows. Since fewer Br ions are bound to the micelle surface when the temperature is increased, dye molecule-surfactant interactions should be stronger than Br ions due to the N_D phase formation. This may be attributed to more chaotropic properties of the anionic parts of the Sunset Yellow molecule than the Br ion (63). The interactions between these parts and the head groups of dodecylalkylammonium bromide surfactant molecules are stronger than the interactions between Br ions and surfactant head groups. Considering the IBM model, the binding of the Sunset Yellow molecule to the micelle surfaces with the increase in temperature causes the micelle growth in the A' x B' plane. Therefore, orientational fluctuations around the symmetry axis perpendicular to this plane became more dominant to stabilize the N_D phase at relatively high temperatures. At constant temperature and mixture composition, N_C (N_D/N_B) phase formation is favored as the head group size of the selected dodecylalkylammonium bromides (DDMABr, DDMEABr, and DTEABr) increases (decreases) due to the weakening (strengthening) of the interactions between the surfactant head groups on the micelle surfaces and the anionic groups of the Sunset Yellow molecule.

From polarized optical microscopy and laser conoscopy measurements, the relationship between nematic phase types and n_{avg} values has been revealed in detail, as mentioned above. Some additional mixtures were prepared to reveal the relationship between the n_{avg} values of the lamellar and hexagonal phase

structures, which are the other two lyotropic liquid crystal structures within the scope of this thesis (Table 4.4). Among the mixtures given in Table 3.1, the s9 mixture with the binary surfactant composition of $X_{DDMEABr}$:3.653 + X_{DDMABr}:1.566 (percent mole fraction) gives only the N_D phase (Table 4.1). The lamellar phase was obtained in the s10 mixture with the composition of $X_{DDMEABr}$:3.131 + X_{DDMABr}:2.087, which has a higher amount of DDMABr than the s9 mixture. In other words, a nematic-lamellar transition is now observed in the s10 mixture. Similarly, there was a transition from the N_C phase to the hexagonal phase when the s26 mixture ($X_{DDMEABr}$: 3.131 + X_{DTEABr}: 2.087) was prepared by increasing DTEABr in the s25 mixture ($X_{DDMEABr}$: 3.653 + X_{DTEABr}:1.566).

Table 4.4 Compositions of the mixtures in percent mole fraction (X) for the determination of nematic-lamellar and nematic-hexagonal boundaries according to the n_{avg} values for the binary surfactant systems DDMABr/DDMEABr/ SSY/DDeOH/water and DDMEABr/DTEABr/SSY/DDeOH/water.

Mixture	$\mathbf{X_{DDMABr}}$	$\mathbf{X_{DDMEABr}}$	$\mathbf{X_{DTEABr}}$	$\mathbf{X_{SSY}}$	$\mathbf{X_{DDeOH}}$	$\mathbf{X_{water}}$	**Phase type**	$\mathbf{n_{avg}}$
s33	1.722	3.496	0.000	0.131	2.131	92.519	L_α	3.34
s34	1.670	3.548	0.000	0.131	2.131	92.519	L_α	3.36
s35	1.305	3.914	0.000	0.131	2.131	92.519	$L_\alpha + N_D$	3.50
s36	0.000	3.444	1.774	0.131	2.131	92.519	N_C	4.68
s37	0.000	3.392	1.826	0.131	2.131	92.519	N_C	4.70
s38	0.000	2.871	2.348	0.131	2.131	92.519	*H*	4.90

Considering the laser conoscopy measurements of the mixtures given in Table 4.1, Table 4.2, and Table 4.4 that give nematic phases (laser conoscopy technique cannot be applied to hexagonal and lamellar phases) and the polarized

optical microscopy measurements of the others, the dependence of the formation of the lyotropic structures on the head group size (n_{avg}) of dodecylalkylammonium bromides is, with the experimental error as follows:

$$n_{avg}: \quad 2.00 \xrightarrow{L_\alpha} 3.45 \xrightarrow{N_D} 3.82 \xrightarrow{N_D+N_B} 3.90 \xrightarrow{N_D+N_B+N_C} 4.22 \xrightarrow{N_C} 4.75 \xrightarrow{H} 6.00$$

Consequently, the relationship between the average area per head group and the formation of different lyotropic structures (considering the formation of the N_B, lamellar and hexagonal phases) in the same lyotropic system (binary dodecylalkylammonium bromides) by controlling head group size has been revealed for the first time within the scope of this thesis. In the following part, some important information is given to support the laser conoscopy and POM results, and their interpretations.

4.4 Small-Angle X-ray Scattering Measurements

Small-angle X-ray scattering (SAXS) is a useful technique to estimate some structural parameters of the different lyotropic phases. In the frame of this thesis, this technique was used to measure and calculate structural parameters for the nematic, hexagonal and lamellar lyotropic phases.

For the three nematic phases, it was supposed that the basic units are anisometric micelles with orthorhombic or biaxial symmetry, as proposed by the Intrinsic Biaxial Micelles (IBM) model (31). The biaxial micelles have approximately the same average shape across the different nematic phases for the same sample. Therefore, it was supposed an average shape of a rectangular parallelepiped for the micelles in the three nematic phases. This is the simplest three-dimensional shape with orthorhombic symmetry. Details of this approximated model and how to use it to extract information from SAXS measurements are presented in (63) and in its Supporting Information.

The SAXS aligned patterns of the nematic phases were used to measure the average dimensions of the available volume per micelle (A, B, C) directly from the peak positions of the nematic bands (31). The following structural parameters were calculated from the model-based analysis of (63): average dimensions of the micelles core (A, B, C), the average area per polar head (a_0) and the shape anisotropy (SA).

For the hexagonal and lamellar phases, simplified models presented in (83) were used for the calculation of the parameters. Prior to the model analysis, the phase identities were confirmed by the SAXS patterns, which are formed by a series of diffraction rings for both phases. For the hexagonal phase, the q positions of the consecutive rings are in ratios of $1:\sqrt{3}:\sqrt{4}:\sqrt{7}:$ ..., while for the lamellar phases the ratios are $1:2:3:4:$ .... The peak positions of first two q values and their ratios for the lamellar and hexagonal phases of some studied samples are given in Table 4.5.

Table 4.5 The *q* positions of the first two consecutive rings for some samples, which give only lamellar and hexagonal phases in $Å^{-1}$ with standard deviations (STD). q_2/q_1 values are the ratios with their standard deviations.

Sample (n_{avg})	**Phase**	**T/°C**	**1st Peak**		**2nd Peak**		**q_2/q_1**	**STD**
			$q_1/Å^{-1}$	**STD/$Å^{-1}$**	**$q_2/Å^{-1}$**	**STD/$Å^{-1}$**		
s16 (2.00)	L_α	15.0	0.1268	0.0000	0.2532	0.0003	1.997	0.002
		25.0	0.1275	0.0000	0.2547	0.0002	1.998	0.002
		30.0	0.1282	0.0000	0.2563	0.0003	1.999	0.002
s12 (2.80)	L_α	15.0	0.1406	0.0001	0.2810	0.0016	1.998	0.011
		25.0	0.1409	0.0000	0.2820	0.0012	1.999	0.009
		30.0	0.1413	0.0001	0.2820	0.0006	1.993	0.005
s34 (3.36)	L_α	25.0	0.1459	0.0000	0.2908	0.0014	1.993	0.010
		30.0	0.1460	0.0001	0.2914	0.0015	1.996	0.011
s9 (3.40)	L_α	15.0	0.1459	0.0004	0.2913	0.0003	1.996	0.006
		25.0	0.1462	0.0001	0.2903	0.0006	1.986	0.004
		30.0	0.1474	0.0001	0.2940	0.0004	1.994	0.003
s35 (3.50)	L_α	25.0	0.1468	0.0000	0.2914	0.0015	1.985	0,010
		30.0	0.1476	0.0001	0.2949	0.0010	1.998	0.006
s26 (4.80)	H	15.0	0.1485	0.0001	0.2574	0.0010	1.733	0.008
s38 (4.90)	H	15.0	0.1343	0.0001	0.2305	0.0015	1.716	0.011
s29 (5.40)	H	15.0	0.1355	0.0000	0.2343	0.0008	1.729	0.006
s32 (6.00)	H	15.0	0.1390	0.0001	0.2409	0.0003	1.733	0.003
		30.0	0.1446	0.0000	0.2501	0.0006	1.730	0.004

The structural model for the hexagonal phase considers an ideal regular hexagonal set of infinite cylinders formed by amphiphilic molecules such that the amphiphiles' alkyl chains form the internal parts of the cylinders, i.e., their hydrophobic core. The hydrophilic ends of the amphiphiles are on the surface of the cylinders, in contact with the water. The cylinders are surrounded by water and other hydrophilic components. The dimension *d* of the hexagonal lattice is determined by measuring the spacings of the diffraction lines. From the simple geometrical model, the diameter d_a of the cylinders and the average area available per polar head a_0, at the water-amphiphile interface, are given by,

$$d_a = d\left[\frac{2\sqrt{3}}{\pi}\frac{1}{1+\bar{v_w}/\bar{v_a}\cdot(1-c)/c}\right]^{1/2} \quad (4.2)$$

$$a_0 = \frac{4M_a\bar{v_a}}{d_a N_A}10^{24} \quad (4.3)$$

where M_a is the molar mass of the amphiphilic molecule, N_A is the Avogadro number, c is the mass fraction of amphiphilic molecules in the mixture, and $\bar{v_w}$ and $\bar{v_a}$ are the partial specific volumes of the hydrophilic and hydrophobic regions, respectively.

The structural model for the lamellar phase considers an infinite stack of parallel and equidistant plane sheets. The sheets are formed by a double layer of amphiphilic molecules such that the alkyl chains form its internal parts and the hydrophilic ends of the amphiphiles are on the surface in contact with the water layers. The amphiphilic sheets are separated by layers of water and other hydrophilic components.

From the measurements of the spacings of the diffraction lines, the periodic distance *d* of the stack is obtained. From the model, it can be determined the thickness of the amphiphilic layer d_a and of the water layer *w*, and the average area available per polar head a_0,

$$d_a = \frac{d}{[1+\bar{v_w}/\bar{v_a}\cdot(1-c)/c]} \quad (4.4)$$

$$w = d - d_a \quad (4.5)$$

$$a_0 = \frac{2M_a\bar{v_a}}{d_a N_A}10^{24} \quad (4.6)$$

where the other parameters are the same of the ones described above.

Figures 4.9-4.59 show the 2D small-angle X-ray scattering (SAXS) patterns and their frame integrations of the lamellar, nematic and hexagonal phases for some samples in Tables 3.1, 3.2 and 4.4.

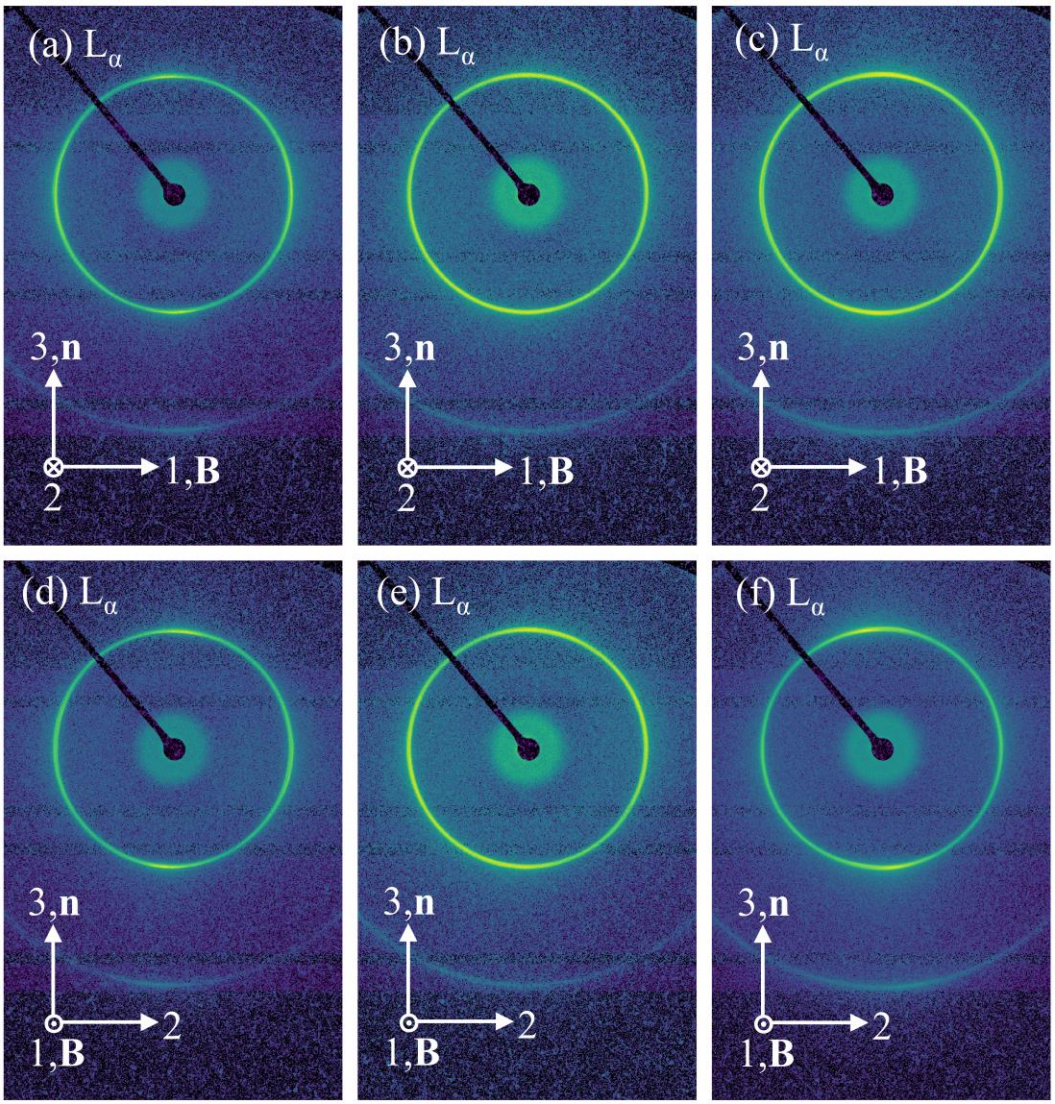

Figure 4.9 The 2D small-angle X-ray scattering (SAXS) patterns of the lamellar (L_α) phase for sample s16 (n_{avg}: 2.00). The patterns (a), (b) and (c) were measured at 15.0 °C, 25.0 °C and 30.0 °C, respectively, where the X-ray beam is along 2 and perpendicular to the magnetic field (**B)** direction (perpendicular, PP, position). The patterns (d), (e) and (f) were obtained at the same temperatures while the X-ray beam is along 1 and therefore parallel to the **B** direction (parallel, PR, position).

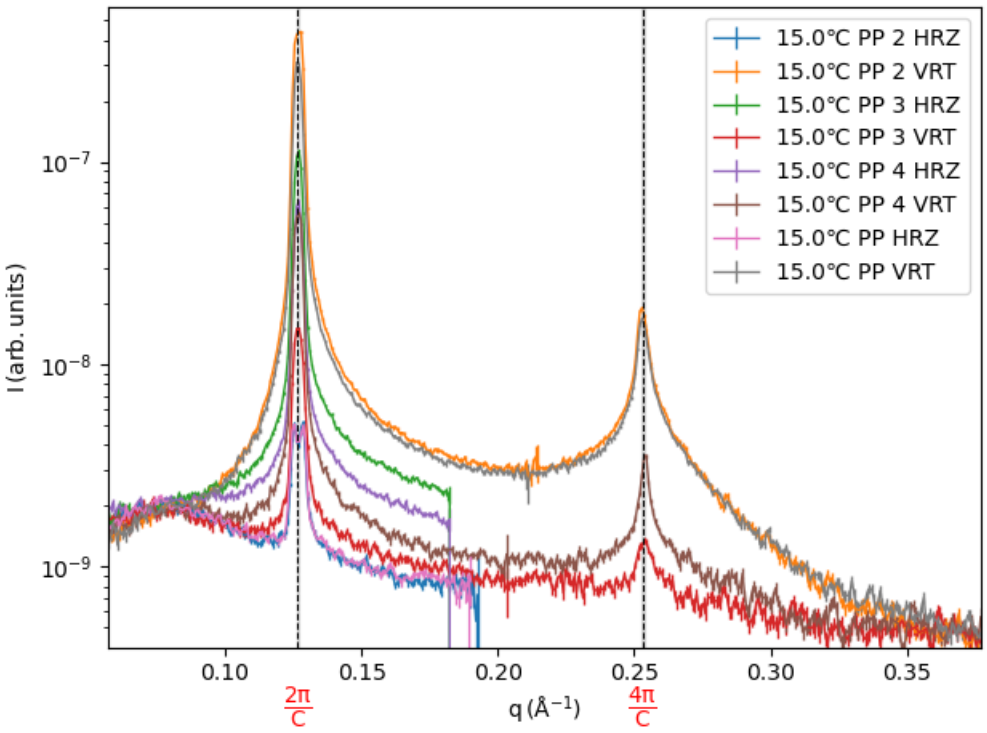

Figure 4.10 Frame integration of the 2D SAXS patterns of the lamellar phase of sample s16 at 15°C for the PP position.

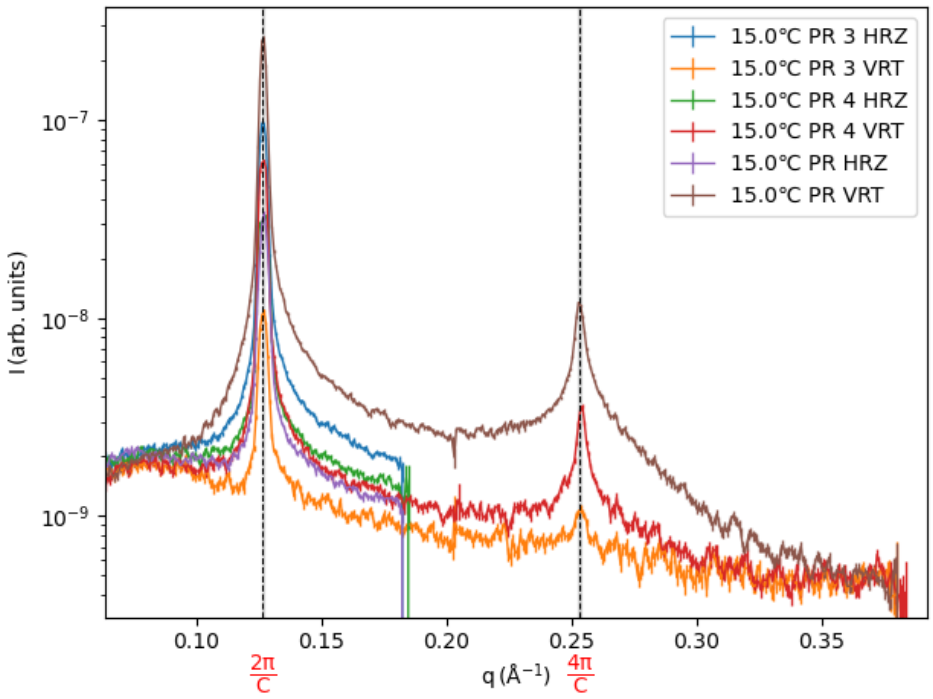

Figure 4.11 Frame integration of the 2D SAXS patterns of the lamellar phase of sample s16 at 15°C for the PR position

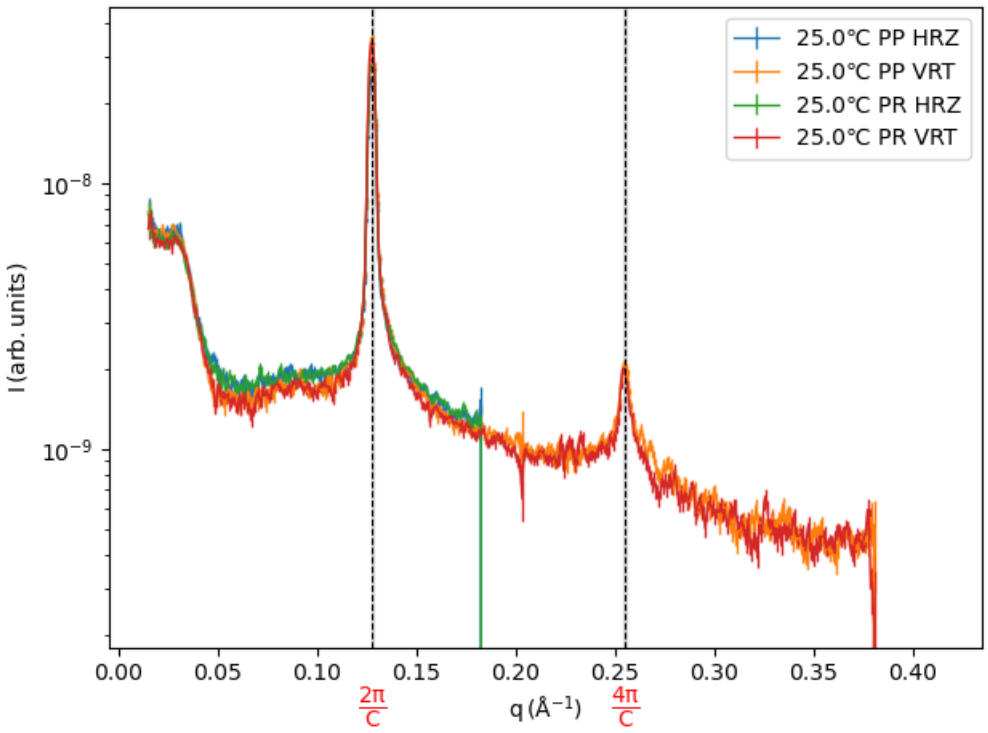

Figure 4.12 Frame integration of the 2D SAXS patterns of the lamellar phase of sample s16 at 25°C for the PP and PR positions.

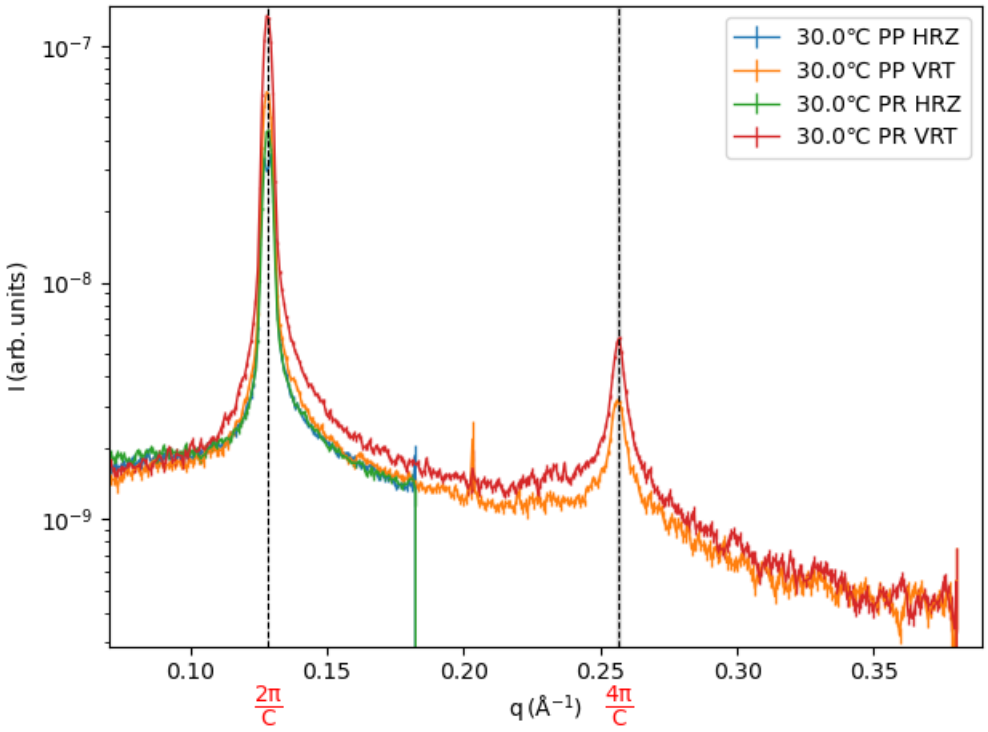

Figure 4.13 Frame integration of the 2D SAXS patterns of the lamellar phase of sample s16 at 30°C for the PP and PR positions.

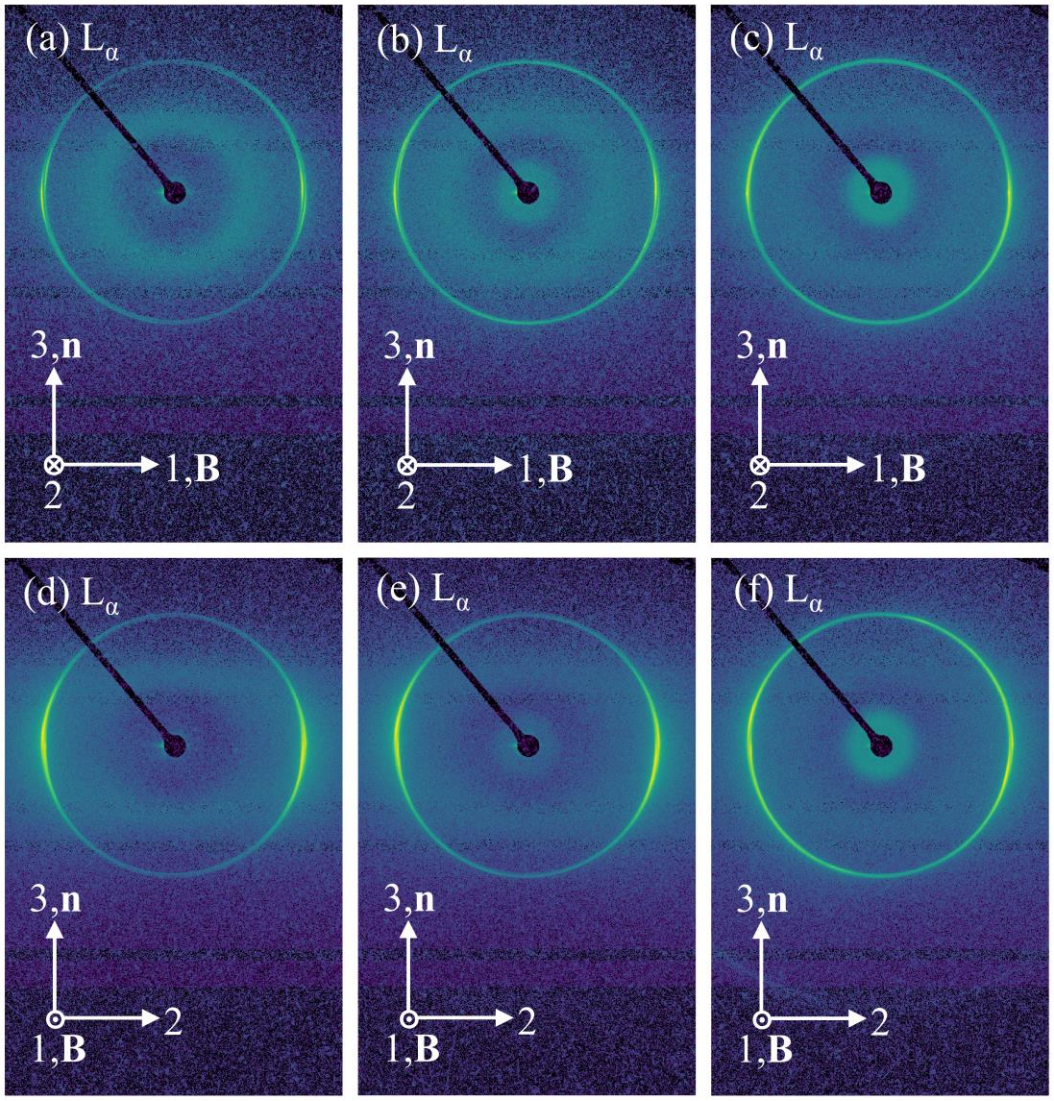

Figure 4.14 The 2D small-angle X-ray scattering (SAXS) patterns of the lamellar (L_α) phase for sample s12 (n_{avg}: 2.80). The patterns (a), (b) and (c) were measured at 15.0 °C, 25.0 °C and 30.0 °C, respectively, at the PP position. The patterns (d), (e) and (f) were obtained at the same temperatures at the PR position.

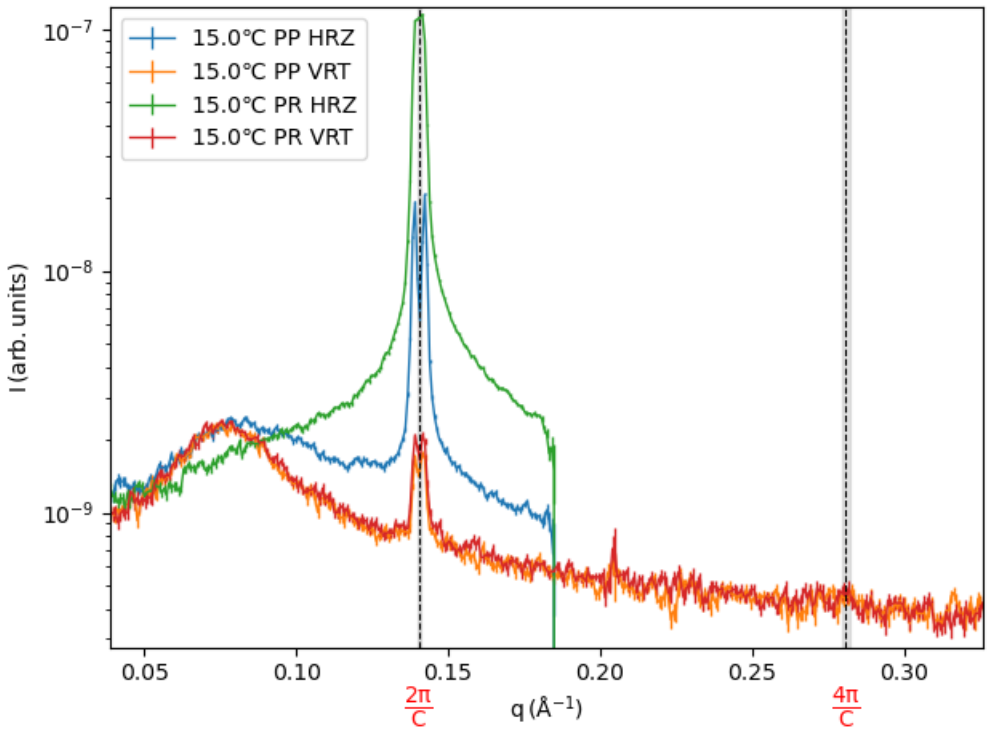

Figure 4.15 Frame integration of the 2D SAXS patterns of the lamellar phase of sample s12 at 15°C for the PP and PR positions.

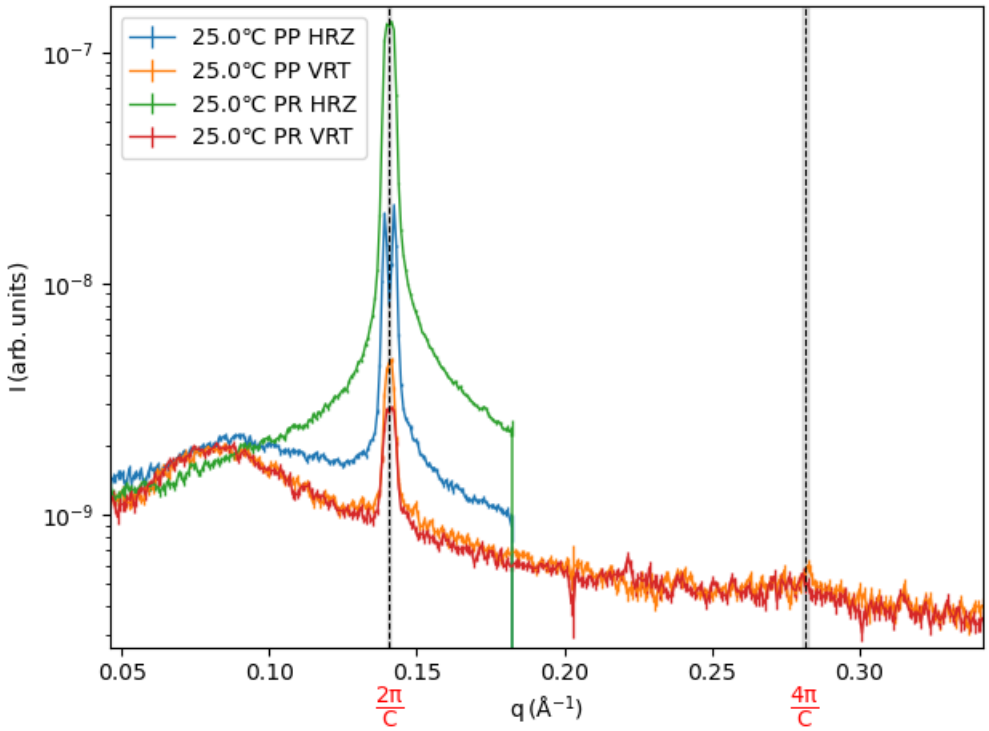

Figure 4.16 Frame integration of the 2D SAXS patterns of the lamellar phase of sample s12 at 25°C for the PP and PR positions.

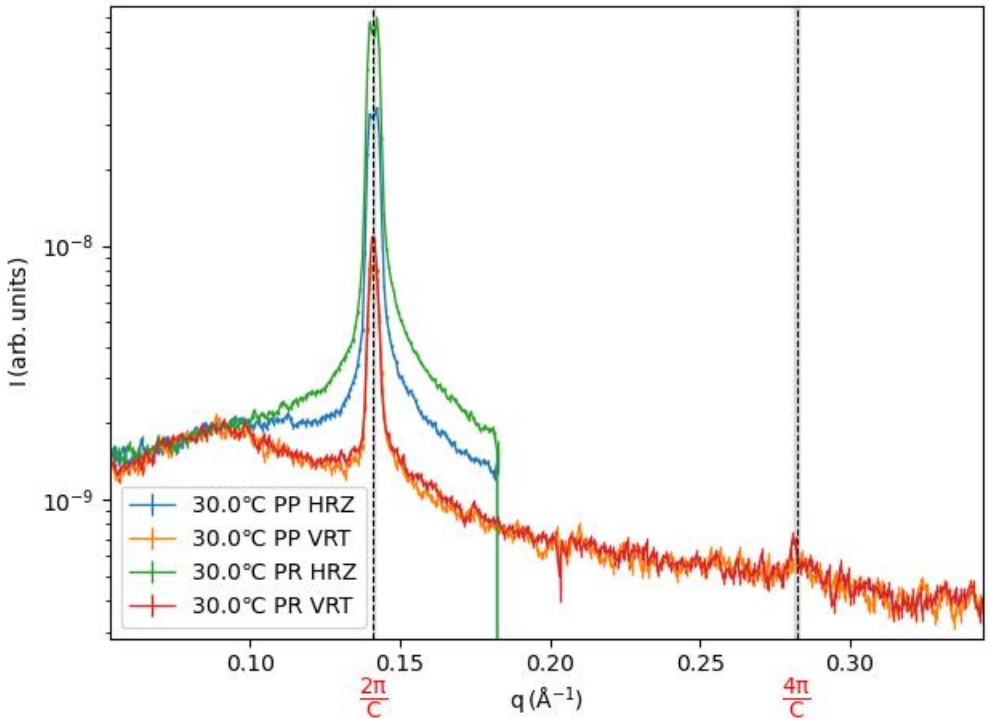

Figure 4.17 Frame integration of the 2D SAXS patterns of the lamellar phase of sample s12 at 30°C for the PP and PR positions.

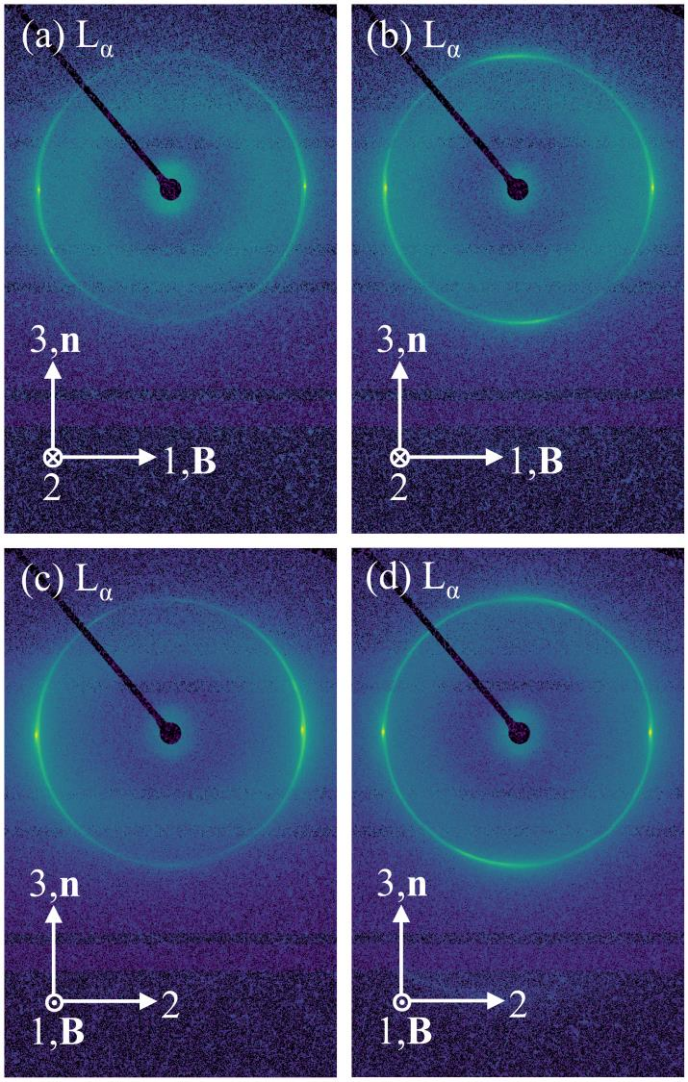

Figure 4.18 The 2D small-angle X-ray scattering (SAXS) patterns of the lamellar (L_α) phase for sample s34 (n_{avg}: 3.36). The patterns (a) and (b) were measured at 25.0 °C and 30.0 °C, respectively, at the PP position. The patterns (c) and (d) were obtained at the same temperatures at the PR position.

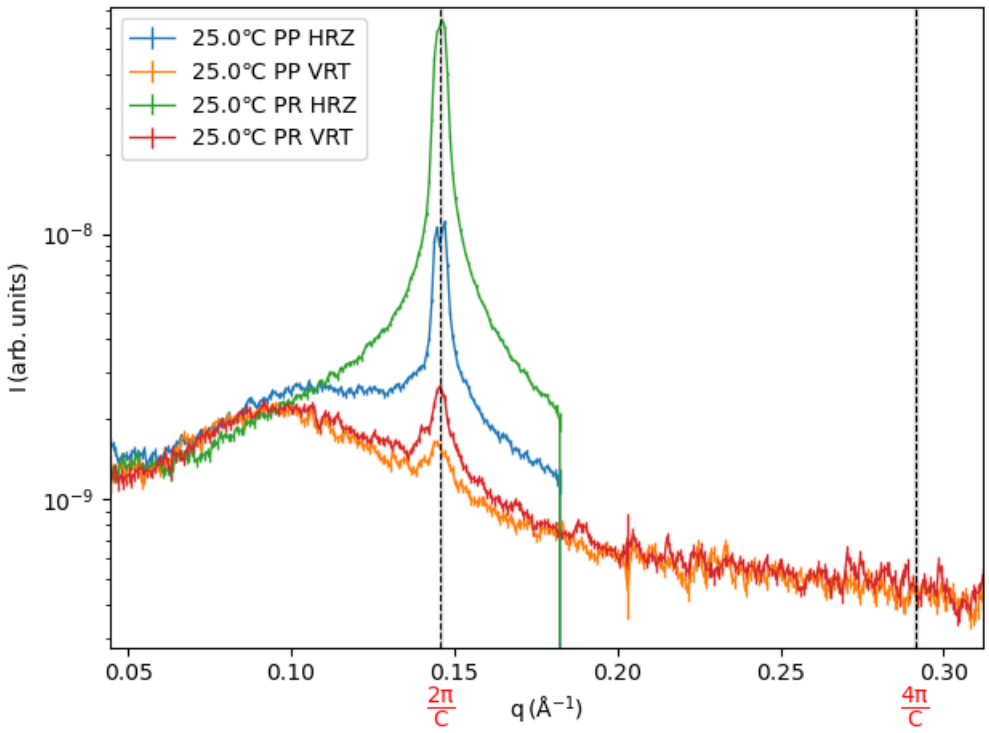

Figure 4.19 Frame integration of the 2D SAXS patterns of the lamellar phase of sample s34 at 25°C for the PP and PR positions.

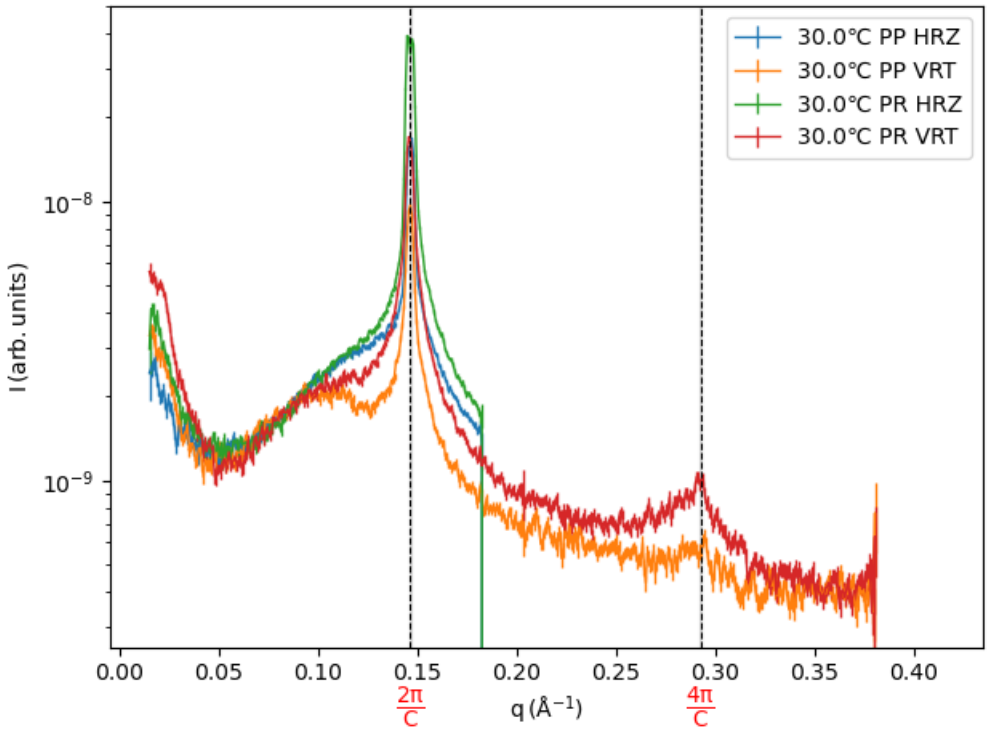

Figure 4.20 Frame integration of the 2D SAXS patterns of the lamellar phase of sample s34 at 30°C for the PP and PR positions.

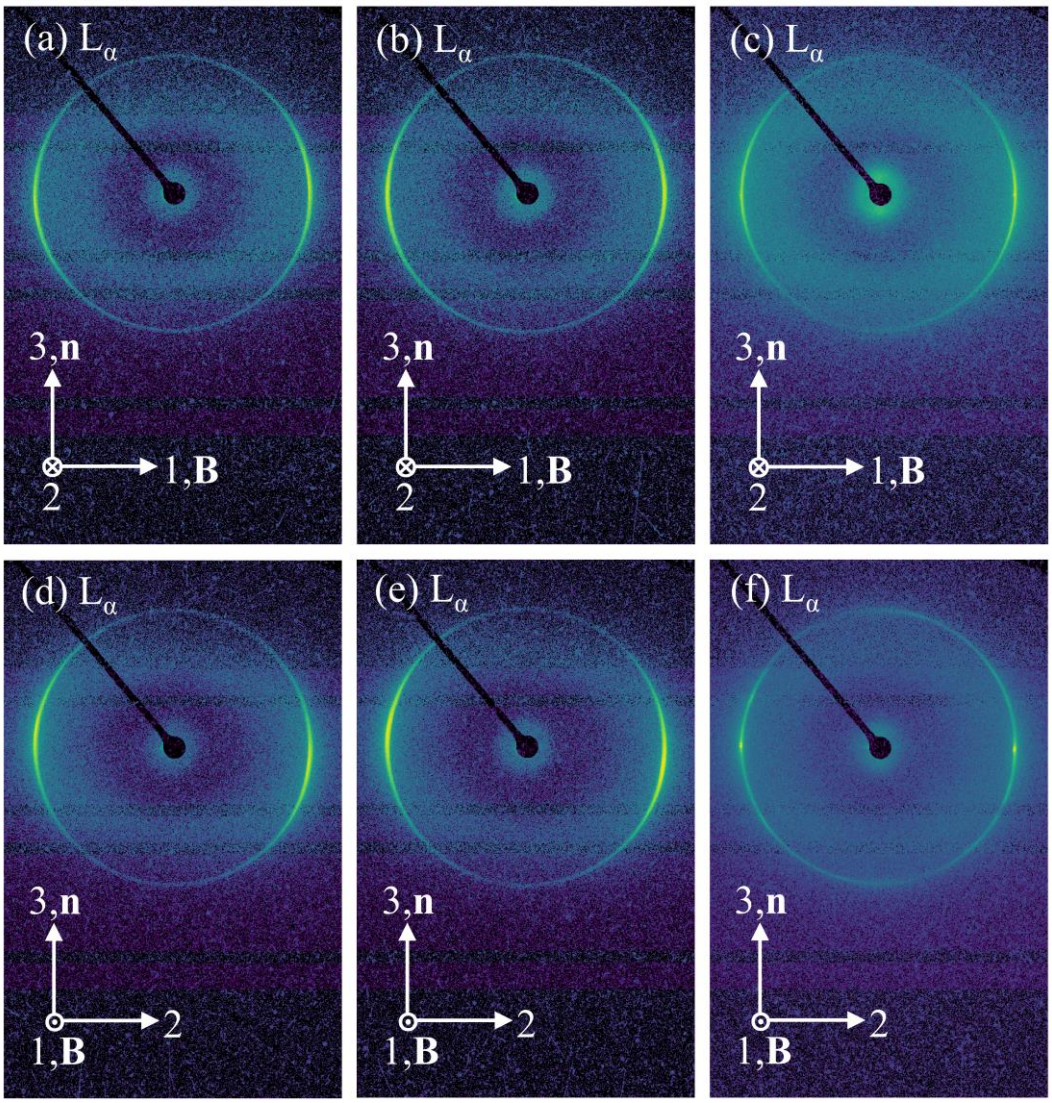

Figure 4.21 The 2D small-angle X-ray scattering (SAXS) patterns of the lamellar (L_α) phase for sample s9 (n_{avg}: 3.40). The patterns (a), (b) and (c) were measured at 15.0 °C, 25.0 °C, and 30.0 °C, respectively, at the PP position. The patterns (d), (e) and (f) were obtained at the same temperatures at the PR position.

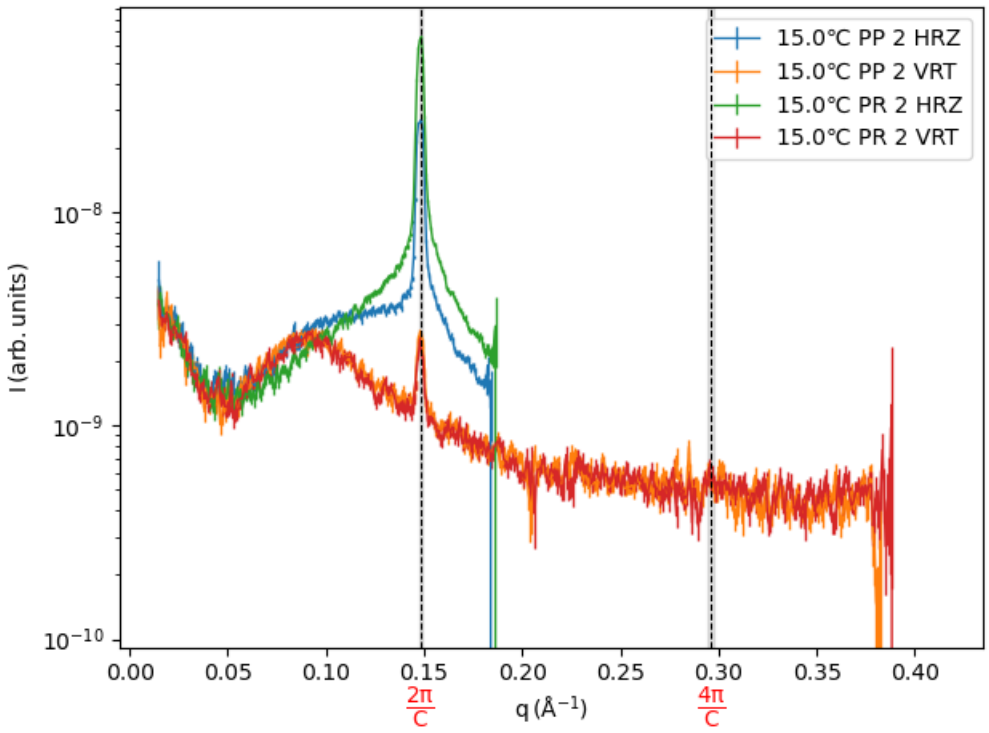

Figure 4.22 Frame integration of the 2D SAXS patterns of the lamellar phase of sample s9 at 15°C for the PP and PR positions.

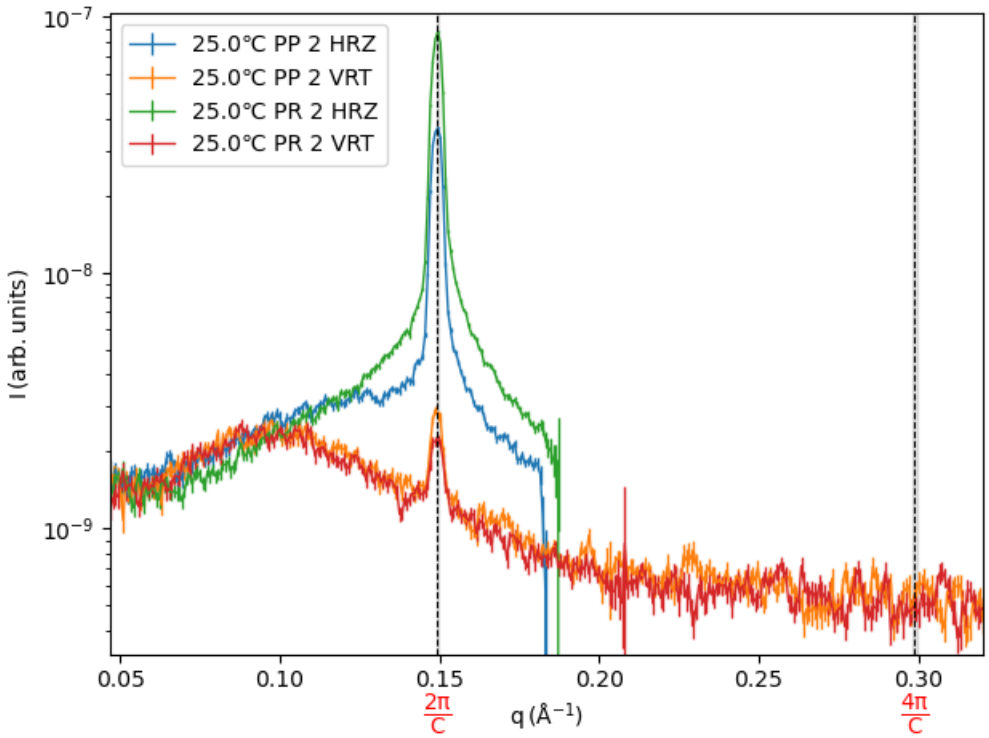

Figure 4.23 Frame integration of the 2D SAXS patterns of the lamellar phase of sample s9 at 25°C for the PP and PR positions.

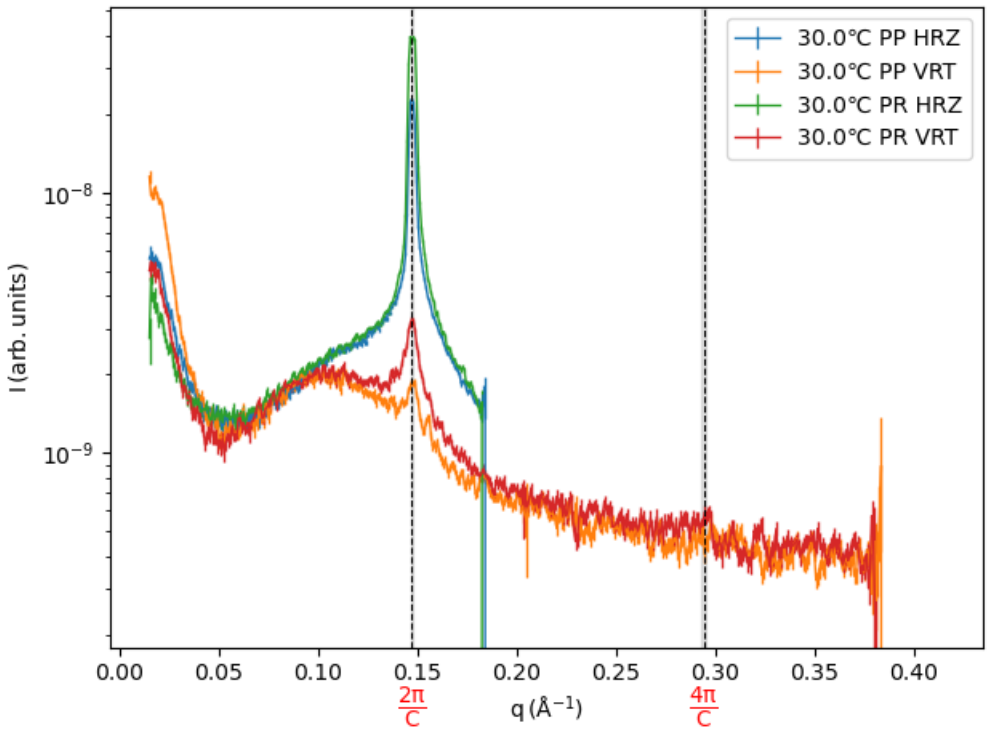

Figure 4.24 Frame integration of the 2D SAXS patterns of the lamellar phase of sample s9 at 30°C for the PP and PR positions.

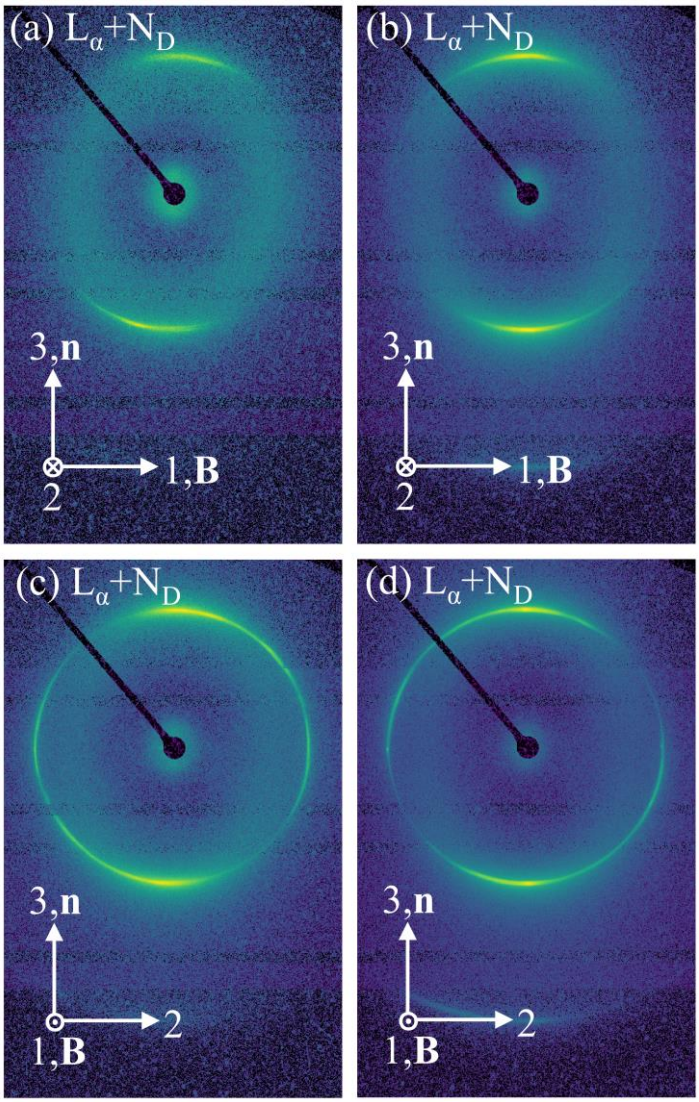

Figure 4.25 The 2D small-angle X-ray scattering (SAXS) patterns of sample s35 (n_{avg}: 3.50) at two different temperatures. The patterns (a) and (b) were measured at 25.0 °C and 30 °C, respectively, at the PP position. The patterns (c), and (d) were obtained at the same temperatures at the PR position.

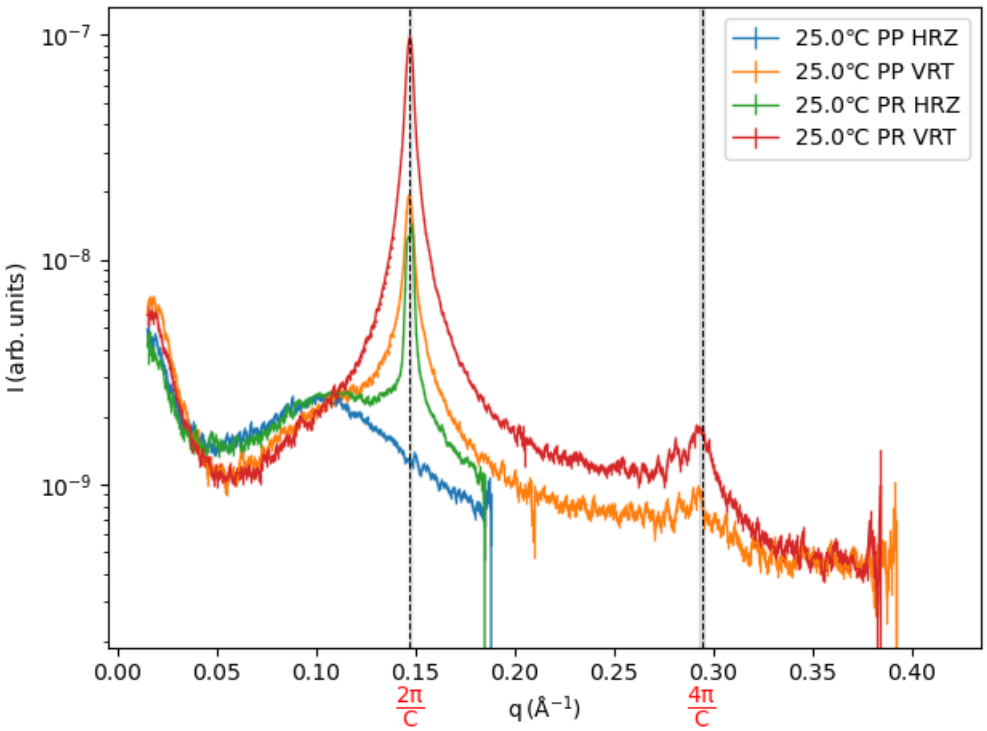

Figure 4.26 Frame integration of the 2D SAXS patterns of the lamellar+N_D phases of sample s35 at 25°C for the PP and PR positions.

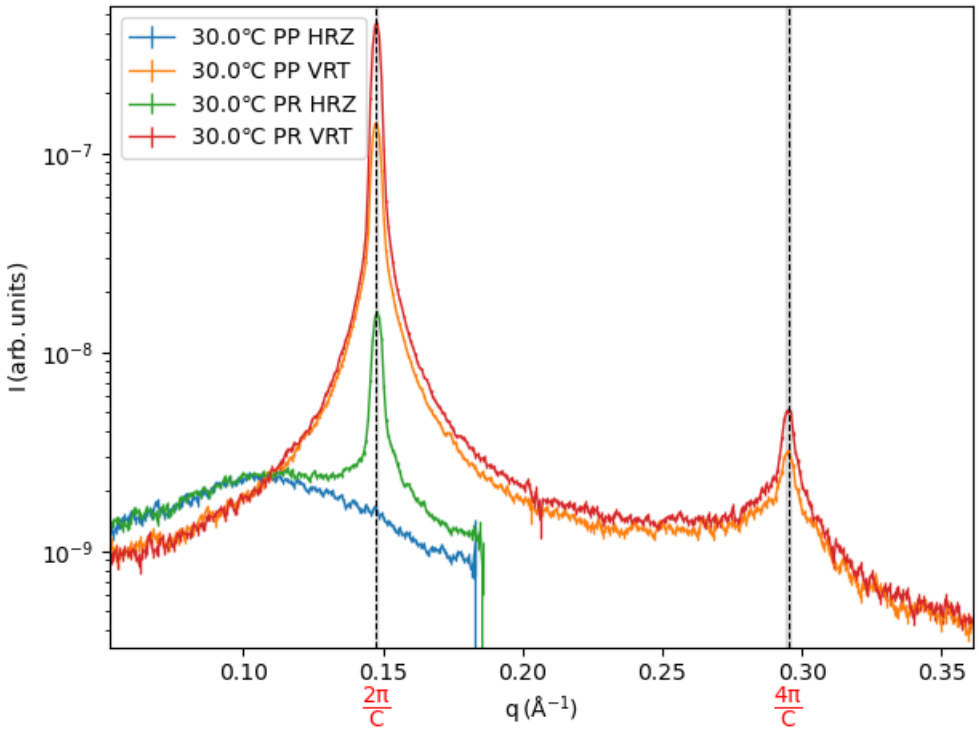

Figure 4.27 Frame integration of the 2D SAXS patterns of the lamellar+N_D phases of sample s35 at 30°C for the PP and PR positions

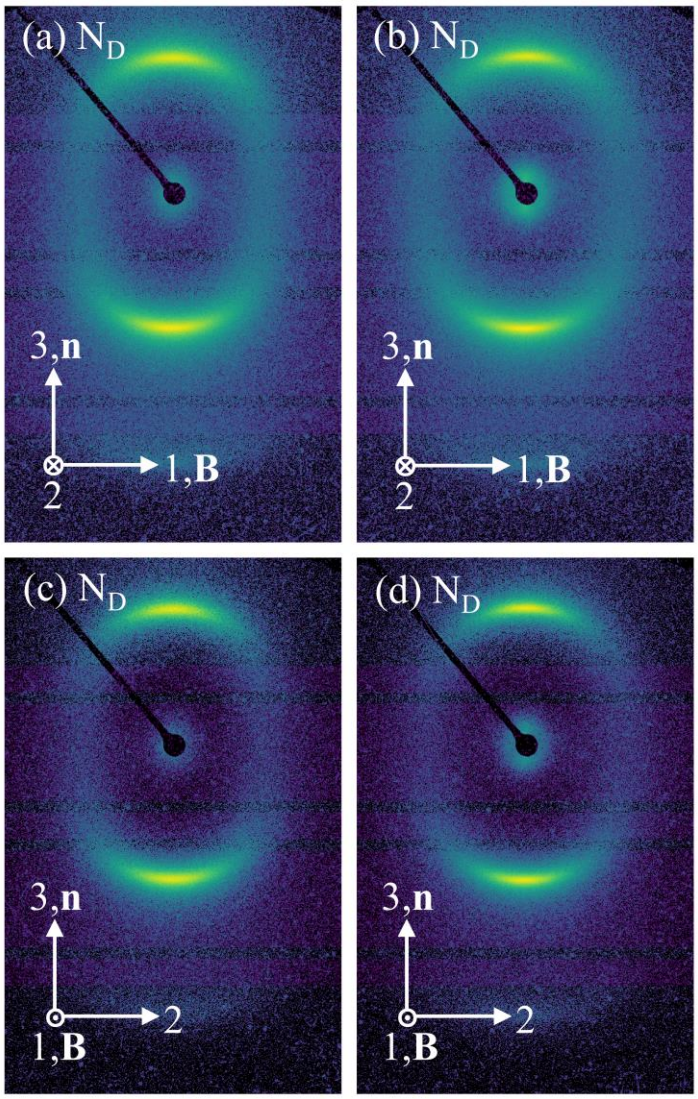

Figure 4.28 The 2D small-angle X-ray scattering (SAXS) patterns of the aligned nematic N_D phases at two different temperatures for sample s8 (n_{avg}: 3.60). The patterns (a) and (b) were measured at 15.0 °C and 25 °C, respectively, at the PP position. The patterns (c) and (d) were obtained at the same temperatures at the PR position.

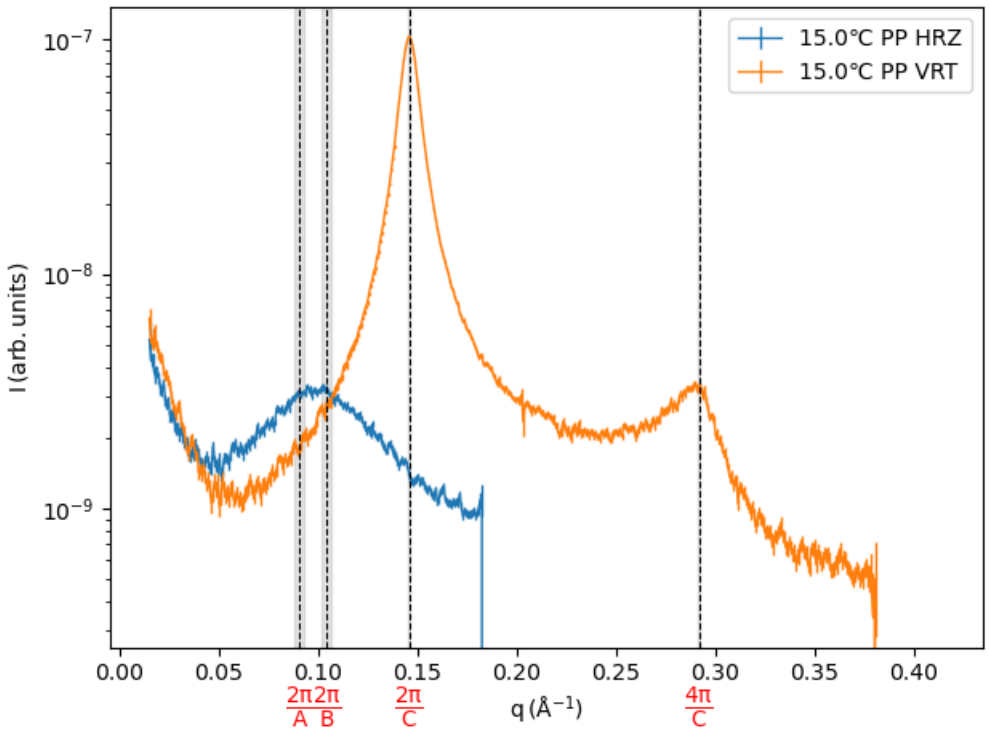

Figure 4.29 Frame integration of the 2D SAXS patterns of the aligned N_D phase of sample s8 at 15.0°C for the PP position. For the PR position, a similar frame integration was obtained.

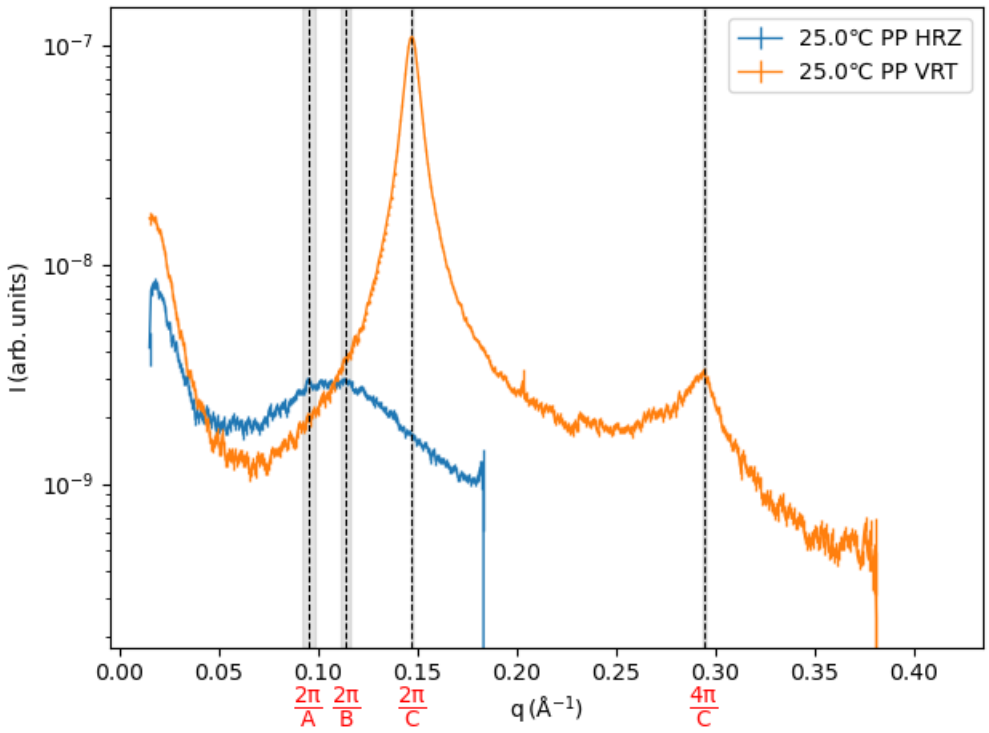

Figure 4.30 Frame integration of the 2D SAXS patterns of the aligned N_D phase of sample s8 at 25.0°C for the PP position. For the PR position, a similar frame integration was obtained.

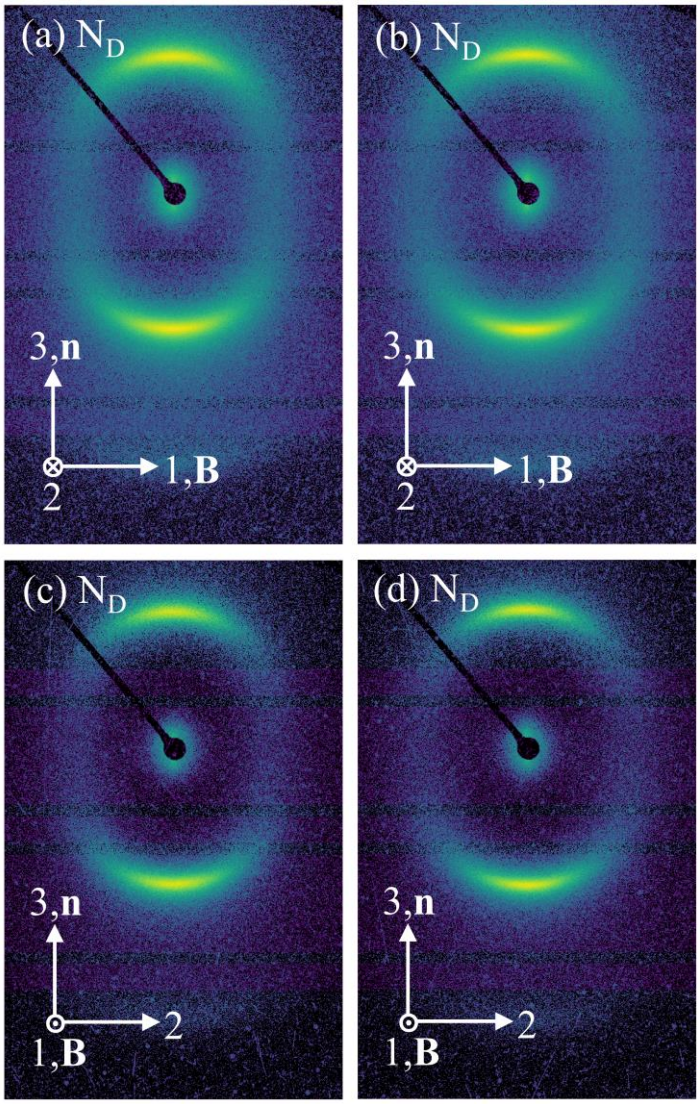

Figure 4.31 The 2D small-angle X-ray scattering (SAXS) patterns of the aligned nematic N_D phases at two different temperatures for sample s17 (n_{avg}: 3.72). The patterns (a) and (b) were measured at 15.0 °C and 25 °C, respectively, at the PP position. The patterns (c) and (d) were obtained at the same temperatures at the PR position.

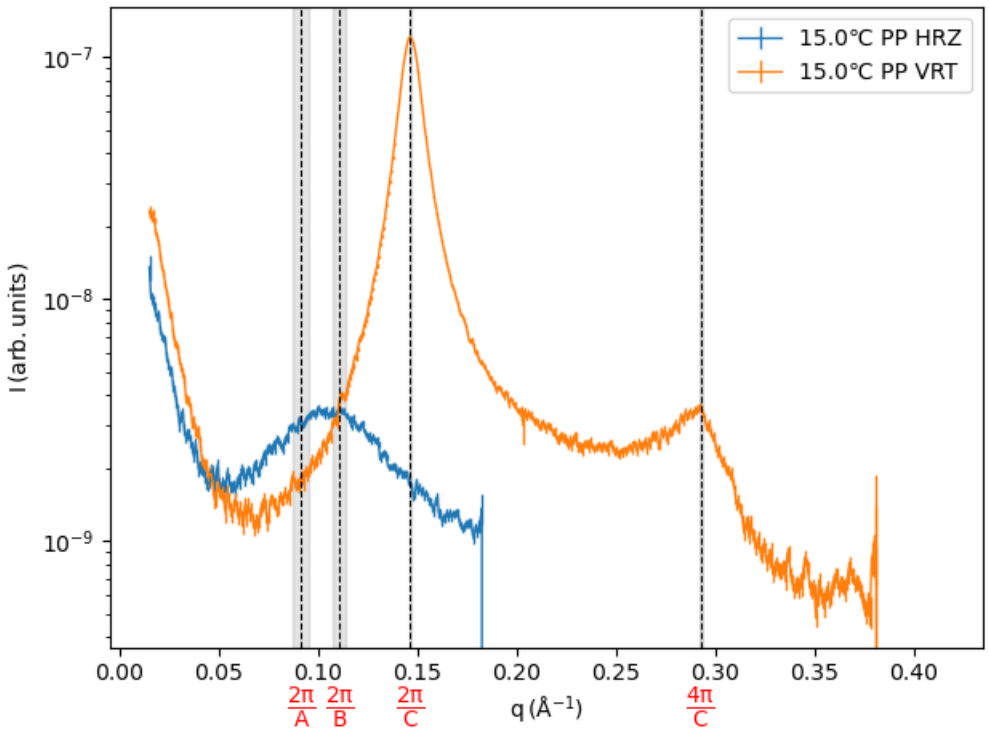

Figure 4.32 Frame integration of the 2D SAXS patterns of the aligned N_D phase of sample s17 at 15.0°C for the PP position. For the PR position, a similar frame integration was obtained.

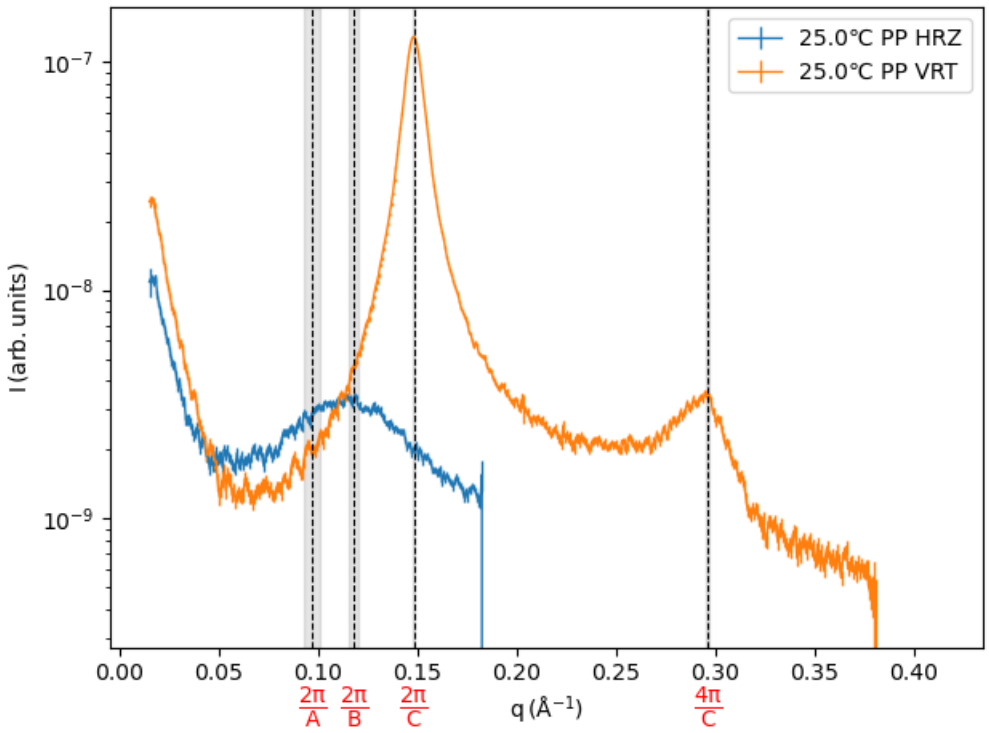

Figure 4.33 Frame integration of the 2D SAXS patterns of the aligned N_D phase of sample s17 at 25.0°C for the PP position. For the PR position, a similar frame integration was obtained.

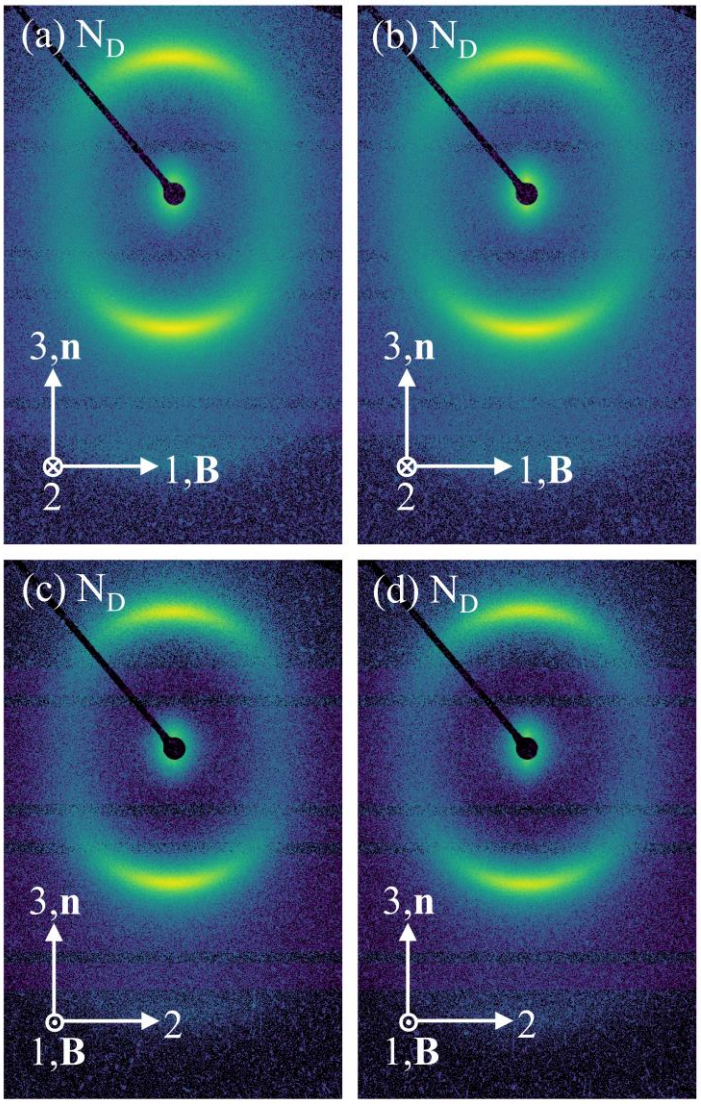

Figure 4.34 The 2D small-angle X-ray scattering (SAXS) patterns of the aligned nematic N_D phases at two different temperatures for sample s5 (n_{avg}: 3.80). The patterns (a) and (b) were measured at 15.0 °C and 25 °C, respectively, at the PP position. The patterns (c) and (d) were obtained at the same temperatures at the PR position.

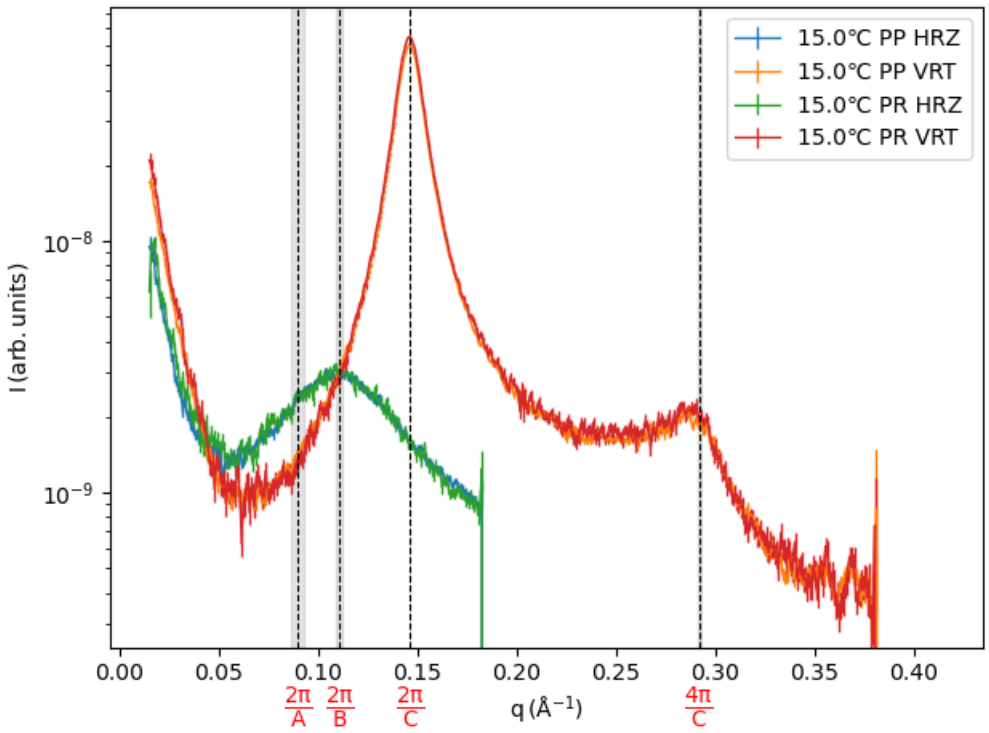

Figure 4.35 Frame integration of the 2D SAXS patterns of the aligned N_D phase of sample s5 at 15.0°C for the PP and PR positions.

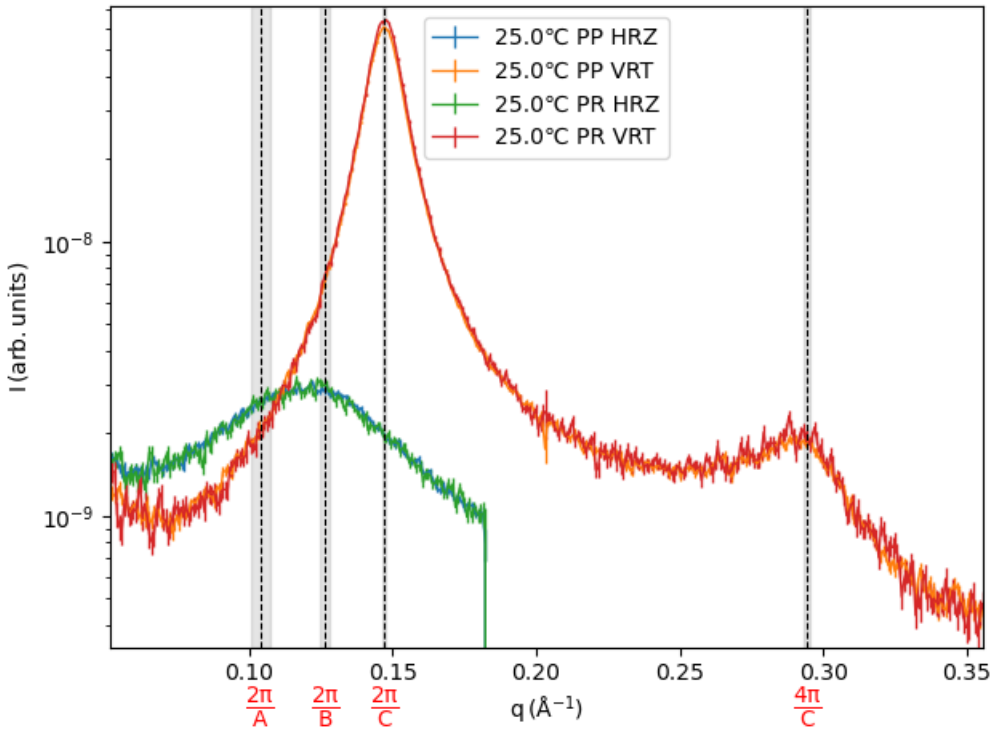

Figure 4.36 Frame integration of the 2D SAXS patterns of the aligned N_D phase of sample s5 at 25.0°C for the PP and PR positions.

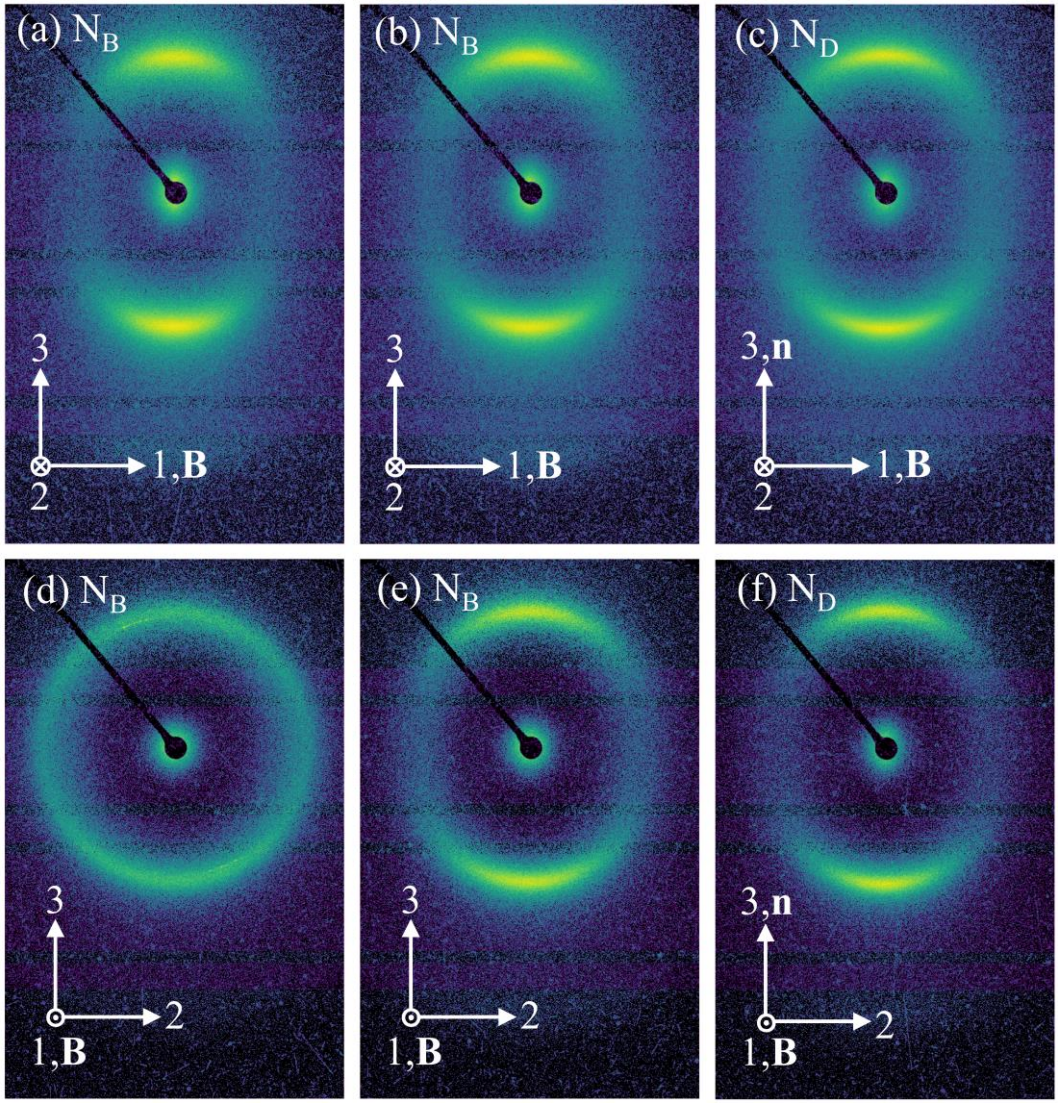

Figure 4.37 The 2D small-angle X-ray scattering (SAXS) patterns of the aligned nematic N_B, N_B and N_D phases for sample s4 (n_{avg}: 3.84). The patterns (a), (b) and (c) were measured at 13.7 °C, 14.4 °C, and 15.0 °C, respectively, at the PP position. The patterns (d), (e) and (f) were obtained at the same temperatures at the PR position.

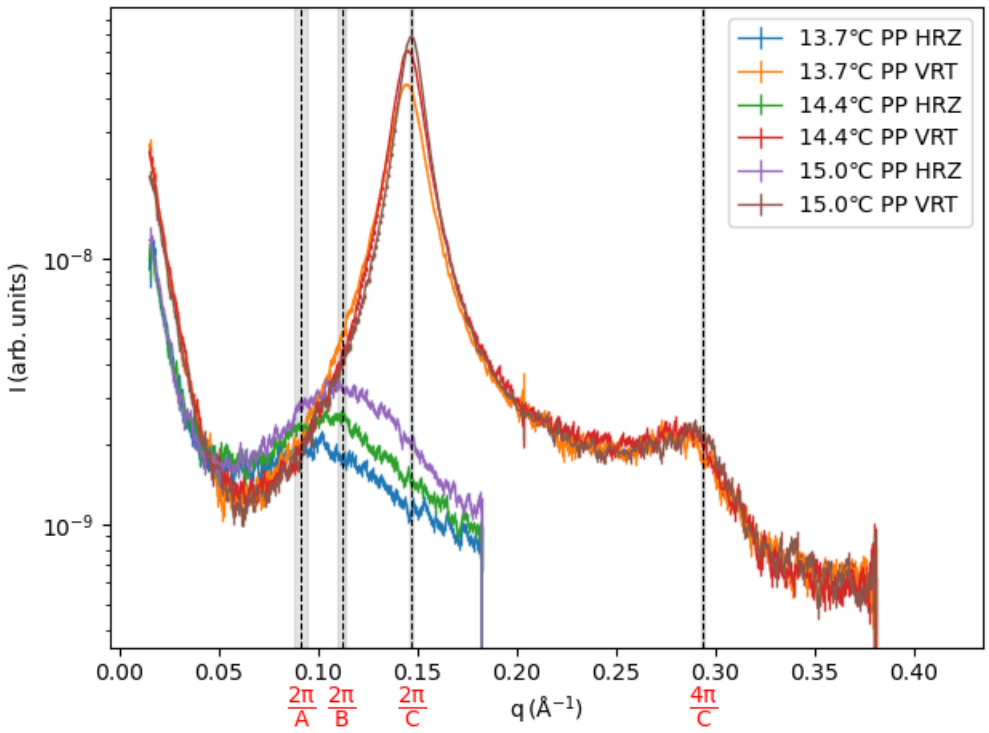

Figure 4.38 Frame integration of the 2D SAXS patterns of the aligned N_B, N_B and N_D phases of sample s4 at 13.7 °C, 14.4 °C, and 15.0 °C, respectively for the PP position.

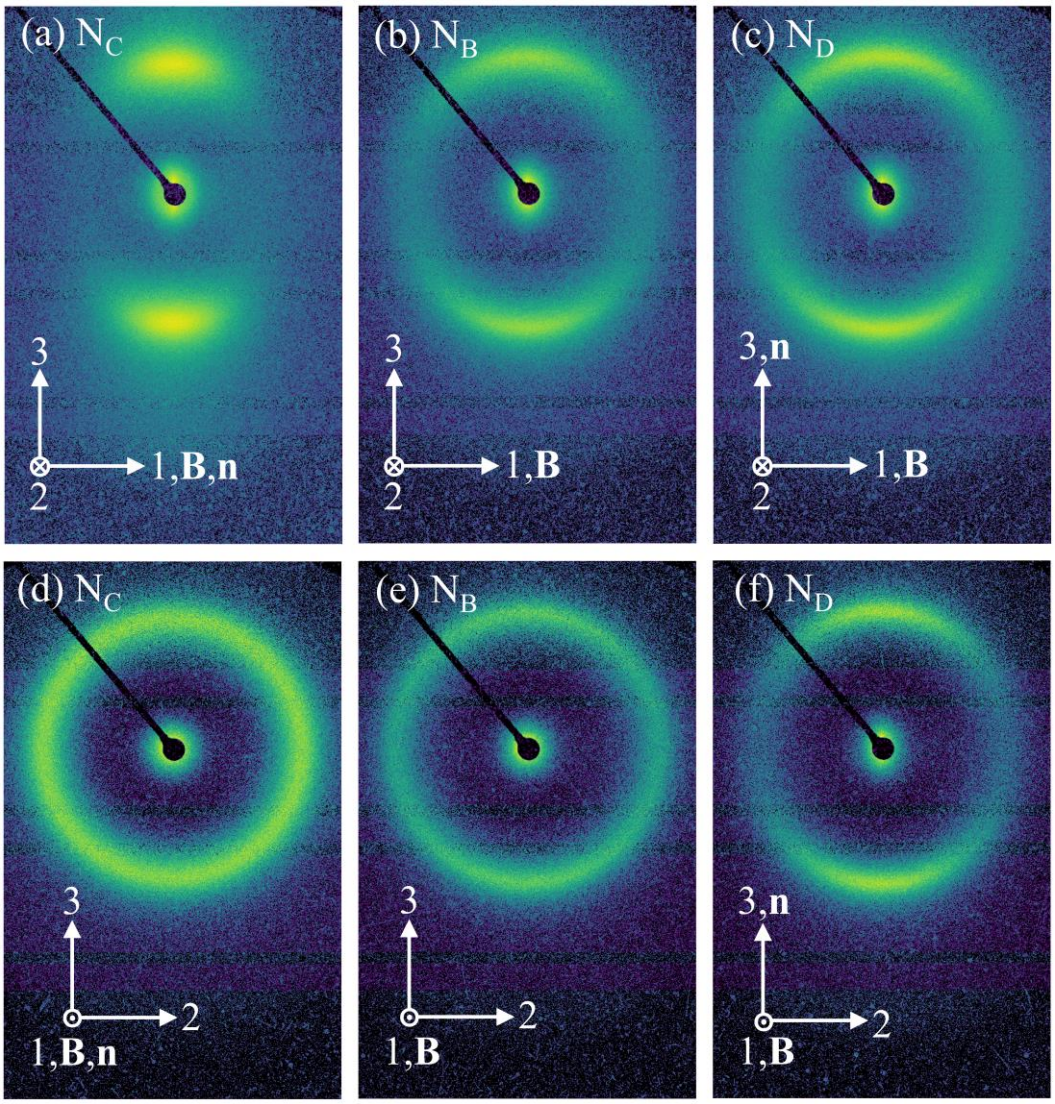

Figure 4.39 The 2D small-angle X-ray scattering (SAXS) patterns of the aligned nematic N_C, N_B and N_D phases for sample s0 (n_{avg}: 4.00). The patterns were measured at 15.0 °C, 21.4 °C and 25.0 °C, respectively, at the PP position. The patterns (d), (e) and (f) were obtained at the same temperatures at the PR position. In the N_B phase region, two additional patterns were measured at 21.1°C and 21.9 °C, and similar patterns were obtained as given at 21.4 °C.

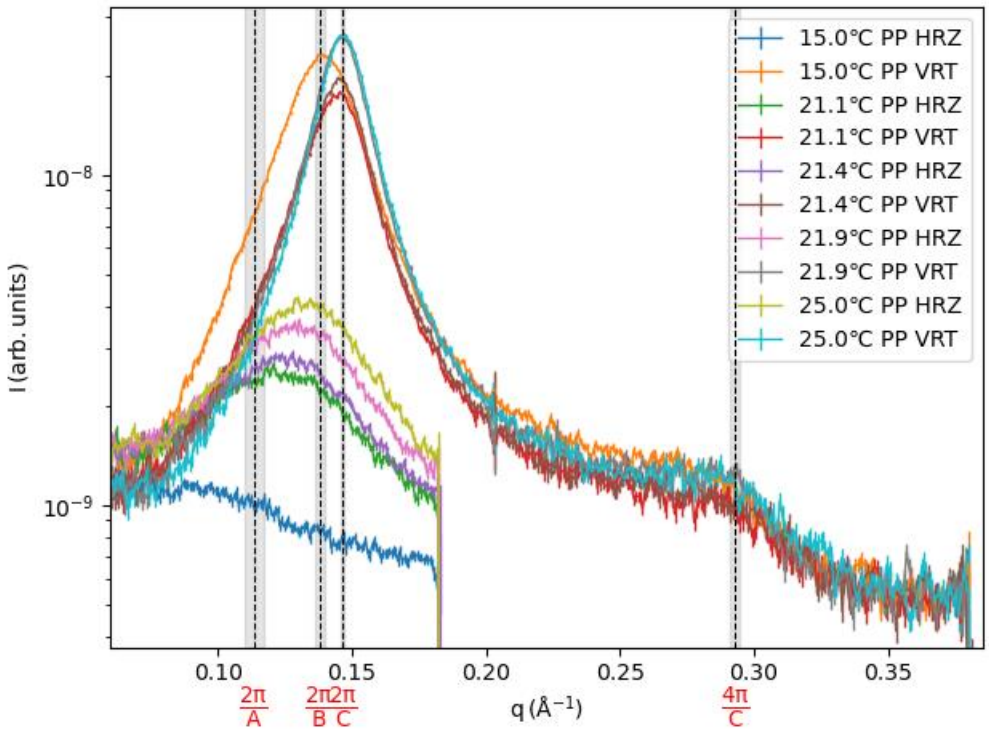

Figure 4.40 Frame integration of the 2D SAXS patterns of the aligned N_C phase at 15.0°C, and N_B phase at 21.1°C, 21.4°C and 21.9°C, and N_D phase 25.0°C, respectively, of sample s0 for the PP position

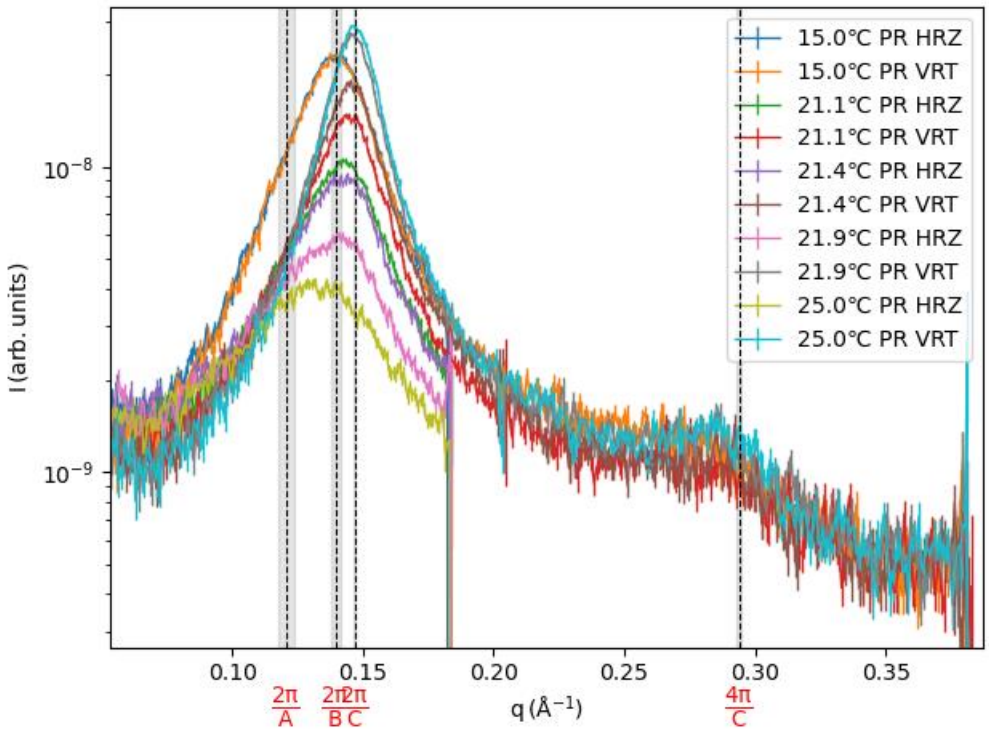

Figure 4.41 Frame integration of the 2D SAXS patterns of the aligned N_C phase at 15.0°C, N_B phase at 21.1°C, 21.4°C and 21.9°C, and N_D phase 25.0°C, respectively, of sample s0 for the PR position.

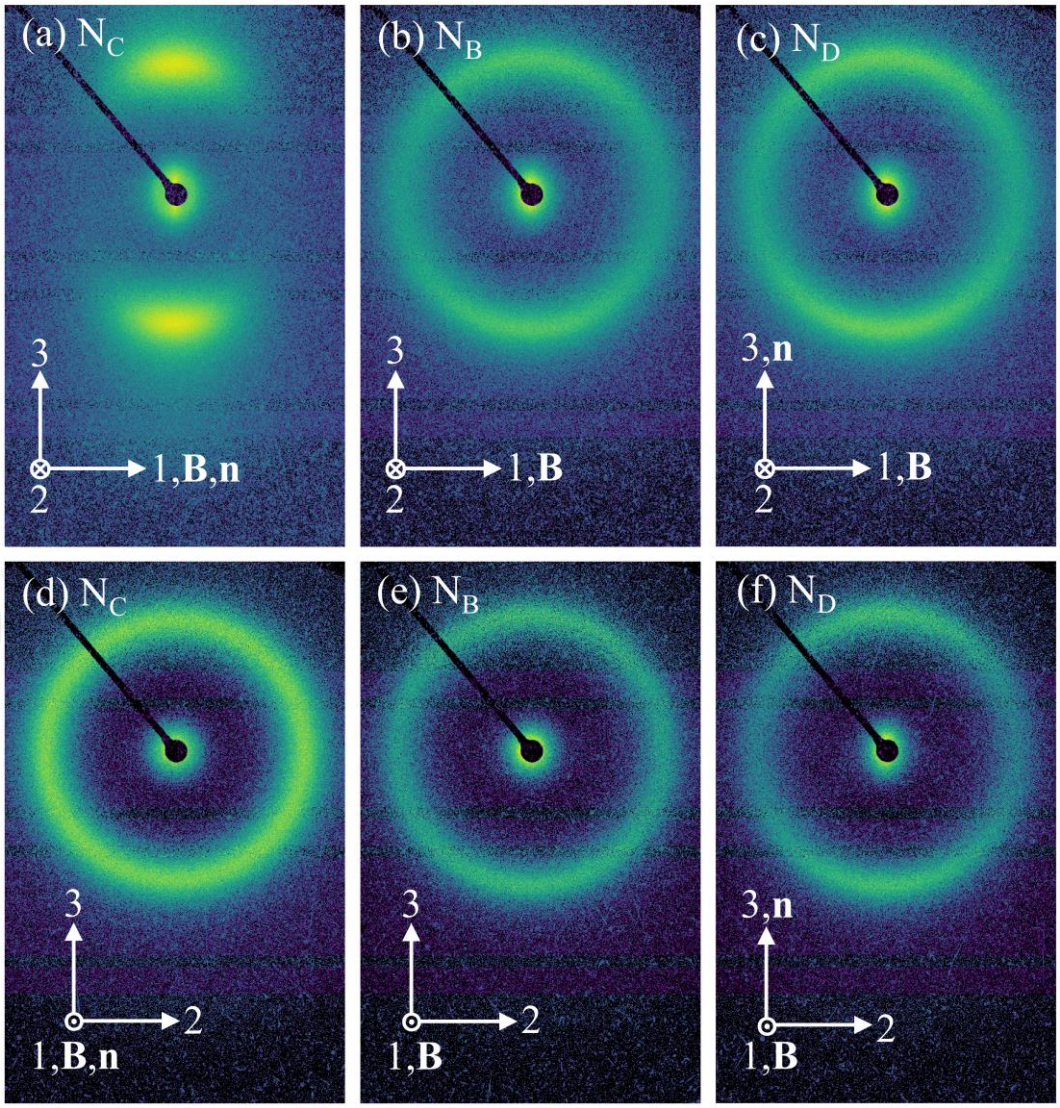

Figure 4.42 The 2D small-angle X-ray scattering (SAXS) patterns of the aligned nematic N_C, N_B and N_D phases for sample s20 (n_{avg}: 4.16). The patterns were measured at 15.0 °C, 24.4 °C, and 25.0 °C, respectively, at the PP position. The patterns (d), (e) and (f) were obtained at the same temperatures at the PR position.

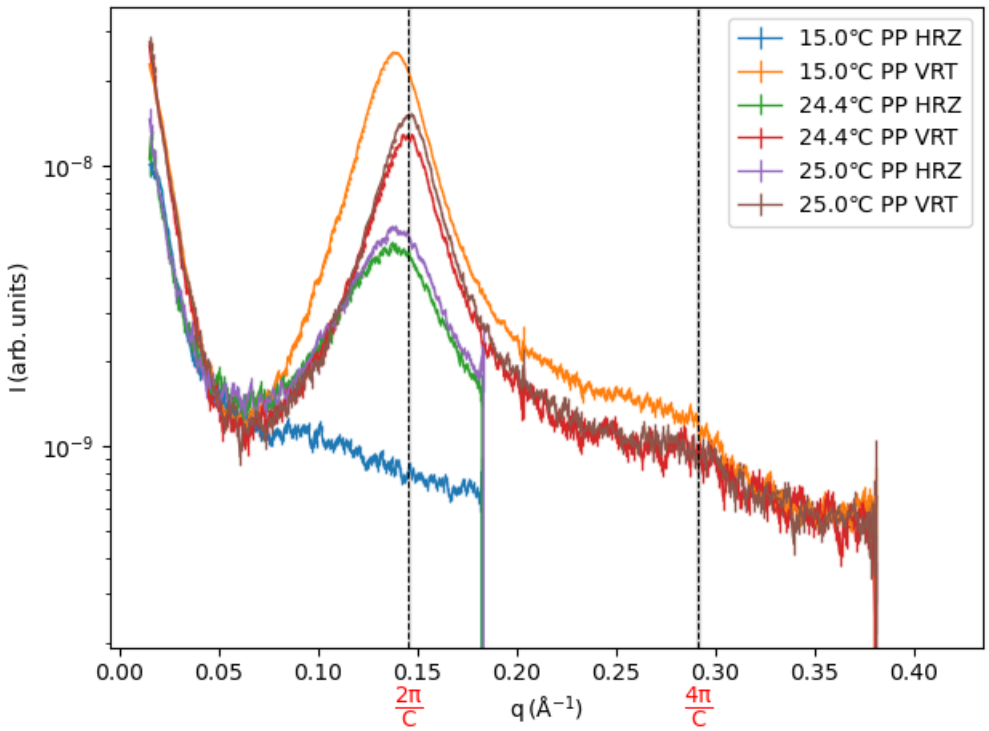

Figure 4.43 Frame integration of the 2D SAXS patterns of the aligned N_C phase at 15.0°C, N_B phase at 24.4°C, and N_D phase 25.0°C, respectively, of sample s20 for the PP position.

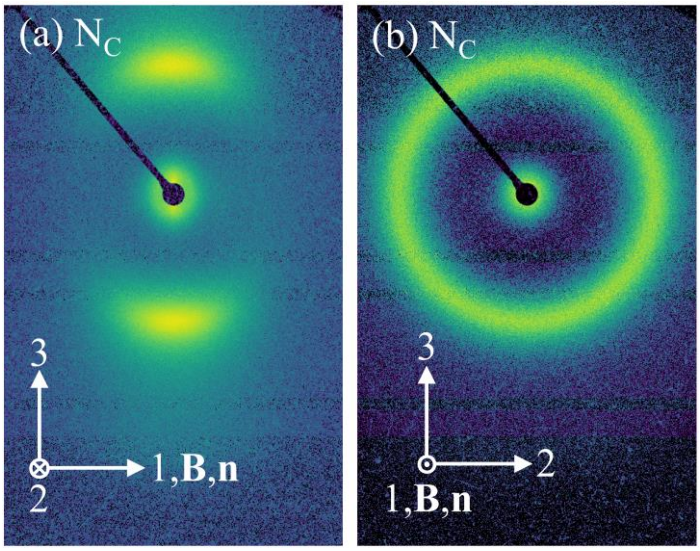

Figure 4.44 The 2D small-angle X-ray scattering (SAXS) patterns of the aligned nematic N_C phase at 15.0 °C for sample s22 (n_{avg}: 4.24) at (a) the PP position and (b) the PR position.

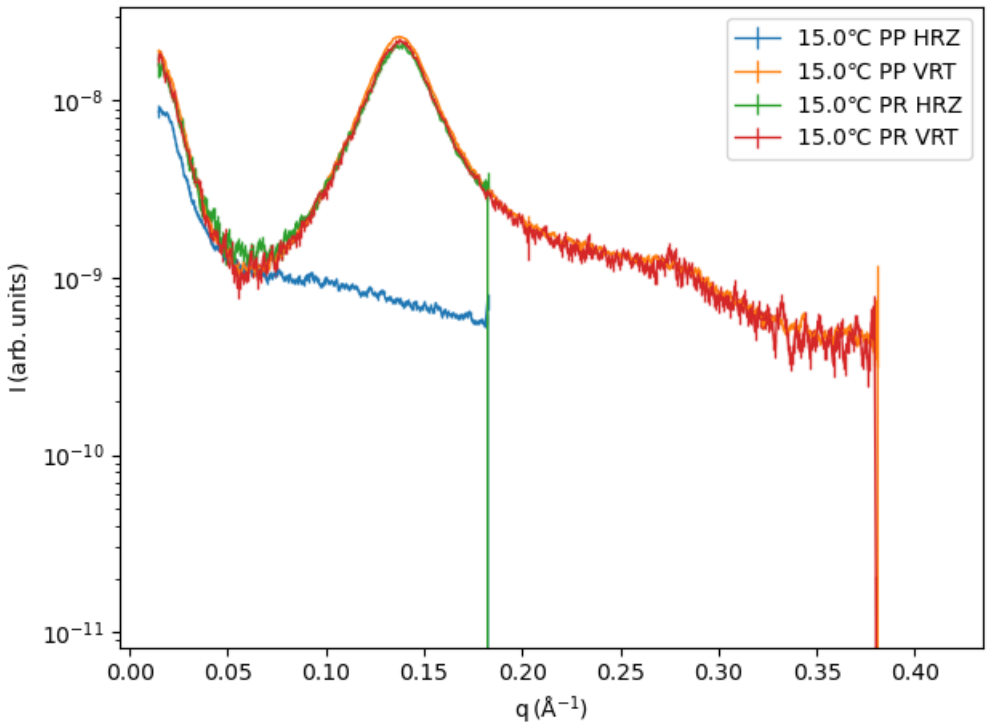

Figure 4.45 Frame integration of the 2D SAXS patterns of the aligned N_C phase of sample s22 at 15.0°C for the PP and PR positions.

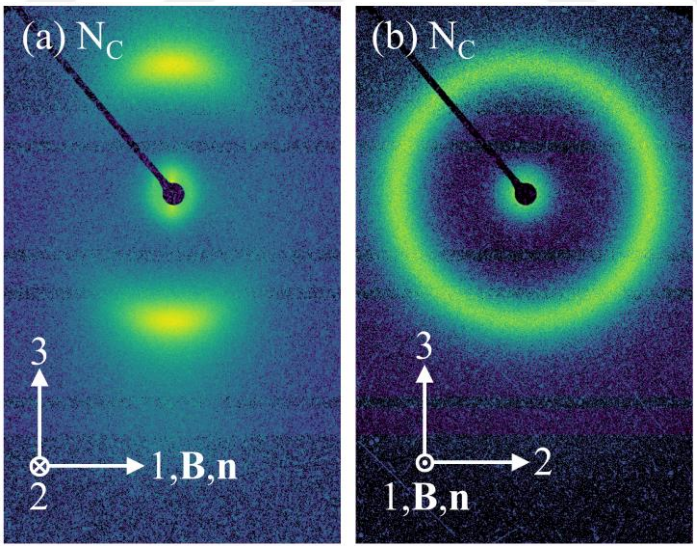

Figure 4.46 The 2D small-angle X-ray scattering (SAXS) patterns of the aligned nematic N_C phase at 15.0 °C for sample s24 (n_{avg}: 4.40) at (a) the PP position and (b) the PR position.

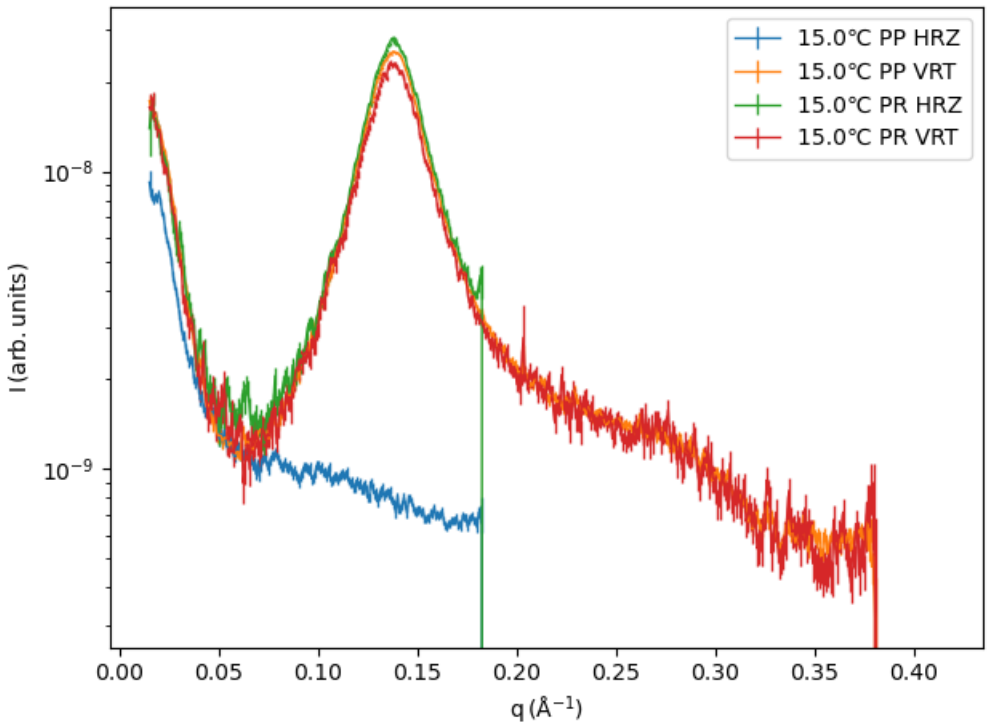

Figure 4.47 Frame integration of the 2D SAXS patterns of the aligned N_C phase of sample s24 at 15.0°C for the PP and PR positions.

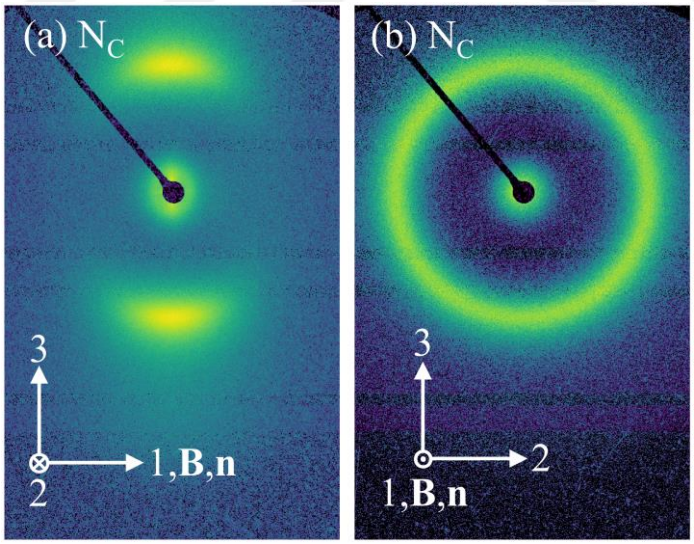

Figure 4.48 The 2D small-angle X-ray scattering (SAXS) patterns of the aligned nematic N_C phase at 15.0 °C for sample s36 (n_{avg}: 4.68) at (a) the PP position and (b) the PR position.

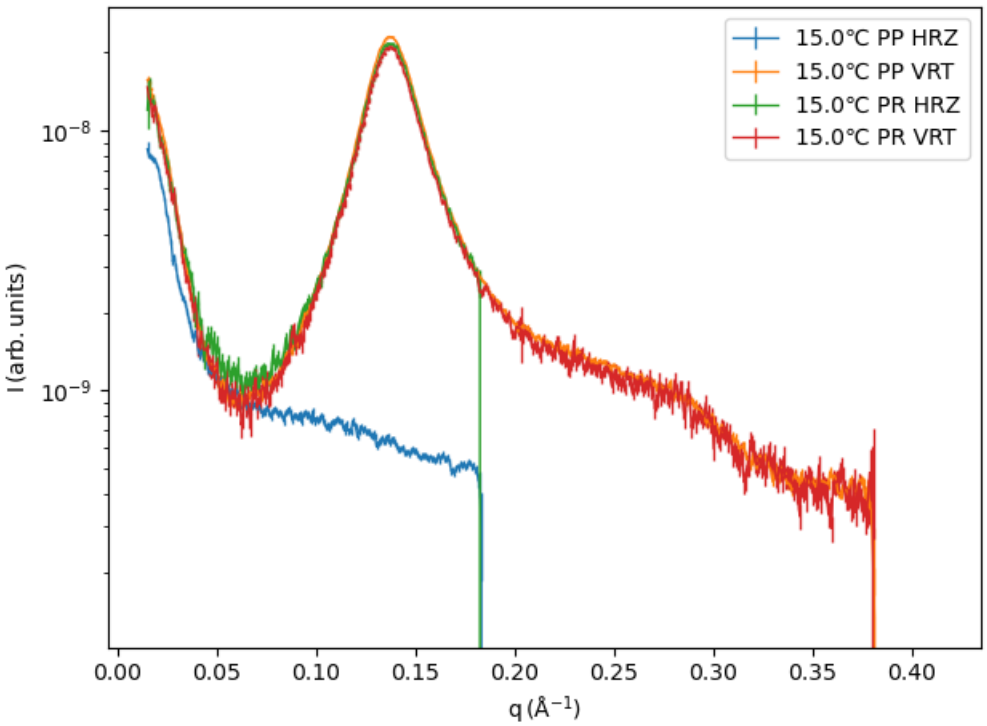

Figure 4.49 Frame integration of the 2D SAXS patterns of the aligned N_C phase of sample s36 at 15.0°C for the PP and PR positions.

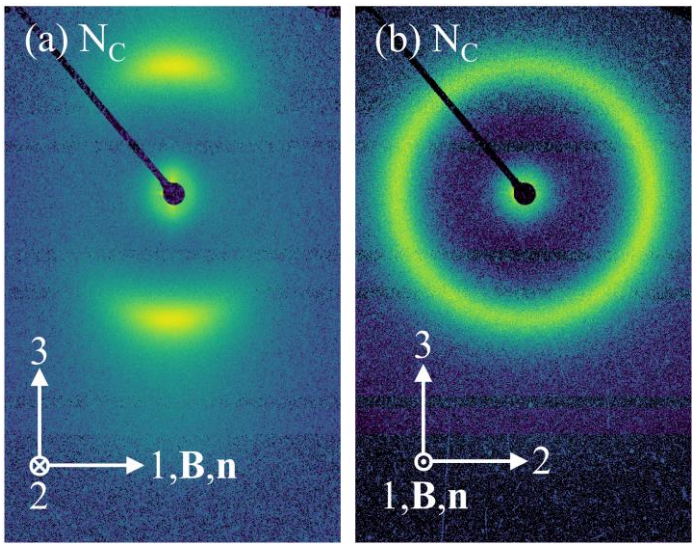

Figure 4.50 The 2D small-angle X-ray scattering (SAXS) patterns of the aligned nematic N_C phase at 15.0 °C for sample s37 (n_{avg}: 4.70) at (a) the PP position and (b) the PR position.

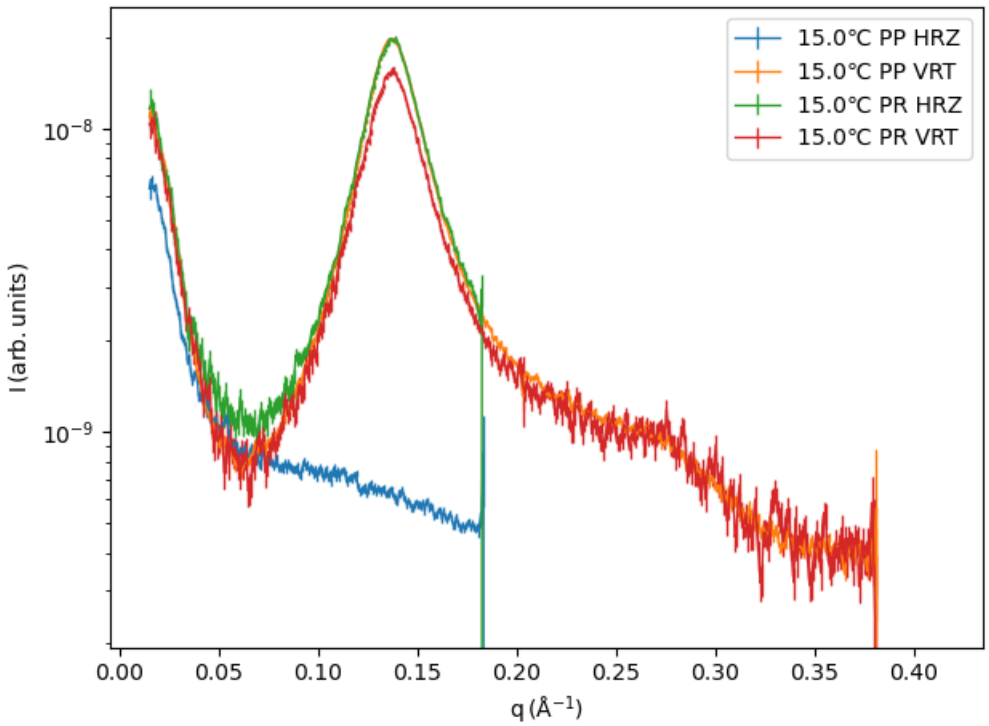

Figure 4.51 Frame integration of the 2D SAXS patterns of the aligned N_C phase of sample s37 at 15.0°C for the PP and PR positions

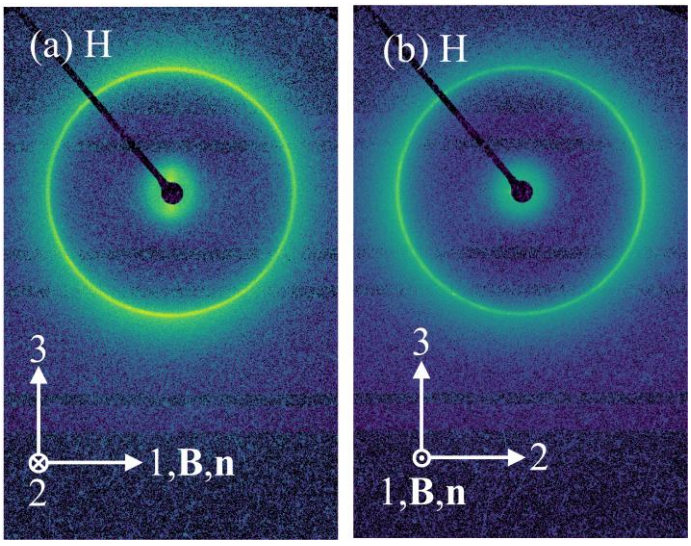

Figure 4.52 The 2D small-angle X-ray scattering (SAXS) patterns of the H phase at 15.0 °C for sample s26 (n_{avg}: 4.80) at (a) the PP position and (b) the PR position.

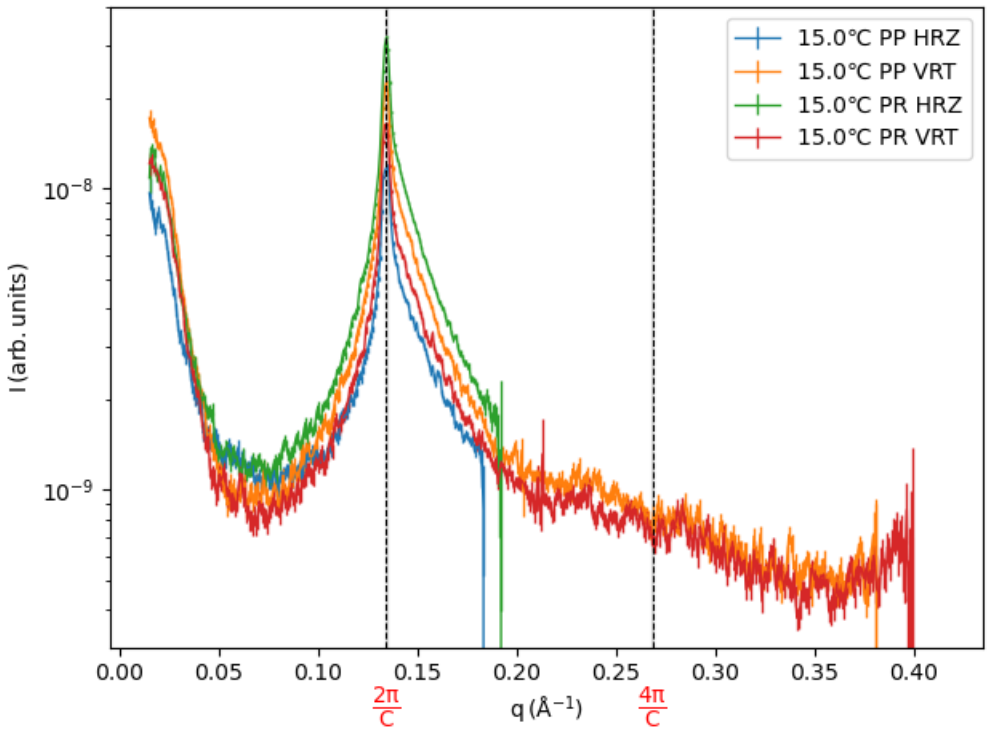

Figure 4.53 Frame integration of the 2D SAXS patterns of the aligned H phase phase of sample s26 at 15.0°C for the PP and PR positions.

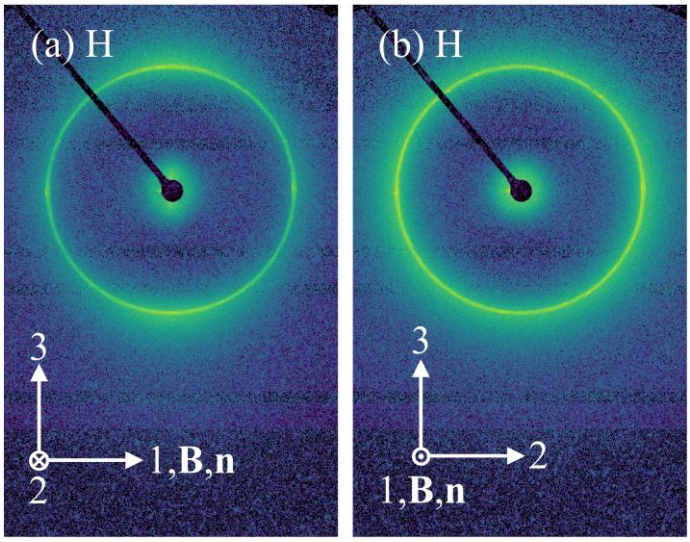

Figure 4.54 The 2D small-angle X-ray scattering (SAXS) patterns of the H phase for sample at 15.0 °C s38 (n_{avg}: 4.90) at (a) the PP position and (b) the PR position.

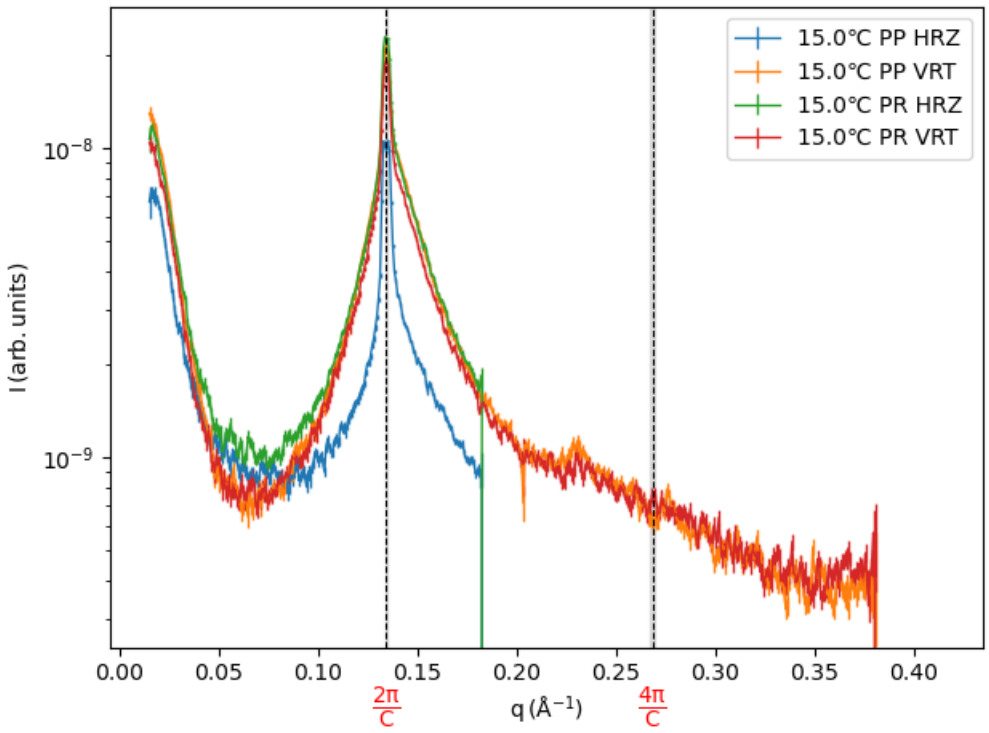

Figure 4.55 Frame integration of the 2D SAXS patterns of the aligned H phase phase of sample s38 at 15.0°C for the PP and PR positions.

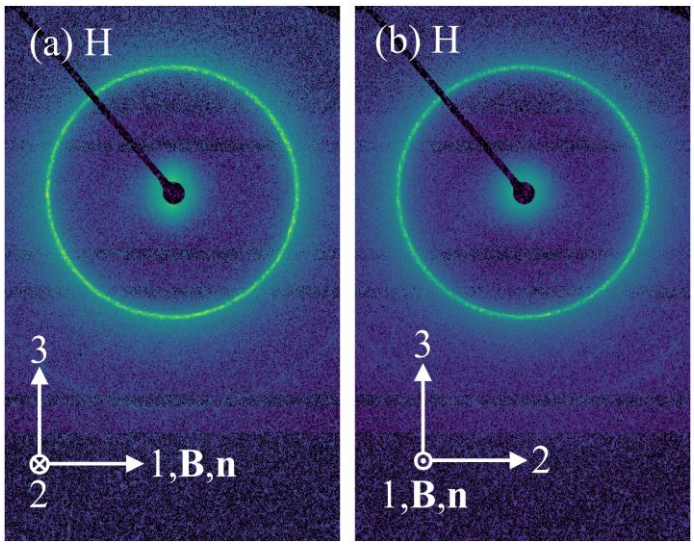

Figure 4.56 The 2D small-angle X-ray scattering (SAXS) patterns of the H phase at 15.0 °C for sample s29 (n_{avg}: 5.40) at (a) the PP position and (b) the PR position.

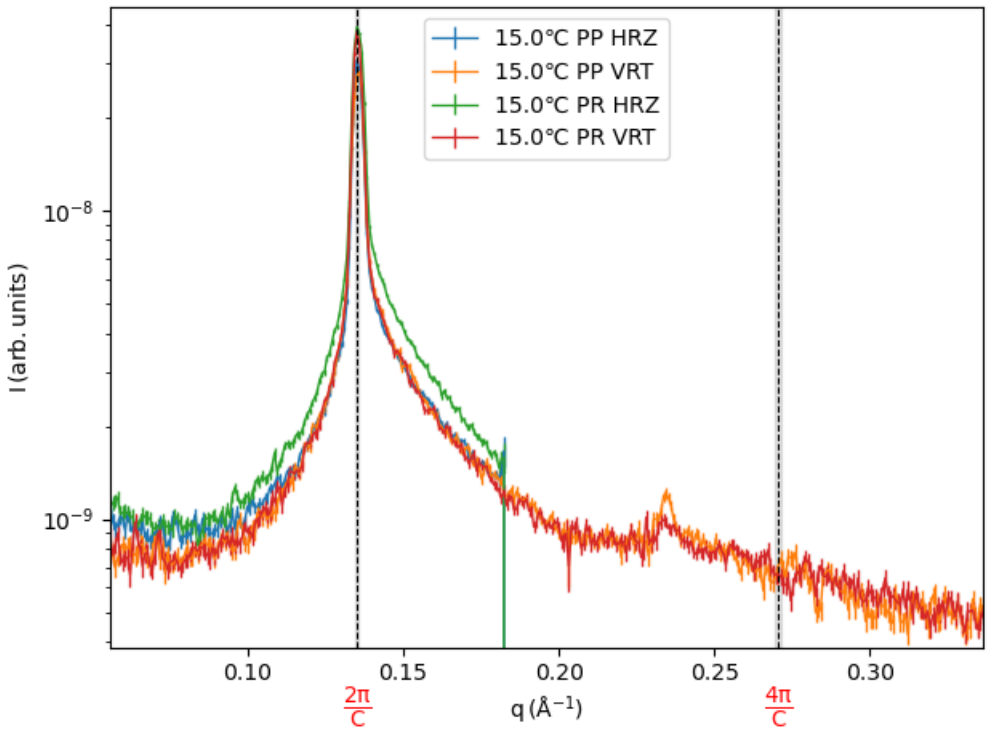

Figure 4.57 Frame integration of the 2D SAXS patterns of the aligned H phase phase of sample s29 at 15.0°C for the PP and PR positions.

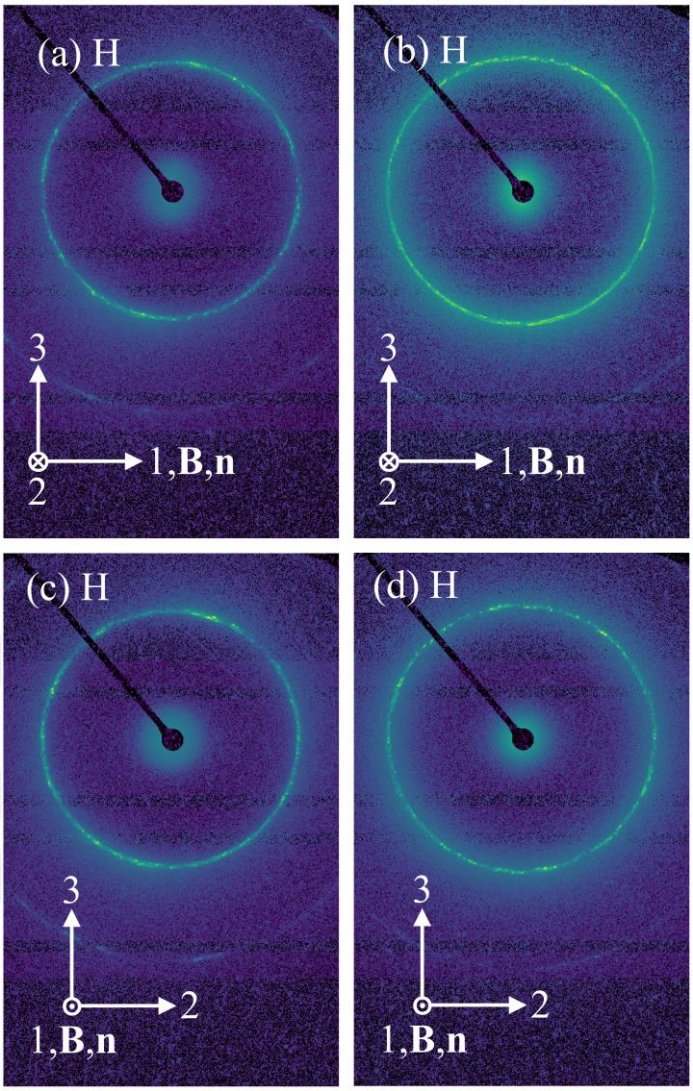

Figure 4.58 The 2D small-angle X-ray scattering (SAXS) patterns of the H phase at 15.0 °C (a and c) and 30 °C (b and d) for sample s32 (n_{avg}: 6.00), The patterns (a) and (b) were measured at the PP position. The patterns (c) and (d) were obtained at the same temperatures at the PR position.

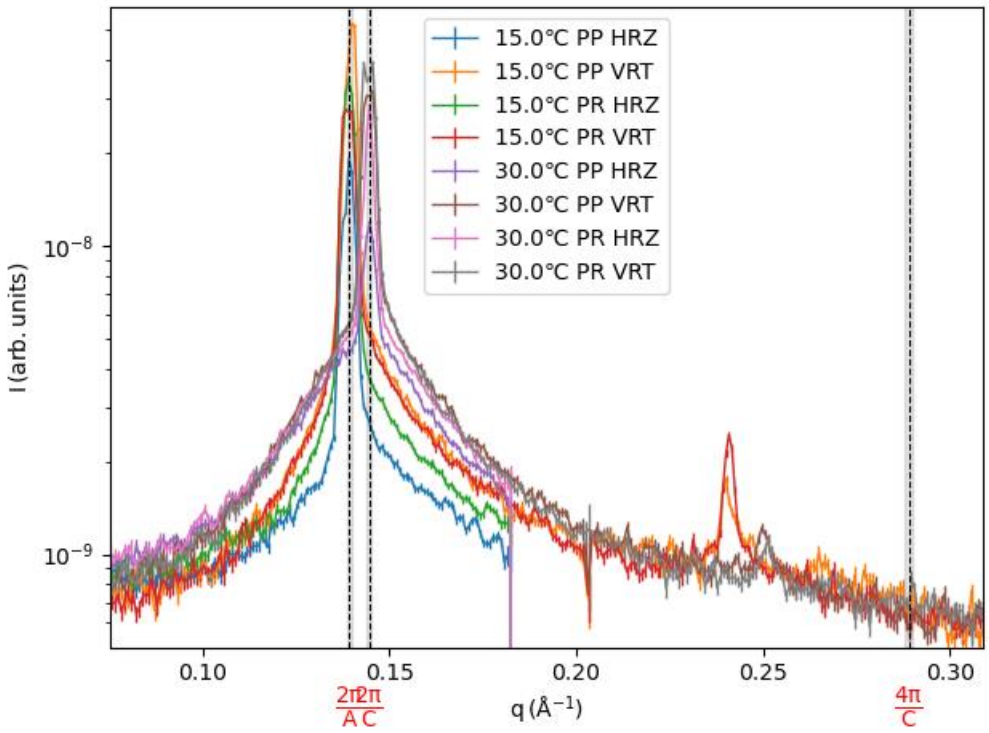

Figure 4.59 Frame integration of the 2D SAXS patterns of the aligned H phase phase of sample at 15.0°C and 30 °C s32 for the PP and PR positions.

The SAXS patterns and their frame integrations are in good agreement with the laser conoscopy and polarized optical microscopy results, except that while sample s9 (n_{avg}: 3.40) exhibited lamellar phase properties according to the SAXS results (Figure 4.23), other techniques gave the properties of the N_D phase. The SAXS (others) measurements were performed in Brazil (in our research laboratories/Türkiye) and it is well-known from the literature that lyotropic samples are very sensitive experimental conditions, especially impurities of components and water quality. So, the difference for the sample s9 may be attributed to the different experimental conditions in those measurements. However, the sample s35 (n_{avg}: 3.50) showed similar properties in all three measurement techniques. Thus, the average of these two n_{avg} values (3.45) may be taken as the n_{avg} value for the lamellar – N_D phase transition.

From the SAXS measurements, we evaluated some micellar parameters: micelle's core average micelle dimensions (A, B, C), micelle shape anisotropy (SA) and the average area per surfactant head group at micelle surfaces (a_0). The SA values is calculated according to the following equation;

$$SA = \left\{ \frac{[(A+B)/2] - C}{[(A+B)/2]} \right\} \quad (4.7)$$

The SA is a measure of the average thickness of the micelle bilayer C relative to the average of the other two dimensions A and B of the micelle's core. The bilayer thickness is related to the lengths of the surfactant's alkyl chain and it varies very small variations with temperature and composition of the mixture. Therefore, it can be said that the SA gives information about the relative growth of the micelle in the directions perpendicular to the amphiphiles' bilayer direction. Because lamellar and hexagonal phases consist of infinitely wide and long micelles, respectively, it is not possible to calculate A and B micelle dimensions. So, only the micelle dimension C can be calculated for these phases. The micellar parameters for some samples are given in Tables 4.6-4.8.

Table 4.6 Micelle average dimension, C, and average area per surfactant head group at micelle surfaces of the samples which give lamellar phases.

Sample (n_{avg})	**T/°C**	**Phase type**	**C/Å**	**a_0/Å²**
s16 (2.00)	15.0	L_α	18.5±0.8	34.9±2.3
	25.0	L_α	18.4±0.8	35.1±2.3
	30.0	L_α	18.3±0.8	35.3±2.4
s12 (2.80)	15.0	L_α	16.4±0.7	39.2±2.6
	25.0	L_α	16.4±0.7	39.3±2.6
	30.0	L_α	16.4±0.7	39.4±2.6
s34 (3.36)	25.0	L_α	15.7±0.7	41.1±2.8
	30.0	L_α	15.7±0.7	41.2±2.8
s9 (3.40)	15.0	L_α	15.7±0.7	41.2±2.8
	25.0	L_α	15.6±0.7	41.2±2.8
	30.0	L_α	15.5±0.7	41.6±2.8
s35 (3.50)	25.0	L_α	15.5±0.7	41.5±2.8
	30.0	L_α	15.5±0.7	41.7±2.8

Table 4.7 Micelle average dimensions (A, B, C), shape anisotropies and average area per surfactant head group at micelle surfaces of the samples which give nematic phases.

Sample (n_{avg})	**T/°C**	**Phase type**	**Micelle's core average dimensions**			**SA**	**a_0/Å^2**
			A/Å	B/Å	C/Å		
s8 (3.60)	15.0	N_D	54.3±2.5	45.1±2.1	27.8±1.6	0.44±0.04	49±3
	25.0	N_D	51.5±2.6	40.5±2.0	28.0±1.6	0.39±0.04	51±4
s17 (3.72)	15.0	N_D	53.8±4.0	41.7±2.9	27.8±2.4	0.42±0.06	50±5
	25.0	N_D	50.4±3.0	38.9±2.3	27.9±2.0	0.37±0.05	52±5
s5 (3.80)	15.0	N_D	55.2±3.0	40.3±1.8	28.0±1.7	0.41±0.04	50±4
	25.0	N_D	46.5±2.4	35.1±1.7	28.8±1.5	0.29±0.04	54±4
s4 (3.84)	15.0	N_B,N_D	53.9±3.0	41.2±2.2	27.8±1.9	0.42±0.05	50±4
	25.0	N_B,N_D	47.2±4.0	36.4±2.6	28.5±2.2	0.32±0.06	53±5
s0 (4.00)	25.0	N_C,N_B,N_D	43.3±2.6	32.7±1.9	29.4±1.6	0.23±0.05	56±4
s20 (4.16)	25.0	N_C,N_B,N_D	50.9±6.0	31.5±4.0	29.0±3.0	0.30±0.10	54±8

Table 4.8 Micelle average dimension, C, and average area per surfactant head group at micelle surfaces of the samples which give hexagonal phases.

Sample (n_{avg})	**T/°C**	**Phase type**	**C/Å**	**a_0/Å^2**
s26 (4.80)	15.0	H	29.3±0.7	44.0±2.4
s38 (4.90)	15.0	H	29.2±0.7	44.1±2.4
s29 (5.40)	15.0	H	28.9±0.7	44.7±2.5
s32 (6.00)	15.0	H	28.0±0.6	46.1±2.5
	30.0	H	26.9±0.6	47.9±2.6

From Tables 4.4-4.6, the average thickness of the micelle bilayer C for the nematic and hexagonal phases is significantly larger than that for the lamellar phases. While the bilayer thickness in the nematic phases increases with the increase in the n_{avg} values, it decreases in both lamellar and hexagonal phases. Furthermore, the a_0 values increase with the n_{avg} values in three different lyotropic structures. If we compare three types of lyotropic samples together,

$$a_0 \text{ (nematic)} > a_0 \text{ (hexagonal)} > a_0 \text{ (lamellar)}$$

This is an unexpected result because as the head group size increases with the increase of the amount of DDMEABr in the samples, the a_0 values would increase to give the order a_0 (hexagonal) > a_0 (nematic) > a_0 (lamellar). The results may be interpreted as follows. As the number of $-CH_2$ or $-CH_3$ group (i.e., n_{avg}) in the surfactant head groups may cause the formation of van der Waals attractions (or London forces) between these groups, which leads to the decrease in the repulsions between the head groups, and the average area per head groups gets relatively small. Our results indicate that these attractions are more dominant in the samples which give hexagonal phases with respect to the nematic and lamellar ones.

5. CONCLUSION AND RECOMMENDATION

This thesis aims to investigate the effect of the interactions between SSY and surfactant head groups on the formation of the nematic, lamellar and hexagonal phases in binary surfactant systems of dodecyldimethylethylammonium bromide (DDMEABr)/dodecyldimethylammonium bromide (DDMABr) and DDMEABr/dodecyltriethylammonium bromide (DTEABr). The properties of lyotropic samples were studied via polarized optical microscopy, laser conoscopy, and Small-angle X-ray Scattering. The results are in good agreement with each other and also with the literature. According to the experimental studies, the following conlusions can be made:

(a) The degree of surfactant-dye interactions on micellar surfaces is directly related to the degree of chaotropic property of the ionic species of both

molecules. When a lamellar phase is obtained in cases where there are strong surfactant-dye interactions and the chaotropic degree of the Sunset Yellow molecule is closer to the chaotropic degree of the head group of the DDMABr molecule than that of DTEABr.

(b) Considering the IBM model of lyotropic nematic phases, surfactant-dye interactions play an active role in the orientational fluctuations of the phase director required to obtain different types of nematic phases.

(c) Surfactant-dye molecule interactions are related to the area per head group of the surfactants on the micellar surfaces.

(d) Although the average number of $-CH_2$ or $-CH_3$ group (n_{avg}) in the surfactant head groups is a parameter to obtain different lyotropic structures, the interactions between these groups at micelle surfaces are also important in addition to the n_{avg} values.

In summary, it has been revealed within the scope of this thesis that the surfactant-dye interactions and the head group size are important parameters in controlling the properties of surfactant-based lyotropic liquid crystals, especially the formation of nematic, hexagonal, and lamellar phases.

6. REFERENCES

1. Sarney DB, Vulfson EN. Application of enzymes to the synthesis of surfactants. Trends Biotechnol. 1995;13(5):164–72.

2. Mukherjee S, Das P, Sen R. Towards commercial production of microbial surfactants. Trends Biotechnol. 2006;24(11):509–15.

3. Vater J. Lipopetides, an attractive class of microbial surfactants. Polym as Colloid Syst. 2007;18:12–8.

4. Nazar MF, Shah SS, Khosa MA. Interaction of azo dye with cationic surfactant under different pH conditions. J Surfactants Deterg. 2010;13(4):529–37.

5. Schultz J, Rosado AS. Extreme environments: a source of biosurfactants for biotechnological applications. Extremophiles [Internet]. 2020;24(2):189–206. Available from: https://doi.org/10.1007/s00792-019-01151-2

6. Alejandro DJCS. Surfactants of microbial origin and its application in foods. Sci Res Essays. 2020;15(1):11–7.

7. Schramm LL, Stasiuk EN, Marangoni DG. Surfactants and their applications. Annu Reports Prog Chem - Sect C. 2003;99(2):3–48.

8. Kralova I, Sjöblom J. Surfactants used in food industry: A review. J Dispers Sci Technol. 2009;30(9):1363–83.

9. Silva R de CFS, Almeida DG, Rufino RD, Luna JM, Santos VA, Sarubbo LA. Applications of biosurfactants in the petroleum industry and the remediation of oil spills. Int J Mol Sci. 2014;15(7):12523–42.

10. Gracida J, Ortega-Ortega J, Torres B LG, Romero-Avila M, Abreu A. Synthesis of Anionic Surfactant and Their Application in Washing of Oil-Contaminated Soil. J Surfactants Deterg. 2017;20(2):493–502.

11. Akshai A, Raouf AA, Chaudhuri RG. Importance of interfacial and rheological properties in the suppression of uniform deposition to coffee ring pattern of zinc oxide nanofluids in the presence of anionic surfactants. Colloid Polym Sci. 2020;298(6):587–94.

12. Rahate AR, Nagarkar JM. Emulsification of vegetable oils using a blend of nonionic surfactants for cosmetic applications. J Dispers Sci Technol. 2007;28(7):1077–80.

13. Neta NS, Teixeira JA, Rodrigues LR. Sugar Ester Surfactants: Enzymatic Synthesis and Applications in Food Industry. Crit Rev Food Sci Nutr. 2015;55(5):595–610.

14. Nagose S, Rose E, Joshi A. Study on wetting and dispersion of the Pigment Yellow 110. Prog Org Coatings. 2019 Aug 1;133:55–60.

15. Bento RMF, Almeida MR, Bharmoria P, Freire MG, Tavares APM. Improvements in the enzymatic degradation of textile dyes using ionic-liquid-based surfactants. Sep Purif Technol. 2020 Mar 18;235:116191.

16. Kwon TK, Kim JC. Monoolein cubic phase containing acidic proteinoid: PH-dependent release. Drug Dev Ind Pharm. 2011;37(1):56–61.

17. Fong W khay, Hanley TL, Thierry B, Kirby N, Waddington LJ, Boyd BJ. Controlling the Nanostructure of Gold Nanorod − Lyotropic Liquid- Crystalline Hybrid Materials Using Near-Infrared Laser Irradiation. 2012;

18. Vallooran JJ, Negrini R, Mezzenga R. Controlling anisotropic drug diffusion in lipid-Fe3O4 nanoparticle hybrid mesophases by magnetic alignment. Langmuir. 2013;29(4):999–1004.

19. Collings PJ. Liquid Crystals : Nature ' s Delicate Phase Of Matter. 2002;

20. Akpinar E, Guner E, Demir-Ordu O, Neto AMF. Effect of head-group size of some tetradecylalkylammonium bromide surfactants on obtaining the lyotropic biaxial nematic phase. Eur Phys J E. 2019;42(4).

21. Lawson KD, Flautt TJ. Magnetically Oriented Lyotropic Liquid Crystalline Phases. J Am Chem Soc. 1967;89(21):5489–91.

22. Boden N, Corne SA, Jolley KW. Lyotropic mesomorphism of the cesium pentadecafluorooctanoate/water system: High-resolution phase diagram. J Phys Chem. 1987;91(15):4092–105.

23. Oliveira EA, Liebert L, Figueiredo Neto AM. A new soap/detergent/water lyotropic liquid crystal with a biaxial nematic phase. Liq Cryst. 1989;5(6):1669–75.

24. Ho CC, Goetz RJ, El-Aasser MS. A Biaxial Lyotropic Nematic Phase in Dilute Solutions of Sodium Lauryl Sulfate-1-Hexadecanol-Water. Langmuir. 1991;7(4):630–5.

25. Nicoletta FP, Chidichimo G, Golemme A, Picci N. Phases and phase transitions in a nematic lyotropic system with a biaxial phase. Liq Cryst. 1991;10(5):665–74.

26. De Melo Filho AA, Laverde A, Fujiwara FY. Observation of two biaxial nematic mesophases in the tetradecyltrimethylammonium bromide/decanol/water system. Langmuir. 2003;19(4):1127–32.

27. Akpinar E, Reis D, Figueiredo Neto AM. Lyotropic mixture made of potassium laurate/1-undecanol/K2SO4/water presenting high birefringences and large biaxial nematic phase domain: A laser conoscopy study. Eur Phys J E. 2012;35(6).

28. Wolff T, Klaussner B. Overlap of colloid chemistry and photochemistry in surfactant systems. Adv Colloid Interface Sci. 1995 Aug 31;59(C):31–94.

29. Akpinar E, Turkmen M, Canioz C, Martins Figueiredo Neto A. Role of kosmotrope-chaotrope interactions at micelle surfaces on the stabilization of lyotropic nematic phases. Eur Phys J E. 2016;39(11).

30. Yu LJ, Saupe A. Observation of a biaxial nematic phase in potassium laurate-1-decanol-water mixtures. Phys Rev Lett. 1980;45(12):1000–3.

31. Galerne Y, Liébert L. Zigzag disclinations in biaxial nematic liquid crystals. Phys Rev Lett. 1985;55(22):2449–51.

32. Madsen LA, Dingemans TJ, Nakata M, Samulski ET. Thermotropic biaxial nematic liquid crystals. Phys Rev Lett. 2004;92(14):1–4.

33. Tschierske C, Photinos DJ. Biaxial nematic phases. J Mater Chem. 2010;20(21):4263–94.

34. Nasrin L, Kabir E, Rahman M. External magnetic field-dependent tricritical points of uniaxial-to-biaxial nematic transition. Phase Transitions. 2016;89(2):193–201.

35. Akpinar E, Neto AMF. Experimental conditions for the stabilization of the lyotropic biaxial nematic mesophase. Crystals. 2019;9(3).

36. Kim YK, Cukrov G, Vita F, Scharrer E, Samulski ET, Francescangeli O, et al. Search for microscopic and macroscopic biaxiality in the cybotactic nematic phase of new oxadiazole bent-core mesogens. Phys Rev E. 2016;93(6):1–8.

37. Bartolino R, Chiaranza T, Meuti M, Compagnoni R. Uniaxial and biaxial lyotropic nematic liquid crystals. Phys Rev A. 1982;26(2):1116–9.

38. Alben R. Liquid crystal phase transitions in mixtures of rodlike and platelike molecules. J Chem Phys. 1973;59(8):4299–304.

39. Blanco-Fernández G, Blanco-Fernandez B, Fernández-Ferreiro A, Otero-Espinar FJ. Lipidic lyotropic liquid crystals: Insights on biomedical applications. Adv Colloid Interface Sci. 2023 Mar 1;313:102867.

40. Bisoyi HK, Kumar S. Discotic nematic liquid crystals: Science and technology. Chem Soc Rev. 2010;39(1):264–85.

41. Guo X, Wang L, Wei X, Zhou S. Polymer-based drug delivery systems for cancer treatment. J Polym Sci Part A Polym Chem. 2016;54(22):3525–50.

42. Dierking I, Al-Zangana S. Lyotropic liquid crystal phases from anisotropic nanomaterials. Nanomaterials. 2017;7(10).

43. Yanase N, Noguchi H, Asakura H, Suzuta T. Preparation of magnetic latex particles by emulsion polymerization of styrene in the presence of a ferrofluid. J Appl Polym Sci. 1993;50(5):765–76.

44. Landfester K, Ramírez LP. Encapsulated magnetite particles for biomedical application. J Phys Condens Matter. 2003;15(15).

45. Chambon C, Clement O, Le Blanche A, Schouman-Claeys E, Frija G. Superparamagnetic iron oxides as positive MR contrast agents: In vitro and in vivo evidence. Magn Reson Imaging. 1993;11(4):509–19.

46. Roger J, Pons JN, Massart R, Halbreich A, Bacri JC. Some biomedical applications of ferrofluids. EPJ Appl Phys. 1999;5(3):321–5.

47. Dodd CH, Hsu HC, Chu WJ, Yang P, Zhang HG, Mountz JD, et al. Normal T-cell response and in vivo magnetic resonance imaging of T cells loaded with HIV transactivator-peptide-derived superparamagnetic nanoparticles. J Immunol Methods. 2001 Oct 1;256(1–2):89–105.

48. Billotey C, Wilhelm C, Devaud M, Bacri JC, Bittoun J, Gazeau F. Cell internalization of anionic maghemite nanoparticles: Quantitative effect on magnetic resonance imaging. Magn Reson Med. 2003;49(4):646–54.

49. Tans SJ, Verschueren ARM, Dekker C. Room-temperature transistor based on a single carbon nanotube. Nature. 1998;393(6680):49–52.

50. Baughman RH, Zakhidov AA, De Heer WA. Carbon nanotubes - The route toward applications. Science (80-). 2002;297(5582):787–92.

51. Thostenson ET, Ren Z, Chou TW. Advances in the science and technology of carbon nanotubes and their composites: a review. Compos Sci Technol. 2001 Oct 1;61(13):1899–912.

52. Wong SS, Joselevich E, Woolley AT, Cheung CL, Lieber CM. Covalently functionalized nanotubes as nanometresized probes in chemistry and biology. Nature. 1998;394(6688):52–5.

53. Jing Kong, Nathan R. Franklin, Chongwu Zhou, Michael G. Chapline, Shu Peng, Kyeongjae Cho, et al. Nanotube Molecular Wires as Chemical Sensors. Science (80-) [Internet]. 2000;287(January):622–5. Available from: www.sciencemag.org

54. Baughman RH, Cui C, Zakhidov AA, Iqbal Z, Barisci JN, Spinks GM, et al. Carbon nanotube actuators. Science (80-). 1999;284(5418):1340–4.

55. Dierking I, Scalia G, Morales P, LeClere D. Aligning and reorienting carbon nanotubes with nematic liquid crystals. Adv Mater. 2004;16(11):865–9.

56. Lagerwall J, Scalia G, Haluska M, Dettlaff-Weglikowska U, Roth S, Giesselmann F. Nanotube alignment using lyotropic liquid crystals. Adv Mater. 2007;19(3):359–64.

57. Buwalda RT, Engberts JBFN. Aggregation of dicationic surfactants with methyl orange in aqueous solution. Langmuir. 2001;17(4):1054–9.

58. Gokturk S, Tuncay M. Dye-Surfactant Interaction in the Premicellar Region. J Surfactants Deterg. 2003;6(4):325–30.

59. Khan MN, Sarwar A. Study of dye–surfactant interaction: Aggregation and dissolution of yellowish in N-dodecyl pyridinum chloride. Fluid Phase Equilib. 2006 Jan 31;239(2):166–71.

60. Rashidi-Alavijeh M, Javadian S, Gharibi H, Moradi M, Tehrani-Bagha AR, Shahir AA. Intermolecular interactions between a dye and cationic surfactants: Effects of alkyl chain, head group, and counterion. Colloids Surfaces A Physicochem Eng Asp. 2011 May 5;380(1–3):119–27.

61. Fazeli S, Sohrabi B, Tehrani-Bagha AR. The study of Sunset Yellow anionic dye interaction with gemini and conventional cationic surfactants in aqueous solution. Dye Pigment. 2012 Dec 1;95(3):768–75.

62. Erdinc N, Göktürk S. Spectrophotometric and Conductometric Studies on the Interaction of Anionic Dye Eosin-Y with Cationic Micelles. Anal Chem Lett. 2014;4(3):146–57.

63. Akpinar E, Topcu G, Reis D, Neto AMF. Effect of the anionic azo dye Sunset Yellow in lyotropic mixtures with uniaxial and biaxial nematic phases. J Mol Liq. 2020 Nov 15;318:114010.

64. Akpinar E, Uygur N, Ordu OD, Reis D, Neto AMF. Effect of the surfactant head-group size dependence of the dye-surfactant interactions on the lyotropic uniaxial to biaxial nematic phase transitions. J Mol Liq. 2021 Jun 15;332:115842.

65. Mitchell JD, Tiddy GJ., Waring L, Bostock T, Mcdonald MP. Phase Behaviour of Polyoxyethylene Surfactants with Water. J Chem SOC, Faraday Trans I. 1983;79:975–1000.

66. Blackmore ES, Tiddy GJT. Phase behaviour and lyotropic liquid crystals in cationic surfactant-water systems. J Chem Soc Faraday Trans 2 Mol Chem Phys. 1988;84(8):1115–27.

67. Santos OR, Braga WS, Luders DD, Sampaio AR, Kimura NM, Simões M, et al. Optical characterization of a biaxial nematic between uniaxial nematic lyotropic phases. Phase Transitions [Internet]. 2021;94(6–8):546–55. Available from: https://doi.org/10.1080/01411594.2021.1945598

68. http://gemologyproject.com/wiki/index.php?title=Polariscope.

69. Wang P. Visualizing the conoscopic isochromatic interference fringes in anisotropic crystals by spinning polarizer and analyzer. Opt Lett. 2012;37(21):4392.

70. Samlan CT, Viswanathan NK. Field-controllable Spin-Hall Effect of Light in Optical Crystals: A Conoscopic Mueller Matrix Analysis. Sci Rep. 2018 Dec 1;8(1).

71. Horowitz VR, Janowitz LA, Modic AL, Heiney PA, Collings PJ. Aggregation behavior and chromonic liquid crystal properties of an anionic monoazo dye. Phys Rev E - Stat Nonlinear, Soft Matter Phys. 2005;72(4).

72. Edwards DJ, Jones JW, Lozman O, Ormerod AP, Sintyureva M, Tiddy GJT. Chromonic liquid crystal formation by edicol sunset yellow. J Phys Chem B. 2008;112(46):14628–36.

73. Smaisim GF, mohammed DB, Abdulhadi AM, Uktamov KF, Alsultany FH, Izzat SE, et al. Nanofluids: properties and applications. J Sol-Gel Sci Technol. 2022;104(1):1–35.

74. Akpinar E, Reis D, Figueiredo Neto AM. Anomalous behavior in the crossover between the negative and positive biaxial nematic mesophases in a lyotropic liquid crystal. ChemPhysChem. 2014;15(7):1463–9.

75. Akpinar E, Reis D, Neto AMF. Effect of alkyl chain length of alcohols on nematic uniaxial-to-biaxial phase transitions in a potassium laurate/alcohol/K 2SO 4/water lyotropic mixture. Liq Cryst. 2012;39(7):881–8.

76. Akpinar E, Canioz C, Turkmen M, Reis D, Figueiredo Neto AM. Effect of the surfactant alkyl chain length on the stabilisation of lyotropic nematic phases. Liq Cryst [Internet]. 2018;45(2):219–29. Available from: http://dx.doi.org/10.1080/02678292.2017.1309698

77. Sharma K, Chauhan S. Effect of biologically active amino acids on the surface activity and micellar properties of industrially important ionic surfactants. Colloids Surfaces A Physicochem Eng Asp. 2014 Jul 5;453(1):78–85.

78. Chauhan S, Kaur M, Kumar K, Chauhan MS. Study of the effect of electrolyte and temperature on the critical micelle concentration of dodecyltrimethylammonium bromide in aqueous medium. J Chem Thermodyn. 2014 Nov 1;78:175–81.

79. Sein A, Engberts JBFN. Micelle to Lamellar Aggregate Transiiion of an Anionic Surfactant in Dilute Aqueous Solution Induced by Alkali Metal Chloride and Tetraalkylammonium Chloride Salts. Langmuir. 1995;11(2):455–65.

80. Aswal VK, Goyal PS. Counterions in the growth of ionic micelles in aqueous electrolyte solutions: A small-angle neutron scattering study. Phys Rev E - Stat Physics, Plasmas, Fluids, Relat Interdiscip Top. 2000;61(3):2947–53.

81. Dawin UC, Lagerwall JPF, Giesselmann F. Electrolyte effects on the stability of nematic and lamellar lyotropic liquid crystal phases: Colligative and ion-specific aspects. J Phys Chem B. 2009;113(33):11414–20.

82. Oelschlaeger C, Suwita P, Willenbacher N. Effect of counterion binding efficiency on structure and dynamics of wormlike micelles. Langmuir. 2010;26(10):7045–53.

83. Luzzati V, Mustacchi H, Skoulios A, Husson F. La structure des colloïdes d'association. I. Les phases liquide–cristallines des systèmes amphiphile–eau. Acta Crystallogr. 1960;13(8):660–7.